

## ABSTRACT

SANDIN, ANDREAS AXEL TOMAS. Tunneling Spectroscopy Studies of Epitaxial Graphene on SiC(0001) and Its Interfaces. (Under the direction of Dr. J.E. (Jack) Rowe and Dr. Daniel B. Dougherty).

A two dimensional network of  $sp^2$  bonded carbon atoms is defined as graphene. This novel material possesses remarkable electronic properties due to its unique band structure at the vicinity of the Fermi energy. The toughest challenge to bring use of graphene electronic properties in device geometries is that graphene is exceptionally sensitive to its electrical environment for integration into macroscopic system of electrical contacts and substrates.

One of the most promising substrates for graphene is the polar surfaces of SiC for the reason it can be grown epitaxially by sublimating Si from the top-most SiC atomic layers.

In this work, the interfaces of graphene grown on the Si-terminated polar surface SiC(0001) is studied in UHV using scanning tunneling microscopy (STM), scanning tunneling spectroscopy (STS), low energy electron diffraction (LEED) and auger electron

Spectroscopy (AES). STM is used image the graphene surface and interfaces with the capability of atomic resolution. LEED is used to study surface atomic reciprocal ordering and AES is used to determine surface atomic composition during the graphene formation.

Interfacial layer (Buffer layer), Single layer graphene and bilayer graphene are identified electronically by means of probing the first member of the image potential derived state. This state is found by  $dZ/dV$  spectroscopy in the high energy unoccupied states and is exceptionally sensitive to electrostatic changes to the surface which is detected by energy shifts of image potential states (IPS). This sensitivity is utilized to probe the graphene screening of external electric fields by varying the electric field in the tunneling junction and addresses the fact that charged impurity scattering is likely to be crucial for epitaxial

graphene on SiC(0001) when it comes to transport parameters. Shifts of IPS energy position has also been used to verify work function changes for identification of several Sodium Intercalation structures of epitaxial graphene. STS, STM along with DFT calculations are used to determine the interface location of Sodium, SiC-bufferlayer or bufferlayer-graphene intercalation.

In this thesis, STM, and STS are used to study the interactions of paramagnetic FePc molecules with epitaxial graphene. The molecules, FePc, is found to interact with the graphene substrate where STM images show substrate induced orientation of FePc densely packed square lattice structure. At sub-monolayer coverages, FePc form a molecular gas at room temperature suggesting a low diffusion barrier on the graphene lattice. The substrate interaction is probed by STS and show an abnormally low LUMO energy that suggest strong electronic coupling between graphene and FePc. DFT calculations support the experimental observations and predict a spin-dependent molecule-graphene hybridization close to the Fermi energy in unoccupied states. For majority spins, DFT demonstrates the Dirac cone splits and a delocalized hybrid state is found in the band gap. For minority spin the Dirac cone is intact with energy of Dirac point empty.

In addition, a novel method of improving UHV graphene growth on SiC(0001) is presented. During growth the SiC surface is exposed to atomic hydrogen which allows selective etching of Si over Carbon. This result in more uniform non-thermal formation of the buffer layer with many fewer defects and thus leads to nearly pit-free and defect-free thermal graphene layers.

© Copyright 2012 by Andreas Sandin

All Rights Reserved

Tunneling Spectroscopy Studies of Epitaxial Graphene on SiC(0001) and Its Interfaces

by  
Andreas Axel Tomas Sandin

A dissertation submitted to the Graduate Faculty of  
North Carolina State University  
in partial fulfillment of the  
requirements for the Degree of  
Doctor of Philosophy

Physics

Raleigh, North Carolina

2012

APPROVED BY:

---

Daniel B. Dougherty  
Co- Chair of Advisory Committee

---

Marco Buongiorno-Nardelli

---

J.E. (Jack) Rowe  
Co- Chair of Advisory Committee

---

Ki Wook Kim

## **BIOGRAPHY**

Andreas Sandin was born in October 1979 in the town of Linköping, Sweden. After finishing his upper secondary school in natural science 1997 Andreas started training for his childhood dream, to become a scuba diver in the Swedish navy. In December of 1999 he accomplished his dream and successfully graduated from navy's Special Forces: the 1st mine clearance diver squadron in Skredsvik located on the Swedish west coast. After completed military service Andreas continued his academic career in 2002 at Lund University in the south of Sweden to study his favorite subject of physics. In 2008 he was awarded Master of Science in engineering physics after he spent the last year in North Carolina completing his Master thesis in the surface science group at NCSU lead by Professor Jack Rowe and Professor Bob Nemanich. Andreas was very passionate about his research and could not decline the offer to stay with Professor Rowe to pursue his PhD in physics to lead the operation of a study of surface and interfaces of the novel material graphene. In close collaboration with a new talented Professor, Dr Daniel Dougherty, Andreas successfully defended his PhD Thesis in May of 2012.

## ACKNOWLEDGEMENTS

It has been my immense pleasure to work with my advisors and other graduate students during my stay here at NCSU. Collaboration, support and teamwork is paramount in order to succeed in any work environment and I would here like to take the opportunity to acknowledge key persons that made my research project successful and enjoyable.

First and most importantly I want to send a special thanks to my advisors Dr Jack Rowe and Dr Daniel Dougherty. I have had the great honor to work closely with both Jack and Dan whom have given me unique and versatile guidance through my studies. Jack is the well established researcher with an impressive long background in surface science whereas Dan is in the early stage of his career very enthusiastic about pursuing exciting state-of-the-art research.

Jack was the one who hired me as a research assistant and first introduced me to the lab. With his experience he has an ability to see the big picture of each projects, something that may not be as straightforward for a graduate student. He has always believed in me even through difficult times as the life of a scientist can be. It has been a great honor to have him as my chair member in my committee.

Dan is a new professor at NCSU and with his talent and modern way of thinking about science he has motivated me and taught me a lot. Dan is not only very smart and

knowledgeable he also possesses a fantastic ability to communicate and show respect for all graduate students. I see him as a rare example of a new generation researcher that is hard working and can bring out the best of each individual student. I have no doubt Dan will become a successful and famous professor in the field of surface science in the future.

I want to thank Alex Pronschinske whom I collaborated with in the lab. Alex is a talented student and I have enjoyed many of our fruitful discussions.

Finally I want to send many thanks to my parents back home in Sweden. My mother Eva and my father Tomas, you have always been there to support me during all my years in school. I am fortunate to be your son and without you I would never have been able to reach this far.

## TABLE OF CONTENTS

<b>1: INTRODUCTION.....</b>	<b>1</b>
1.1 Graphene - General Importance .....	1
1.2 Background to the Discovery of Graphene .....	4
1.3 Epitaxial Graphene on SiC - Path Towards Applications .....	6
1.4 Motivation .....	7
1.5 Scope of This Dissertation.....	8
<b>2: MATERIALS .....</b>	<b>10</b>
2.1 Properties of Silicon Carbide.....	10
2.1.1 Atomic Structure of SiC .....	12
2.1.2 Hexagonal SiC Surface (0001) .....	14
2.2 Graphene - Allotrope Structure & Electronic Description .....	16
2.2.1 Graphene on SiC(0001) .....	22
2.2.2 Charge Transport in Graphene .....	25
2.2.3 Disruption of Graphene Band Structure .....	28
2.3 Proposed Future Graphene Devices .....	31
<b>3: EXPERIMENTAL METHODOLOGY .....</b>	<b>35</b>
3.1 Auger Electron Spectroscopy .....	36
3.1.1 The Auger Process .....	36
3.1.2 Detection of Auger Electron Energies .....	39
3.1.3 Graphene Thickness Measurement Using Auger Spectroscopy .....	43
3.2 Low Energy Electron Diffraction .....	44
3.2.1 Four-Grid LEED System.....	45
3.2.2 Kinematic Theory of LEED.....	46
3.2.3 Interpreting LEED Pattern .....	49
3.3 Scanning Tunneling Microscopy - Techniques and Principles .....	51
3.3.1 Basic Setup and Principles .....	51
3.3.2 The Physics of Tunneling .....	54
3.3.3 Constant Current Mode – Types of STM Images.....	56
3.3.4 Imaging SiC and Graphene with STM – Bias Voltage Dependency.....	58
3.4 Spectroscopy Using STM Tunneling Current .....	59

3.4.1	<i>Current-Voltage Spectroscopy (I-V)</i> .....	59
3.4.2	<i>Tip-Sample Distance-Voltage Spectroscopy (Z-V)</i> .....	61
<b>4:</b>	<b>SELECTIVE Si-ETCHING ON SiC(0001) BY ATOMIC HYDROGEN TO AVOID PIT-FORMATION DURING GRAPHENE GROWTH.....</b>	<b>64</b>
4.1	Abstract.....	65
4.2	Introduction to Selective Si-Etching on SiC(0001) by Atomic Hydrogen to Avoid Pit-Formation During Graphene Growth.....	65
4.3	Experimental Procedure .....	68
4.4	Results and Discussion .....	69
4.5	Conclusion.....	80
<b>5:</b>	<b>INCOMPLETE SCREENING BY EPITAXIAL GRAPHENE ON THE Si FACE OF 6H-SiC(0001) .....</b>	<b>81</b>
5.1	Introduction to Image Potential States.....	82
5.2	Abstract.....	85
5.3	Introduction to Incomplete Screening by Epitaxial Graphene on the Si Face of 6H-SiC(0001) .....	86
5.4	Methods .....	88
5.5	Results and Discussion .....	91
5.6	Further Discussion.....	95
5.6.1	<i>Image Potential States of Epitaxial Graphene Interface Layer</i> .....	96
5.6.2	<i>Image Potential States and its Correlation to Work Functions</i> .....	99
<b>6:</b>	<b>COMBINED THEORETICAL-EXPERIMENTAL STUDY OF IRON PHTHALOCYANINE ON GRAPHENE .....</b>	<b>102</b>
6.1	Abstract.....	103
6.2	Introduction to Combined Theoretical-Experimental Study of Iron Phthalocyanine on Graphene .....	104
6.3	Methods .....	107

6.4 Results and Discussion – Theory.....	109
6.5 Results and Discussion – Experiments.....	110
6.5.1 <i>Monolayer coverage</i> .....	111
6.5.2 <i>Sub-Monolayer Coverage</i> .....	114
6.5.3 <i>Tunneling Spectroscopy</i> .....	116
6.6 Summary.....	117
<b>7: MULTIPLE COEXISTING INTERCALATION STRUCTURES OF SODIUM IN EPITAXIAL GRAPHENE-SiC INTERFACES .....</b>	<b>119</b>
7.1 Abstract.....	121
7.2 Introduction to Multiple Coexisting Intercalation Structures of Sodium in Epitaxial Graphene-SiC Interfaces .....	121
7.3 Experimental Methods.....	124
7.4 Computational Methods .....	125
7.5 Results and Discussion .....	126
7.6 Summary and Conclusions .....	134
7.7 Further Discussion.....	135
7.7.1 <i>Dynamics of Intercalation</i> .....	136
7.7.2 <i>Selective Intercalation of Na on Single Layer Graphene</i> .....	138
7.7.3 <i>Triangular Defect Structure of Decoupled Buffer Layer</i> .....	140
<b>8: REFERENCES.....</b>	<b>144</b>

## LIST OF FIGURES

- Figure 2.1** The two basic units of the SiC crystal with interconnected tetrahedrons. (a) eclipsed configuration and (b) A  $60^\circ$  twisted configuration. Stacking of only twisted bilayers gives a cubic SiC crystal and a mix of them both results in hexagonal 4H and 6H SiC crystal structure..... 12
- Figure 2.2** (a) A single bilayer of SiC with Si atoms in a sublayer above the C atom sublayer. Each bilayer is perpendicular to the [0001]. (b) Bilayer stacking sequence (highlighted in red) of ABC for 3C-SiC with only twisted tetrahedrons modifications, hence a cubic lattice. (c) Hexagonal structure for 6H-SiC with stacking ABCACB sequence with one eclipsed tetrahedral at center height resulting in hexagonal structure. (a-c) taken from [26]. (d) Unit cell of 6H-SiC with the parameters:  $a_{\text{SiC}}=b_{\text{SiC}}=3.08 \text{ \AA}$ ,  $c_{\text{SiC}}=15.12 \text{ \AA}$ . Taken from [27]. ..... 13
- Figure 2.3** (a) Possible bulk terminated surface layer stacking sequences on 6H-SiC(0001) projected in the  $(1\ 1\ \bar{2}\ 0)$  plane. S1, S2 and S3 are identical to S1\*, S2\* and S3\* except for a  $60^\circ$  rotation. Integers indicate the number of twisted oriented bilayers directly at the surface before the occurrence of an identical bilayer rotation. Taken and modified from [29]. (b) Si-adatoms in T4 positions for SiC( $\sqrt{3}\times\sqrt{3}$ )R30 surface reconstruction. Taken from [30]..... 15
- Figure 2.4** (a) Graphene real space unit cell spanned by unit vectors  $\mathbf{a}_1$  and  $\mathbf{a}_2$  containing 2 atoms, one from each A and B sublattice. Nearest neighbor distance vectors are defined as  $\delta_i$  ( $i=1,2,3$ ) (b) Reciprocal graphene space; Brillion cell, primitive reciprocal-lattice vectors  $|b_1|=|b_2|=2\pi/a$  and zone boundaries and high symmetry points..... 17
- Figure 2.5** (a) Fermi surface of graphene by the tight-binding model. The Fermi surface vanishes where the valence band and conduction band meet at the so called Dirac point. The blow up shows the linear dispersion (Dirac cones) for the  $\pi$ -bands close to the Dirac point. (b) Band structure of graphene from ab initio calculations along high symmetry lines in the 2D Brillouin zone. Here all bands are visible including contributions from  $\sigma$ -bonds. The linear energy dispersion from  $\pi$ -bonds can be seen near the Fermi level at the K point. Taken from reference [27]..... 20
- Figure 2.6** (a) From ref. [37]: ARPES of buffer layer and (b) graphene grown on top of buffer layer. (c) From ref. [36]: Photoelectron intensity at the Brillouin zone K-point of buffer layer and (d) the epitaxial graphene. (e) Structural model of the SiC-buffer layer interface and SiC-graphene interface ..... 24
- Figure 2.7** Pseudospin for Dirac-like fermions in  $K'$  and K valleys in graphene. Small momentum backscattering becomes inefficient since it requires a flip of the pseudospin. A hopping in between valleys is possible without having to flip

the pseudospin (pseudospin backscattering). Note that there are two bands crossing each other which gives a “chirality” of the valleys with the pseudospin. .... 26

- Figure 2.8** (a) Schematic side-view of AB stacked graphene layers in graphite. Shaded area shows graphite unit cell with participating atoms from 3 layers and 2 different positions for each graphene sublattice: A, A', B, B'. Interlayer distance is 3.5 Å (b) STM of graphite imaged at Bias = -10 mV, I = 1 nA where  $\pi$ -orbitals from one toplayer sublattice protrude more than the second sublattice due to AB-stacking discussed in the text. Superimposed is the full honeycomb cartoon structure from both sublattices. (c) Schematic top-view of the two top-most layers in an AB-stacked graphite structure. .... 30
- Figure 2.9** (a) Electron Veselago lens based on graphene n-p-n junctions. By varying the charge carrier density in the p-type region by a top gate, an electron point source in one n-type region can be focused to desired position in the opposite n-type region. (b) Beam-splitter with prism-shaped p-region. From ref. [56]. .... 33
- Figure 3.1** UHV multi purpose system with two separated chambers. The methods used in this work were LEED, Auger and STM, all located in the analysis chamber. .... 35
- Figure 3.2** Schematic illustration of a typical Auger transition process. The participating electron shells are a core shell (K) and shells close to the Fermi level,  $L_1$  and  $L_2$  in this case. Image taken from [61]. .... 37
- Figure 3.3** Signal and data processing for AES analysis. (a) CMP connected to a channeltron. (b) Basic principles of a lock-in amplifier (single phase): A known reference signal is multiplied by the in-signal. An integrator acts as a low-pass filter which gives the output proportional to one half the amplitude of the signal derivative. Image (a) taken and modified from [66]. .... 40
- Figure 3.4** Modulation used to increase signal to noise ratio in AES analysis. (a) Typical spectra from the electron distribution,  $N(E)$ . (b) Signal is modulated by a high frequency, low amplitude signal allowing to measure  $dN(E)/dE$ . (c) The first derivative of modulation gives a clear AES spectrum. Image taken from ref [66]. .... 42
- Figure 3.5** Estimated graphene layers versus Auger peak-to-peak ration of the Si(LVV)/C(KLL). The image is taken from ref. [66] but corrected for the intermediate carbon-rich buffer layer that is always present underneath the epitaxial graphene grown on SiC. The zeroth layer simply corresponds to the buffer layer. .... 43
- Figure 3.6** Variations in mean escape depth of various materials as a function of electron energy. Taken from ref. [68]. .... 45
- Figure 3.7** (a) Diagram of a four-grid reverse view LEED system optics. (b) Atomic scale image in 1D of the electron beam impinging and scattered off an ordered sample surface with lattice spacing  $a$ . Laue Conditions for the normal incidence

electrons are fulfilled if the phase shift  $d = a \cdot \sin \theta$  equals an integer number of the electron wave length,  $\lambda$ . ..... 46

**Figure 3.8** (a) The Ewalds-sphere construction in LEED viewed parallel to the surface. (b) Real space setup of LEED. The blue triangles are analogous in the two images and determine a direct mapping of the reciprocal lattice spot projected on a phosphor screen..... 48

**Figure 3.9** Simplified schematic view of an STM. The tip is scanned in the two lateral dimensions while a feedback circuit is constantly adjusting the tip height to keep the current constant. The voltage supplied to the piezo drivers produces the path of the tip which gives an image of the shape of the surface. Taken from [75]. ..... 52

**Figure 3.10** Schematics of potential barrier between electrodes for vacuum tunneling. (a) Two electrodes with slightly different work functions are brought to close proximity so that electrical equilibrium, i.e. a common Fermi level ( $E_F$ ), is established. (b) A bias voltage  $eV$  is applied which will cause the Fermi levels to differ by  $eV$  and enable current. The sample states between energy level  $E_F - eV$  and  $E_F$  can tunnel to the tip and generate a tunneling current. The schematic illustrates tunneling of one of such state with the wave function  $\Psi_n$  with energy  $E_n$ . (c) The tip-sample distance is defined between the topmost tip atom with respect to the nucleus of the nearest atom of the sample. Image taken and modified from [76]. ..... 54

**Figure 3.11** Schematic of current-voltage (I-V) spectroscopy in STM. Taken from [81]..... 60

**Figure 3.12** Schematic of tip-sample distance-Voltage (Z-V) spectroscopy in STM. Taken from [81]. ..... 62

**Figure 4.1** (a) Auger electron spectroscopy of sample annealed to 850 °C (black curve) and same sample annealed to 900 °C for 3 minutes (red curve). (b) STM image of same sample annealed to 900 °C showing a bare SiC(0001) surface with step heights  $\sim 2.5$  Å. Note every third step is more rough and dissolved compare to the other steps. (c) Auger intensity ratio of Si/C peaks with respect to annealing temperature in UHV. At each data point a same sample has been annealed for 3 minutes. .... 70

**Figure 4.2** (a) STM image and line profile of sample annealed to 1050 °C in UHV.  $I=0.1$  nA,  $U=-2$  V. (b) Close-up from a of a step separated by S3 and S2 terraces where the surface is dominated by Si-rich  $\sqrt{3}$  on the S3 terrace with random carbon-rich  $6\sqrt{3}$  domains. (c) STM image and line profile of sample annealed to 1100 °C in UHV where surface has become severely roughened. (d) close-up from c showing surface is dominated by carbon-rich  $6\sqrt{3}$  with small domains of Si-rich  $\sqrt{3}$ .  $I=0.1$  nA,  $U=2$  V ..... 72

- Figure 4.3** (a) Atomic hydrogen etched surface at 1000 °C for 10 minutes at  $P=10^{-5}$  mB.  $I=0.1$  nA,  $U=-2.3$  V. (b) AES scan of hydrogen etched surface in a. (c) Same surface annealed to 1300 °C in UHV for 3 minutes.  $I=0.1$  nA,  $U=-1.9$  V. (d) Surface in figure 4.2 annealed to 1300 °C for 3 minutes.  $I=0.1$  nA,  $U=2$  V. .... 75
- Figure 4.4** (a) Sample exposed with atomic hydrogen for 45 minutes at 850 °C followed by a quick flash to 900 °C to remove native oxide. (b) AES of sample in a. (c) Different sample exposed with atomic hydrogen for 45 minutes at 900 °C. AES for this surface is shown in (d). Z-scale for both STM images is 1.3 nm. .... 78
- Figure 5.1** Inverse photoemission spectra for Au(111), Ag{111}, and Cu(111) for normal electron incidence. Image potential states are denoted IS. Taken from [105]..... 84
- Figure 5.2** (a) STM image (36nm x 36nm) of coexisting single layer and bilayer graphene; (b) Line profile across the blue line marked in part a showing the apparent height variation across the SLG to BLG boundary; (c) Schematic depiction of an electron bound just outside of a surface by polarization it induces; (d) Schematic depiction of (Stark shifted) image potential derived states (horizontal red lines) in an STM experiment where a potential well is created by the combined image potential and linear potential between the tip and sample. .... 89
- Figure 5.3** Changes in IPS's due to unintended tip changes; (a) Single layer graphene; (b) Bilayer graphene measured with the same two tip conditions as in part a. .... 90
- Figure 5.4** (a) Current dependent distance-voltage spectra measured for SLG; (b) Current dependent distance-voltage spectra measured for BLG with the same tip condition as in part a); (c) Current dependent position extracted for the  $n=1$ -state of SLG (open symbols) and BLG (closed symbols). Dependencies for two different tip conditions (triangle versus squares) are shown. .... 92
- Figure 5.5** Differentiated constant-current distance-voltage spectra measured for buffer layer at two different samples. Currents; Tip A: 0.2 nA, Tip B: 0.1 nA ..... 97
- Figure 5.6** (a) Differentiated constant-current distance-voltage spectra measured with identical tips comparing (a) SLG with BLG and (b) buffer layer with SLG..... 101
- Figure 6.1** Results of DFT calculations. (a) Individual spin-band structures of FePc on graphene. Dirac cone is intact and empty for spin up while Dirac cone is split and empty for opposite spin. A mixed graphene-molecule state is present at the Fermi level marked in green. (b) side-view of LUMO orbitals originating from mixed graphene-molecule state of spin down. (c) Individual spin bandstructures of CuPc on graphene. (d) Relaxed computational cell of a FePc molecule lying flat in on-top site with a C atom in the graphene. Red=Fe, blue=Nitrogen, black=carbon and white=hydrogen. For calculations with CuPc only the center metal Fe atom is replaced with a Cu atom..... 110

- Figure 6.2** (a) Single domain of square close-packed FePc on both single- and bilayer graphene,  $U=1.5$  V,  $I=50$  pA (b) close-up of a differently oriented square close-packed FePc domain showing the unit vectors A and B separated by  $\sim 90^\circ$ ,  $U=1.3$  V,  $I=50$  pA. .... 111
- Figure 6.3** (a) LEED of clean graphene on SiC(0001),  $E=14$  eV. (b) LEED of monolayer FePc on graphene on SiC(0001),  $E=14$  eV. Reciprocal lattice vectors for one out of six identical but differently oriented FePc domains on the graphene marked with white arrows. Purple line shows the direction of a graphene reciprocal lattice vector. (c) Atomic model of the real space FePc lattice on top of the graphene lattice. Unit vectors have magnitude  $A=1.37$  nm,  $B=1.30$  nm both separated by  $90^\circ$ . .... 113
- Figure 6.4** (a) Molecular gas of FePc at sub-monolayer coverage at room temperature. (b) Boundary of ordered FePc(left side) molecules with FePc molecule gas (right side of image). (c) Same coverage as in (a) but at 110 K showing a boundary of close-packed FePc molecules and bare graphene (lower right corner). .... 115
- Figure 6.5**  $dI/dV$  spectroscopy of monolayer FePc on single layer graphene on SiC(0001) (blue curve) on SiC(0001) and monolayer FePc on graphite (red curve). .... 116
- Figure 7.1** STM images of Na intercalated between buffer and graphene layer, SiC/B/Na/G. (a) Low coverage Na chains ( $V=-2.18$  V,  $I=62$  pA); (b) Intermediate coverage with chains and islands. ( $V=-2.0$  V,  $I=50$  pA); (c) Na island in figure b with (6x6) quasi-cell indicated ( $V=-2.3$  V,  $I=50$  pA); Graphene lattice of island in figure c ( $V=-0.55$  V,  $I=350$  pA). .... 127
- Figure 7.2** STM images of Na intercalated at SiC interface after heating of sample: SiC/Na/G/G (a)-(c) and SiC/Na/G (d)-(f); (a)  $\sim 180^\circ$  C with full coverage SiC/Na/G/G ( $V=-1.93$  V,  $I=200$  pA); (b)  $\sim 530^\circ$  C showing an area of coexisting SLG, BLG, and SiC/Na/G/G ( $V=-1.7$  V,  $I=50$  pA); (c) Graphene lattice on SiC/Na/G/G ( $V=-0.37$  V,  $I=150$  pA); (d)  $\sim 180^\circ$  C with full coverage SiC/Na/G ( $V=-2.6$  V,  $I=50$  pA), (e) Triangular depressions covering SiC/Na/G surface ( $V=-1.8$  V,  $I=50$  pA); (f) Graphene lattice on SiC/Na/G ( $V=-0.14$  V,  $I=0.11$  nA). .... 128
- Figure 7.3** Differentiated ( $dz/dV$ ) distance-voltage spectra  $z(v)$  of the  $n=1$  IPS for different intercalation structures relative to the  $n=1$  IPS on SLG (red). All spectra are recorded with a constant current set-point of 50 pA. .... 130
- Figure 7.4** Calculated electronic bands- and atomic structures for (a) SLG on top of SiC(0001); (b) SiC/B/Na/G (c) SiC/Na/G/G (Layers are AB-stacked); and (d) SiC/Na/G. Yellow atoms are C, black are Si, and red are Na. (e) Shift in measured  $n=1$  IPS energy (blue squares) and shift in calculated work function from SLG (green circles) for each intercalation structure. .... 133

- Figure 7.5** (a) Submonolayer Na deposited on buffer layer where the sodium avoids small domains of coexisting single layer graphene. For clarity some SLG domains are marked SLG in blue color. (b) Submonolayer deposition of Na single layer graphene while avoiding small domains of coexisting bilayer graphene. Bilayer domains marked as BLG in green text. .... 139
- Figure 7.6** From ref [200]. (a) STM image of epitaxial graphene on 6H-SiC(0001) with the two different types of defects occurring at the buffer layer SiC interface: trimer-like marked with blue triangle and rousette-like marked with green hexagon.  $E=-0.1$  V,  $I=0.3$  nA (b) Proposed model of buffer layer  $(6\sqrt{3}\times 6\sqrt{3})R30$  unit cell with  $H_{5,6,7}$  top and hollow defects without causing dislocations. (c-d) Calculated DOS isosurfaces for occupied states between  $-0:1$  eV and the Fermi level for the (c) top and (d) hollow variants. Carbon atoms are represented by small balls; Si, by larger balls. .... 141
- Figure 7.7** (a) Surface of coexisting epitaxial graphene (SiC/B/G) and SiC/Na/G) trimer top site defects shown as small protrusions in (SiC/B/G) and triangular defects seen as depressions on (SiC/Na/G). (b) (SiC/Na/G) coexisting on both S and S\* bulk SiC surfaces where the two possible orientations of the triangular defects are marked out in green color. .... 142

## **1: INTRODUCTION**

I would like to start off by introducing the reader to the field of graphene by giving a motivation of why it is important to conduct research on this novel 2D electronic material. I will mention the important events in the history of graphene where common sense was flaunted by the experimental discovery of isolated graphene. Special remarks are given to the bright scientists who realized the potential in graphene through their groundbreaking experiments. I will finish this chapter by motivating the study of graphene grown epitaxially on SiC and finally specify and outline the scope of my own work in this field.

### **1.1 Graphene - General Importance**

The electronics industry is constantly searching for materials that can improve device properties in order to build faster and better computers, cell phones, television and computer screens etc. A corporate competitive market fight to be able to offer the best product for the increased need of data processing in the society as whole.

Today's building blocks for electronic circuits are made out of single crystal Silicon and ever since the first silicon transistor was demonstrated by Texas Instruments in 1954, the world has witnessed a remarkable technological revolution when it comes to computer performance.<sup>1</sup> The present day technology is based on silicon with the complimentary-metal-oxide-semiconductor (CMOS) circuits consisting of a source, drain and a gate to accommodate electron flow.<sup>2</sup> It is by the gate the current flow from source to drain can be controlled, this current is a two-dimensional-electron-gas (2DEG) channel manipulated by an

applied electric field from an on state (current flow) to an off-state (no or drastically reduced current flow). This transistor design is thus called a field-effect transistors (FET) and is the corner stone for essentially all integrated circuit (IC) components in electronic devices.

Improved scaling and packing of these transistors has allowed for a remarkably increased device performance per spent dollar. In 1965 IC chips containing about 2000 transistors were available. In 2001 the Intel Pentium 4 processor held 42 million transistors and Intel's latest production line introduced in 2011 hold 1.16 billion transistors per chip. This development roughly follows the famous Moore's law which is a prediction formulated by Intel co-founder Gordon Moore in 1965 stating that approximately every 2 year transistor density will double.<sup>3</sup> The benefit of this minimization and more efficient packaging of transistors intuitively give more powerful processors for today's small hand-held devices such as smart phones, tablets or other electronic gadgets. However, even more importantly than saving space is that the switching speed of each transistor is dramatically increased as the effective size of each transistor shrink, i.e. the channel length between source and drain. Today's state of the art transistors have an impressively small channel length of about of 20 nm. However further reduction of the channel length causes inevitable leakage currents which makes the transistor difficult to turn off. In addition increasing of transistor scaling makes it difficult to prevent the chip from over heating due to the increase in switching power.<sup>2</sup>

Graphene is a new interesting material that can potentially change the landscape for future nanoelectronics. It has received a huge attention mainly because the charge carriers in

graphene behave as a 2DEG as in a MOS-FET but now are truly spatially confined due to the two-dimensional structure of graphene crystal.<sup>4</sup> The 2DEG in graphene is in fact far superior the electronic properties of a 2DEG in a MOS-FET with a dramatically improved electron and hole charge mobility. The mobility in graphene is about 100 times larger than Silicon at room temperature even for high concentrations induced by electric fields. In a CMOS-circuit each type carrier (electrons or holes) is used but mobility is only high for one type of carrier. In graphene both holes and electrons have essentially equally good mobility. If graphene is used in a traditional CMOS-FET it results in charge carriers with ballistic transport as they travel extremely coherently from the source and drain meaning they will completely avoid diffusive scattering on the scale of the transistor active channel length.<sup>5</sup> This suppression of scattering results in less heat dissipation which is one of the biggest issues with Silicon-based integrated circuits today.

These aspects are good examples of how graphene can improve today's transistors; however graphene possess even more interesting properties that can be incorporated into other technology devices. The graphene 2D crystal is not only a good conductor but it is also extremely strong<sup>6</sup> while being flexible and transparent.<sup>7</sup> This makes graphene useable in all kinds of applications which require transparent electrodes such as touch screens and solar cells. The reader may now start to realize that there are almost an infinite number of high-tech applications that can benefit from the properties of graphene which subsequently can boost the field of information technology. As a consequence this translates into a stimulus of the world electronics economy beneficial for the whole society since the information

technology has accounted for 25 % of the overall world economic growth since 1995 and it contributes to the world productivity growth more than all other industries combined .<sup>8</sup> This explains why graphene is so important to study and it is now up to researchers and scientists across the world but learn how to master the untapped resources hiding in the unique 2D crystal of graphene.

## **1.2 Background to the Discovery of Graphene**

A single layer of  $sp^2$  bonded carbon atoms arranged in a hexagonal pattern is defined as graphene. Such 2D carbon fullerene was argued in the 1930's by Landau not to be thermodynamically stable because of a rapidly decreased melting point with decreasing thickness and could therefore not exist.<sup>9</sup> Being considered as only stable as an integral part of thicker crystals that of graphite, Professor P. R. Wallace calculated the band structure of individual graphene layers using the simple tight-binding model.<sup>10</sup> In 1947 the theory showed that an isolated graphene layer had very unique electronic band structure around the Fermi level because the energy versus momentum has a perfect linear dispersion. For some of the above described reasons it was scientifically groundbreaking when experiments demonstrated in the 1990's that a single graphene layer could exist rolled up in the form carbon nanotubes (CNT).<sup>11,12</sup> These nanotubes were found to have extremely good electronic properties such as room-temperature ballistic conductivity<sup>13</sup> and excellent field effect transistor (FET) characteristics<sup>14</sup> which triggered an intense research with the visualization of CNT's as building blocks for future nano-electronic circuits. However today, about 20 years

later the interest for CNT's has declined because of the difficulties involved of precise and repeatable control the growth at the nano scale.

As recent as 2004 carbon fullerene research took a remarkable and unexpected turn as researchers in Manchester, UK lead by the Russian physicists Alexander Geim and Konstantin Novoselov were able to isolate graphene using a surprisingly straightforward method. They simply peeled of flakes from a graphite crystal using scotch tape and subsequently rubbed it on to a Silicon-Silicon Oxide sample from where they could identify single layers in an optical microscope.<sup>15</sup> A SiO<sub>2</sub> layer directly beneath graphene flakes served as an optical path for the microscope light to reflect at the Si interface and a monolayer graphene adds up sufficiently to the path in order to induce a phase contrast that could distinguish graphene from thicker flakes. Monolayer graphene flakes with sizes around 10 μm was obtained having high crystal quality and macroscopic continuity. Such samples allowed the Manchester scientists to explore the quantum physics of graphene and demonstrate its remarkable electronic properties.<sup>5, 16, 17</sup> Graphene share all the unique and favorable properties of carbon nanotubes and the planar 2D structure of graphene enable wider diversity for layered device geometries and can be directly incorporated into today's developed circuit design with standard lithographic techniques. In 2010 Geim and Novoselov was awarded the Nobel Prize for the discovery and their groundbreaking studies on graphene.

### 1.3 Epitaxial Graphene on SiC - Path Towards Applications

Peeling of flakes from graphite using scotch tape is rather straightforward technique for a lab environment to study the electronic properties of graphene. However it is not a process that is adoptable to scale up for industrial manufacturing. Alternative methods have to be explored in order to grow graphene controllably and uniform at least on a wafer-size scale. It was the same year as Geim and Novoselov discovered the graphene as a research group lead by Professor Walt de Heer at Georgia Tech University discovered that graphitized SiC surfaces demonstrated excellent 2DEG properties.<sup>4</sup> They created there ultra-thin graphite films by heating up the polar surface SiC(0001), a procedure that has been know since 1975 when Van Bommel observed what he called “monolayer graphite” on the SiC(0001) surface.<sup>18</sup> The technique is rather unambiguous: upon annealing of SiC to temperatures above  $\sim 1000$  °C Si atoms starts to sublime and leave off excess carbon at the surface. With higher annealing temperatures the Si sublimation is accelerated and sufficient released carbon forms graphitic bonds at temperatures around  $1200$  °C arranging in large lateral and unified oriented domains. De Heer’s pioneering electronic measurements on this surface<sup>4</sup> in conjunction with the Geim and Novoselovs discovery of isolated graphene<sup>16</sup> lead to the development of the field *epitaxial graphene* on SiC. Epitaxial graphene has been a subject of considerable research because it is one of the most promising and viable route towards graphene industrial production and commercialization via controlled bottom-up growth. In addition, from a technological application point of view, SiC has insulating properties which makes it a suitable substrate for supporting graphene.

Epitaxial graphene is supported by an interfacial layer carbon rich layer to the SiC which makes this system more complex than exfoliated graphene deposited on SiO<sub>2</sub> but not necessarily less interesting. The interface can be manipulated for instance by intercalation which makes epitaxial graphene on SiC an exceptionally versatile system for exciting surface science research.

## **1.4 Motivation**

When I started this PhD study at North Carolina State University in 2009 I immediately found the field of graphene extremely promising and exciting. The reasons for this was mainly because the simplicity of graphene atomic structure. It is easy to imagine and interpret a two dimensional crystal only consisting of one of this galaxy most abundant element, carbon. Adding to that such a simple crystal was awarded the Nobel Prize for its unique electronic properties just a year after I started my PhD research on graphene which made my work even more so motivating and timely. Even though graphene is just an infant experimentally most of the work of exploring the fundamental intrinsic physics in graphene has moved rapidly forward in the last years and can be considered as an accomplished task. New research needs now to be focused on to understand how graphene production can be optimized and how graphene reacts to various interfaces in order for it to be utilized in device structures. The choice of substrate to support graphene, functionalization compounds for electronic tailoring or metal contacts for device construction has proven to be particularly difficult as the graphene is exceptionally sensitive to any disturbance of the natural electronic state.

My research in this Thesis was conducted to gain alternative insights on how to improve graphene growth mode, how to chemically modify, functionalize and electronically characterize graphene interfaces in the system epitaxial graphene on SiC(0001). My methods and techniques used differs most of the times significantly from the “main stream” research in surface science and involves several novel discoveries outlined in the thesis scope summary in the next section. My hope it that my studies can open up new perceptivity and understanding towards future carbon-based electronic devices built from the SiC-graphene platform.

## **1.5 Scope of This Dissertation**

This thesis is a partial fulfillment of the requirements for the degree of Doctor of philosophy in physics at North Carolina State University. In this first chapter I have given a brief introduction to graphene as well as the motivation and objects for this study.

I will move on in the following chapter 2 to give a more detailed theoretical background to both Silicon Carbide and Graphene.

Chapter 3 contains a description of the experimental methods used. These are mainly the scanning tunneling microscope (STM) and Scanning Tunneling Spectroscopy (STS) but also Auger electron spectroscopy and low energy electron diffraction (LEED). My main research projects and results are further presented in the remaining part in the form of a short chapter introduction followed by an outline arranged as individual scientific reports.

Chapter 4 will cover a novel technique that I have developed to improve the growth of graphene on SiC(0001) using atomic hydrogen. This method is very different from today's

state of the art growth processes and offers the possibility to use solely hydrogen in a complete quasi-free graphene manufacturing cycle.

Chapter 5 describes indirect screening measurements of epitaxial single and bilayer graphene by probing their corresponding image potential derived states. The STM-tip in these experiments serves as a “charged impurity” that is inferred to be poorly screened by the surrounding graphene. Consequently this suggests that issue of charge impurities being a limiting factor of transport properties in exfoliated graphene on SiO<sub>2</sub> may also be critical for epitaxial graphene on SiC.

Chapter 6 presents a study of paramagnetic molecules (Iron-Phthalocyanine) structure and electronic interaction with graphene. The graphene-magnetic molecule interface is particularly important because of its potential to play an important role in proposed spin-graphene devices. In fact graphene offers not only exceptional electronic conductance it is also a suitable medium for carrying spin for relatively long time and distances. Magnetic molecules may enhance spin injection into the graphene as graphene is suggested to serve as the active channel in future spin field effect transistors.

Finally in chapter 7 I will present work involving epitaxial graphene-SiC(0001) intercalation of Sodium. Intercalation of this interface is a new emerging sub-field of epitaxial graphene and has a remarkable impact on both interfacial atomic and electronic structure, unique for the SiC-Graphene interface. I find this field particularly interesting and will here present the world’s first study of atomic-scale scanning probe imaging of several new intercalation structures that can exist for graphene grown on SiC.

## **2: MATERIALS**

A material background will be here be given for SiC and graphene. Emphasis will lie on the theory of the unique properties of graphene which explains the motivation for studying this novel material. A brief explanation will also be given on how these properties can be utilized for electronic applications and what possible drawbacks graphene suffers from on this aspect. The SiC substrate which serves as both an insulating substrate as well as carbon source will also be reviewed.

### **2.1 Properties of Silicon Carbide**

Single crystal Silicon carbide (SiC) is a semiconductor capable to operate at more harsh environments compared to other traditional semiconductors such as Silicon and Gallium Arsenide (GaAs). Its high saturated electron drift velocity<sup>19</sup>, high thermal conductivity<sup>20</sup> and large breakdown electric field strength<sup>21</sup> make SiC useable in high power devices. These properties can mainly be explained by the large indirect bandgap of SiC of around 3 eV compared to 1.1 eV for Si and 1.4 eV for GaAs. The thermal ionization of electrons from the valence band to the conduction band is by a wide band gap much more comprehensible to avoid intrinsic carrier concentrations exceeding doping levels which will impede the functionality of a semiconductor. As a result SiC offer a wide temperature functional range with the ability to effectively dissipate large thermal power densities. Further, SiC is both physically and chemically robust and can essentially withstand all wet chemical etchants at room temperature.

The production of single crystal SiC is far less mature compared to the Silicon production. It wasn't until the early 1990's before enough high-quality single crystals of SiC wafers became commercially available because traditional methods developed for Si growth cannot be adapted to SiC due to the lack of a SiC liquid phase. Therefore new growth techniques had to be considered that are based on high temperature sublimation of SiC powder or more expensive chemical vapor deposition (CVD) procedures<sup>22</sup>, methods that are still subject for considerable research for refinement and crystal quality optimization. The development of SiC electronic devices has been limited by crystal defects such as edge and screw dislocations and in addition, the task of forming a uniform interface of SiC with silicon dioxide has proven to be difficult and has further hampered the development of SiC-based power MOS-FETs.<sup>23</sup>

Today, wafer sizes of SiC(0001) up to 4 inches are commercially available but the cost per wafer exceeds by far the cost of Si wafers by a factor of more than 100; which inhibits production of cost-effective SiC-based technology and accessibility for SiC research. The most remarkable industrial application of SiC was the first blue light emitting diode (LED) but these were soon surpassed in intensity by direct bandgap III-nitrides like GaN which are usually made on SiC wafers.<sup>24</sup> Recently commercial SiC MOS-FETs were introduced in 2011 by the company Cree in Durham, North Carolina that can operate up to 1200 V, 10 times higher than a Si MOS-FET, while allowing lower switching losses and higher temperature operation up to 200 °C.<sup>25</sup> This development will eventually open up a more wide spread commercialization of SiC-technology however epitaxial graphene grown on SiC could

potentially create a much larger demand and by so significantly accelerate the development and increase supply for cheap single crystal SiC raw material.

### 2.1.1 Atomic Structure of SiC

SiC is composed of equal Silicon and Carbon stoichiometry where each atom is bonded to four other atoms in tetrahedral  $sp^3$  hybridization. The tetrahedral is the smallest structural unit of either  $Si_4C$  or  $SiC_4$  where each element (Si or C) is positioned exclusively in sublayers where two adjacent sublayers make up one SiC bilayer.

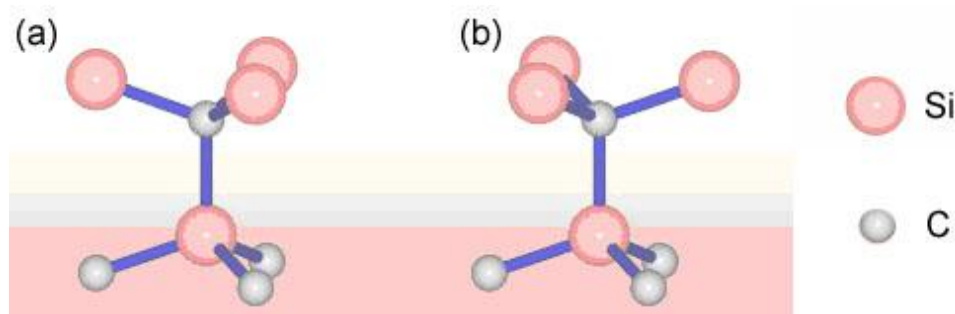


**Figure 2.1** The two basic units of the SiC crystal with interconnected tetrahedrons. (a) eclipsed configuration and (b) A  $60^\circ$  twisted configuration. Stacking of only twisted bilayers gives a cubic SiC crystal and a mix of them both results in hexagonal 4H and 6H SiC crystal structure.

Adjacent bilayers can exist in two types of subsequent configurations. They can either have the eclipsed orientation configuration (see fig. 2.1a) or be rotated by  $60^\circ$  with respect to each other as shown in fig. 2.1b. These two constellations have practically the same total energy and therefore bulk SiC exists in many types of stacking sequences, so called polytypes.

Identical stacking sequence of only the twisted configuration (fig. 2.1b) result in cubic diamond-like bulk SiC. With periodic feature of the eclipsed configuration will form a hexagonal wurtzite SiC structure. Polytypes are identified by the lattice symmetry and the number of bilayers in each repeatable bulk unit cell.

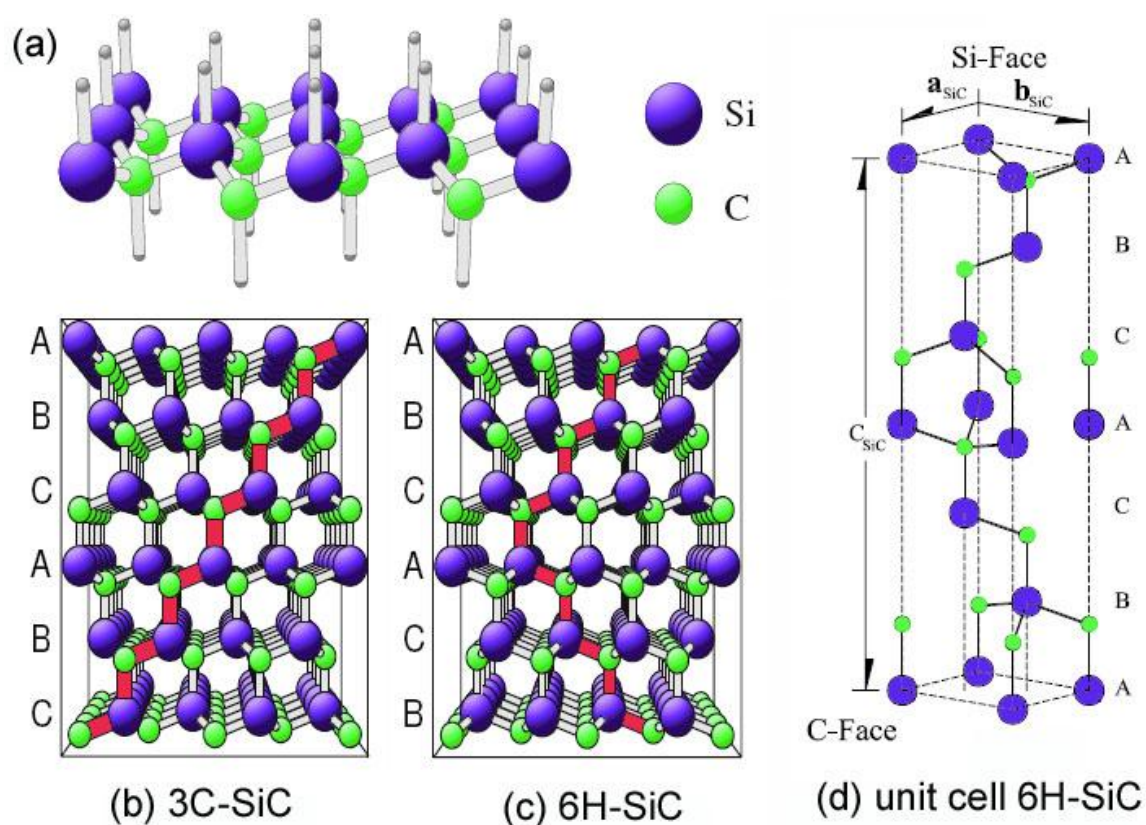


**Figure 2.2** (a) A single bilayer of SiC with Si atoms in a sublayer above the C atom sublayer. Each bilayer is perpendicular to the [0001]. (b) Bilayer stacking sequence (highlighted in red) of ABC for 3C-SiC with only twisted tetrahedrons modifications, hence a cubic lattice. (c) Hexagonal structure for 6H-SiC with stacking ABCACB sequence with one eclipsed tetrahedral at center height resulting in hexagonal structure. (a-c) taken from [26]. (d) Unit cell of 6H-SiC with the parameters:  $a_{SiC}=b_{SiC}=3.08 \text{ \AA}$ ,  $c_{SiC}=15.12 \text{ \AA}$ . Taken from [27].

The three most common polytypes are 3C (fig 2.2b), 4H and 6H-SiC (fig. 2.2c) where H stands for hexagonal, C for cubic and the integer corresponds to the number of bilayers in each bulk unit cell along the c-axis [0001] or [111] directions.

6H-SiC have six bulk truncated bilayers where the stacking sequence is ABCACB centered from one eclipsed bilayer configuration. 4H-SiC will have four bulk truncated surface structures for the stacking ABCB, also with one eclipsed bilayer configuration at each end of the stacking sequence.<sup>26</sup> In this Thesis, hexagonal 6H and 4H polytypes are used for growing epitaxial graphene. They differ only in bulk unit cell height  $c = 15.12 \text{ \AA}$  for 6H (see figure 2.2d) and  $c = 10.08 \text{ \AA}$  for 4H height of approximately  $2.5 \text{ \AA}$  for each SiC bilayer. Their surfaces are identical with unit cell parameters of the basal plane  $a=b=3.08 \text{ \AA}$  discussed in the following section.

### 2.1.2 Hexagonal SiC Surface (0001)

The two opposite basal plane surfaces normal to the polytype stacking direction are called the polar {0001} surfaces of SiC. One is Si terminated with one dangling bond for each Si surface atom (figure 2.2a) often denoted Si-face or SiC(0001) for crystallographic identification. Its opposite surface is geometrically identical but has a carbon terminated surface called the C-face, SiC(0001,<sup>-</sup>). Epitaxial graphene can be formed on both these two surfaces however the growth and graphene-SiC interface differs significantly between the two faces, even the multilayer graphene stacking is different on the C-face compared to the Si-face.<sup>27</sup> It should be mentioned that recent studies have reported on high quality graphene

grown on cubic 3C-SiC epitaxially grown on Si-wafers which may allow for integration of graphene on SiC into existing Si technology.<sup>28</sup>

In this Thesis, graphene grown on the Si-face SiC(0001) will be considered and there are two different surface configurations for hexagonal surfaces due to the mix of bilayer stacking configurations discussed in previous section. The two types are denoted S and S\* along with an integer to identify the number of identically ( $60^\circ$  twisted) stacked bulk truncated bilayers before the occurrence of a eclipsed bilayer configuration as in fig. 2.1a.<sup>29</sup> Consequently, 4H have four possible bulk terminated surface layer stacking sequences and 6H has six constellations: S1, S2, S3, S1\*, S2\*, S3\* (fig. 2.3a).

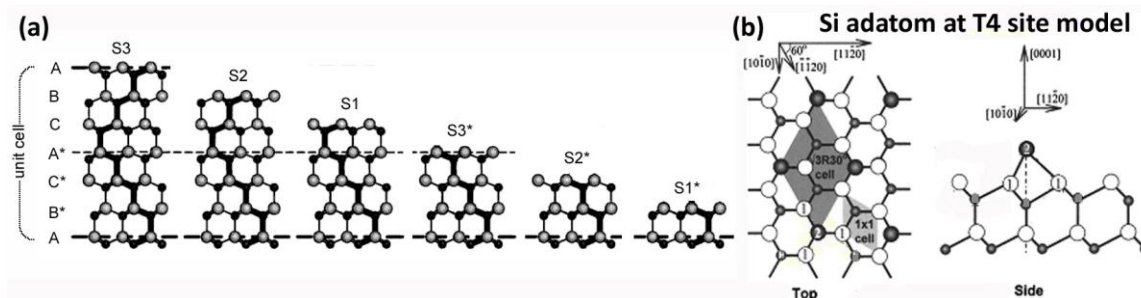


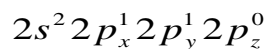
**Figure 2.3** (a) Possible bulk terminated surface layer stacking sequences on 6H-SiC(0001) projected in the  $(1\ 1\ \bar{2}\ 0)$  plane. S1, S2 and S3 are identical to S1\*, S2\* and S3\* except for a  $60^\circ$  rotation. Integers indicate the number of twisted oriented bilayers directly at the surface before the occurrence of an identical bilayer rotation. Taken and modified from [29]. (b) Si-adatoms in T4 positions for SiC( $\sqrt{3}\times\sqrt{3}$ )R30 surface reconstruction. Taken from [30]

The top most Silicon atoms make up the surface of bare SiC(0001). This surface forms a native oxide with immediate contact to ambient air which saturates dangling bonds, one for each Si surface atom. The oxide can be removed in UHV by annealing the surface to  $800^\circ\text{C}$

for 4H-SiC(0001) or 900 °C for 6H-SiC(0001) and with limited amount of oxygen present in a UHV environment the surface will form a Si-adatom SiC( $\sqrt{3}\times\sqrt{3}$ )R30 reconstruction with Si-adatoms in T4 sites (fig. 2.3b).<sup>30</sup> This surface is well studied mainly because of its importance for heteroepitaxy and homoepitaxy crystal growth on SiC. Considering the Si-rich SiC( $\sqrt{3}\times\sqrt{3}$ )R30 reconstruction as a clean initial surface, further annealing of this surface will result in Si atoms to sublime and more complex carbon-rich reconstructions will take form due to symmetry requirements to the SiC. One structure in particular, the SiC( $6\sqrt{3}\times 6\sqrt{3}$ )R30 is of great importance for epitaxial graphene formation and will be discussed further in section 2.2.1.

## 2.2 Graphene - Allotrope Structure & Electronic Description

A Carbon atom consists of 6 electrons with its ground state valence electron configuration being:



In a carbon crystal it is energetically favorable to form hybridized state where all four valence electrons (in the principle quantum number  $n=2$ ) participate in bonding. With complete degenerate hybridization a carbon network can form exclusively  $sp^3$  hybridization just like in SiC to form its most stable allotrope, diamond. In a  $sp^3$  carbon network all atoms form 4 bonds with stable covalent  $\sigma$ -bonds identified by their symmetry with respect to rotation about the bond axis and explain the hardness of diamond materials. The  $sp^2$  counterpart, marginally less stable but nonetheless very common, is a 2D crystal called graphene and is the building block for several dimensional carbon allotropes: buckyballs

(0D), carbon nanotubes (1D) and graphite (3D). The  $2p_x$  and  $2p_y$  hybridize with a  $2s$  orbital to form 3 strong  $\sigma$ -bonds oriented 120 degrees from each other in the plane and make up the 2D graphene crystal structure.<sup>31</sup> The remaining valence electron is left unhybridized and occupies the  $2p_z$  orbital pointed out of graphene plane. They form weak  $\pi$ -bonds with adjacent carbon atoms that, unlike the  $\sigma$ -bonds, overlap perpendicular to bond axis. The  $\pi$ -bonds play the dominant role in transport properties of graphene whereas the in-plane  $\sigma$ -bonds are responsible for high mechanical strength and robustness.

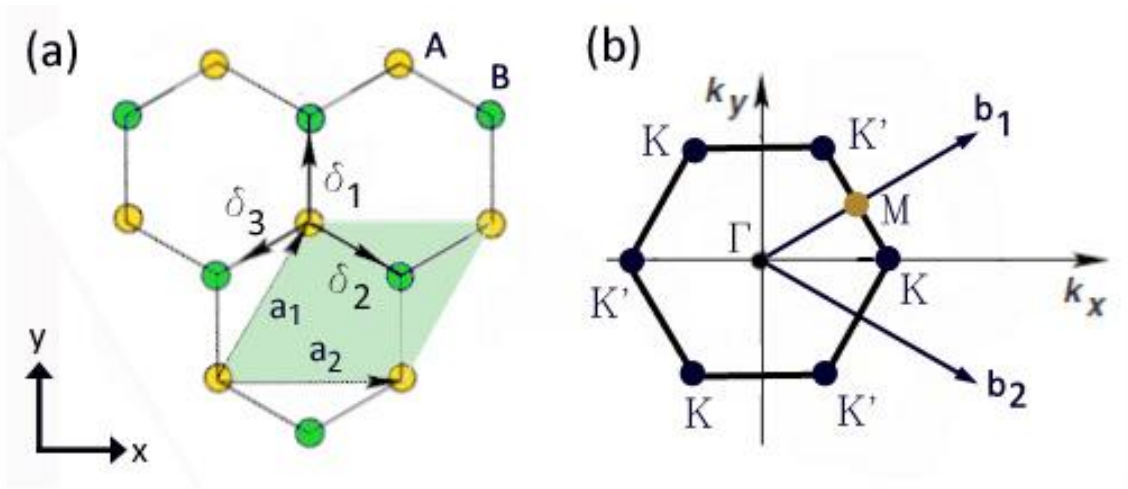


**Figure 2.4** (a) Graphene real space unit cell spanned by unit vectors  $\mathbf{a}_1$  and  $\mathbf{a}_2$  containing 2 atoms, one from each A and B sublattice. Nearest neighbor distance vectors are defined as  $\delta_i$  ( $i=1,2,3$ ) (b) Reciprocal graphene space; Brillion cell, primitive reciprocal-lattice vectors  $|\mathbf{b}_1|=|\mathbf{b}_2|=2\pi/a$  and zone boundaries and high symmetry points.

In order to explain the electronic structure of graphene we shall further examine its crystal structure. Figure 2.4a displays the real space lattice which can be described by a superposition of two hexagonal Bravais lattices, so called sub lattices denoted A and B. The

unit cell consists of 1 atom from each sub lattice spanned by the unit vectors  $\mathbf{a}_1$  and  $\mathbf{a}_2$  with  $|\mathbf{a}_1|=|\mathbf{a}_2|=2.46 \text{ \AA}$ . A sub lattice atom is adjacent to 3 opposite sub lattice atoms with nearest neighbor distance,  $|\delta_i(i=1,2,3)| = 1.42 \text{ \AA}$ .

A rather straightforward way to describe the low-energy electronic band structure of graphene is to use the tight-binding model by considering only the  $\pi$ -bonds to participate with the two  $p_z$ -orbitals, one from each sub lattice in the unit cell. The Schrödinger equation (SE) in momentum space is to be solved to get the band structure:

$$H\Psi = E(k)\Psi \quad (2.1)$$

Where the wave function  $\Psi$  is a linear combination of two Bloch function from the two carbon atoms in sublattice A and B. The tight-binding model is simplified by considering only nearest neighbor interactions which well describes the periodic potential in graphene. To determine the Hamiltonian the diagonal elements in can be taken from integration over each single carbon atom in sub lattice A and B and their compositional identically gives  $H_{AA}=H_{BB}$  value which can be set to zero as energy reference.<sup>32</sup>

The off-diagonal matrix elements essentially describe the coupling between A and B sublattice. With three nearest neighbor vectors for  $\delta_1, \delta_2, \delta_3$  expressed in Cartesian vector coordinates from figure 2.4a as:

$$\delta_1 = \left(0, \frac{a}{\sqrt{3}}\right), \quad \delta_2 = \left(\frac{a}{2}, -\frac{a}{2\sqrt{3}}\right), \quad \delta_3 = \left(-\frac{a}{2}, -\frac{a}{2\sqrt{3}}\right) \quad (2.2)$$

$H_{AB}$  can then be written as:

$$H_{AB} = tf(k) = t \left( e^{ik\delta_1} + e^{ik\delta_2} + e^{ik\delta_3} \right) = t \left( e^{ik_y a / \sqrt{3}} + 2e^{-ik_y a / 2\sqrt{3}} \cos\left(\frac{k_x a}{2}\right) \right) \quad (2.3)$$

The function  $f(k)$  in equation 2.3 above describes sublattice coupling and  $t$  is the so called transfer integral determined from the  $\pi$ -bonding orbitals and nearest neighbor distance. For graphene lattice a typical value for  $t$  is  $\sim 3$  eV.<sup>32</sup>

Further,  $H$  is Hermitian so that we have:  $H_{BA} = H_{AB}^*$  and as a result the complete Hamiltonian for the graphene sub-lattices can be written:

$$H = \begin{pmatrix} 0 & tf(k) \\ tf(k)^* & 0 \end{pmatrix} \quad (2.4)$$

Solving  $E(k)$  in the Schrödinger equation (Eq. 2.1) we get the  $\pi$ -orbital band structure<sup>33</sup>:

$$E(k_x, k_y) = \pm t \sqrt{1 + 4 \cos\left(\frac{\sqrt{3}k_y a}{2}\right) \cos\left(\frac{k_x a}{2}\right) + 4 \cos^2\left(\frac{k_x a}{2}\right)} \quad (2.5)$$

The function in equation 2.5 is plotted in 3D in figure 2.5a bellow where the interesting band structure features are illuminated. An ideal isolated graphene layer has the valence band and conductance band touching each other at a single point in  $k$ -space right at the  $K$  points of hexagon Brillouin zone displayed in figure 2.4b. Hence there is no gap in-between the valence and conductance band like in other common semiconductors making graphene to a zero-gap semiconductor.

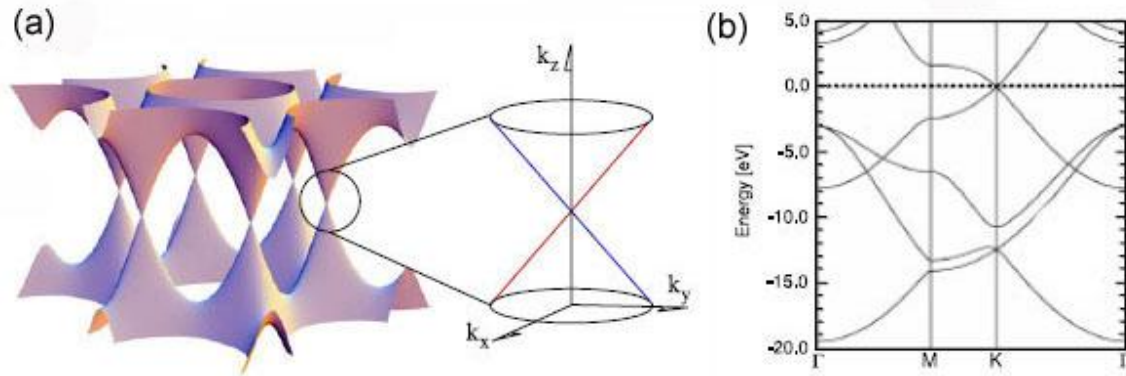


**Figure 2.5** (a) Fermi surface of graphene by the tight-binding model. The Fermi surface vanishes where the valence band and conduction band meet at the so called Dirac point. The blow up shows the linear dispersion (Dirac cones) for the  $\pi$ -bands close to the Dirac point. (b) Band structure of graphene from ab initio calculations along high symmetry lines in the 2D Brillouin zone. Here all bands are visible including contributions from  $\sigma$ -bonds. The linear energy dispersion from  $\pi$ -bonds can be seen near the Fermi level at the K point. Taken from reference [27].

Importantly, there are three so called valleys, each centered around K and K' points in the Brillouin zone with equivalent linear energy- momentum dispersion around  $E(K)=0$  ( $E(K')=0$ ). We can evaluate  $f(k)$  at these points with reciprocal coordinates determined from the primitive reciprocal lattice vectors  $\mathbf{b}_1$  and  $\mathbf{b}_2$  from figure 2.4b:

$$K = \left( \frac{4\pi}{3a}, 0 \right) \quad K' = \left( -\frac{4\pi}{3a}, 0 \right) \quad (2.6)$$

We get  $f(k)$  at these points:

$$f(K) = t \left( 1 + e^{i2\pi/3} + e^{-i2\pi/3} \right) = 0 \quad f(K') = t \left( 1 + e^{-i2\pi/3} + e^{i2\pi/3} \right) = 0 \quad (2.7)$$

Hence there is no interaction between the two sublattices exactly at K and K' points. They do however hold the same quantum states which results in the energy degeneracy shown in figure 2.5a. Because of the linearity of the band structure in the K and K' valleys we can Taylor expand Eq. 2.3 at K(K') to only include linear terms. We do this with help from a wave vector measured from K expressed as:

$$\kappa = k - K \quad (2.8)$$

Similar transformation can be done for K'. Off-diagonal Hamiltonian elements become<sup>34</sup>:

$$H_{AB} = tf(\kappa) = t \left( e^{i\kappa_y a / \sqrt{3}} + 2e^{-i\kappa_y a / 2\sqrt{3}} \cos\left(\frac{2\pi}{3} + \frac{\kappa_x a}{2}\right) \right) \approx \left(1 + \frac{i\kappa_y a}{2\sqrt{3}}\right) + 2 \left(1 - \frac{i\kappa_y a}{2\sqrt{3}}\right) \left(-\frac{1}{2} - \frac{\sqrt{3}\kappa_x a}{4}\right) \approx -\frac{\sqrt{3}a}{2}(\kappa_x - i\kappa_y) \quad (2.9)$$

This results in a new approximate Hamiltonian for electrons close to E(K) :

$$H = \frac{\sqrt{3}at}{2} \begin{pmatrix} 0 & (\kappa_x - i\kappa_y) \\ (\kappa_x + i\kappa_y) & 0 \end{pmatrix} = \hbar v_F (\boldsymbol{\kappa} \cdot \boldsymbol{\sigma}) \quad (2.10)$$

Where  $v_F$  is the Fermi velocity:

$$v_F = \frac{\sqrt{3}ta}{2\hbar} \quad (2.11)$$

This Hamiltonian in equation 2.10 is similar to the one used to describe relativistic particles with zero rest mass, i.e. Dirac particles.<sup>35</sup> Therefore graphene fermions at K and K' points are

often referred to as Dirac-like fermions and the points at  $E(K(K'))$  where the bands overlap are referred to the Dirac points. We get energy Eigenvalues and Eigenfunctions for the new Hamiltonian (eq. 2.10) as:

$$E(\kappa) = \hbar v_F |\kappa| \quad \Psi_{\pm} = \frac{e^{i\kappa \cdot \mathbf{r}}}{\sqrt{2}} \begin{pmatrix} 1 \\ \pm e^{i\varphi} \end{pmatrix} \quad (2.12)$$

Where  $\varphi$  is the polar angle  $\kappa$  vector in the graphene plane.<sup>34</sup> The linear energy-momentum dispersion is obvious from the eigenvalues and the Fermi velocity ( $v_F \approx c/300$  where  $c$  is the speed of light) is constant independent on the energy.

### 2.2.1 Graphene on SiC(0001)

The energy-momentum dispersion of graphene derived from theory is experimentally confirmed from samples of graphene grown on SiC(0001). Importantly, a substrate mediated interaction with the graphene exists that alters the electronic properties of the epitaxial graphene and will be discussed in the following.

What deserves special attention is the graphene-SiC interface which consists of a so called buffer-layer and has the epitaxial match  $(6\sqrt{3} \times 6\sqrt{3})R30^\circ$  with the SiC substrate. A bare buffer layer can be formed by heating the SiC crystal to temperatures around 1000 °C in UHV and further heating to around 1300 °C allows for controlled growth of graphene covered buffer layer. The  $(6\sqrt{3} \times 6\sqrt{3})R30^\circ$  buffer layer is commensurate with the  $13 \times 13$  graphene unit cell with ~0.14 % epitaxial strain:

$$6\sqrt{3} \cdot \mathbf{a}_{SiC} = 6\sqrt{3} \cdot 3.073\text{\AA} = 31.94\text{\AA}$$

$$13 \cdot \mathbf{a}_G = 13 \cdot 2.46\text{\AA} = 31.98\text{\AA}$$

The buffer layer and its existence has been long known but its atomic configuration and composition has been widely debated and difficult to interpret because of its complex appearance in STM and LEED measurements.<sup>36</sup> Angle resolved photo emission can however give an interesting comparison of buffer and graphene layer on SiC(0001). Interestingly, the ARPES recorded for buffer layer and graphene on SiC(0001) displayed in figure 2.6a-b show remarkable similarities in their corresponding  $\sigma$ -band structure with binding energy 5 to 25 eV. The similar shape and width of  $\sigma$ -bands suggests that the buffer layer is topologically very similar to graphene with same honey comb lattice structure and carbon-carbon bond lengths.<sup>37</sup> What is on the other hand strikingly different from the two surfaces is the  $\pi$ -bands which holds the delocalized  $\pi$ -states crucial for transport properties (fig. 2.6a-b). The buffer layer exhibit no graphene like  $\pi$ -bands around the Fermi level, in fact there are no states at all available making the  $6\sqrt{3}$  layer semiconducting compared to graphene which show the presence of the Dirac cone. ARPES in figure 2.6c-d clearly show this discrepancy around the K-point close to zero binding energy. Consequently, the buffer layer can be described as a “dead” graphene layer that has strong covalent bonds to the SiC through the carbon  $p_z$  orbitals such that complete disruption its  $\pi$ -band structure occur.

Photoemission spectra of C 1s core levels further illuminates the claim of significantly stronger substrate interaction of the buffer layer compared to the graphene sheet.<sup>37</sup>

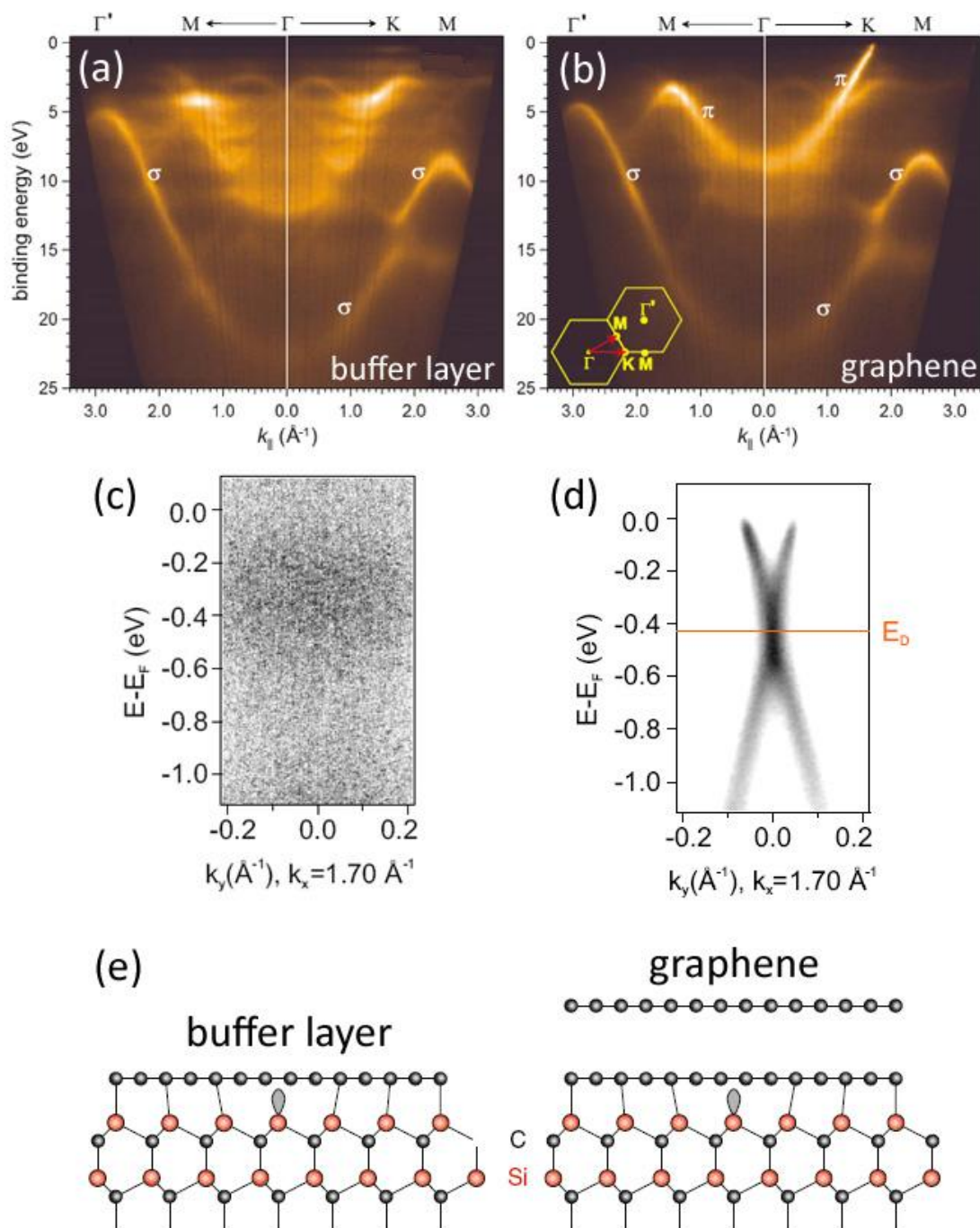


**Figure 2.6** (a) From ref. [37]: ARPES of buffer layer and (b) graphene grown on top of buffer layer. (c) From ref. [36]: Photoelectron intensity at the Brillouin zone K-point of buffer layer and (d) the epitaxial graphene. (e) Structural model of the SiC-buffer layer interface and SiC-graphene interface

Another important observation in figure 2.6a is that the  $\sigma$ -bands in the buffer layer are shifted up in energy compared to neutral graphite. As a result, Dirac point  $E_D$  of the graphene layer relative to  $E_F$  is also shifted but reduced to about 0.4-0.5 eV (fig. 2.6b and 2.6 d). This is explained by the fact that the graphene suffers from an intrinsic electron doping due to charge transfer from the substrate which corresponds to an excess charge of  $1.1 \cdot 10^{13} \text{ cm}^{-2}$ .<sup>38</sup> This charge transfer originates from Si-dangling bonds due to considerable lattice mismatch within the  $6\sqrt{3}$  unit cell at the SiC-buffer layer interface and has been confirmed by DFT calculations.<sup>39</sup> Estimations from photoemission studies suggest that about every third carbon atom form covalent C-Si that is coexisting with unsaturated Si-dangling bonds. A cartoon schematic of the approximate interface structure for buffer layer with covalent bond mixed with Si-dangling bands is shown in figure 2.6e along with the same structure with the additional on-top graphene layer.

### 2.2.2 Charge Transport in Graphene

The  $\pi$ -band electrons are located close to the Fermi level, delocalized in a crystal and thereby used to determine transport properties of graphene. The charge carrier mobility is a crucial parameter for the performance of a 2DEG device and is often cited when highlighting graphene electronic properties. Carrier mobility is a quantity relating the Fermi velocity of electrons or holes to applied electric field across a material and for graphene its room temperature intrinsic mobility extends over  $200.000 \text{ cm}^2/(\text{V}\cdot\text{s})$ .<sup>40</sup> For comparison the maximum values for Si is  $1400 \text{ cm}^2/(\text{V}\cdot\text{s})$  for electrons and around  $450 \text{ cm}^2/(\text{V}\cdot\text{s})$  for the hole mobility at 300K with carrier concentration  $10^{14} \text{ cm}^{-2}$ .<sup>41</sup> Importantly and sharp contrast

to Si and other conventional semiconductor materials, mobility in graphene is essentially independent on the carrier concentration (holes and electrons) up to  $10^{13} \text{ cm}^{-2}$  from either electrically or chemically doped samples.<sup>5</sup>

So what is the reason behind these superb transport properties of graphene? It can mainly be explained by two reasons. The first is a reduced lattice vibration scattering in graphene (phonons scattering) which is what drastically limits the mobility in Si as the temperature reaches room temperature.

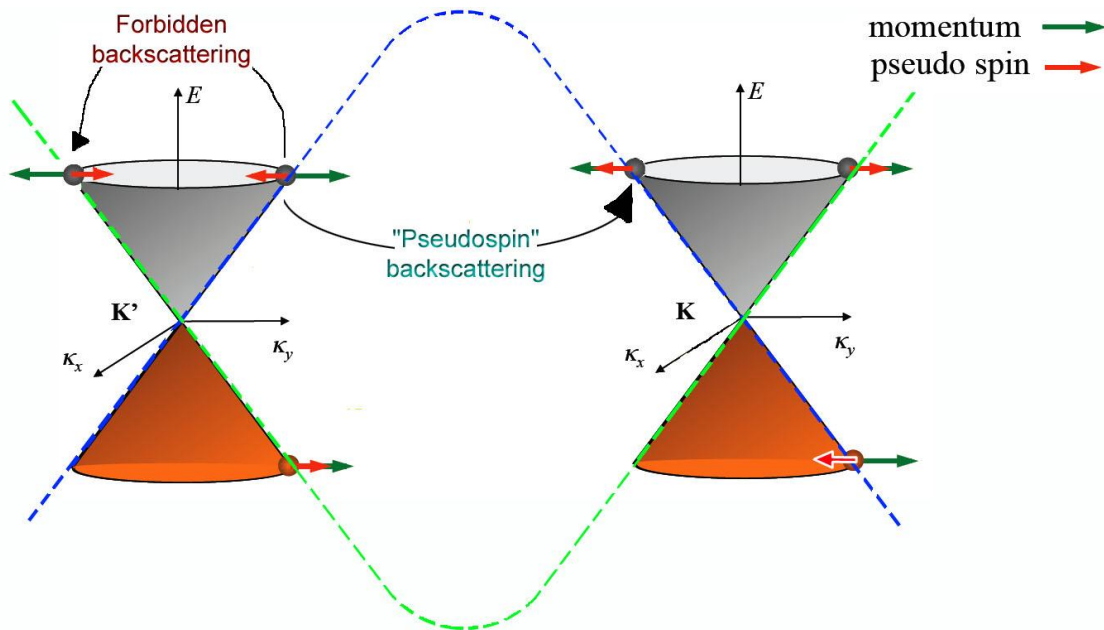


**Figure 2.7** Pseudospin for Dirac-like fermions in  $K'$  and  $K$  valleys in graphene. Small momentum backscattering becomes inefficient since it requires a flip of the pseudospin. A hopping in between valleys is possible without having to flip the pseudospin (pseudospin backscattering). Note that there are two bands crossing each other which gives a “chirality” of the valleys with the pseudospin.

Optical phonons have barely any temperature dependent impact on graphene mobility up to room temperature because of their energies above 150 meV are too high to couple with Fermi electrons in graphene.<sup>42</sup> The second explanation for the good mobility in graphene comes directly from the Dirac-like behavior of fermions in graphene. Dirac cone states carry so called pseudospin due to their chiral symmetry in K and K' valleys and is observed from eigenfunctions solved from the Dirac-like Hamiltonian (eq. 2.12). The chirality is important when description of mobility of massless charge carriers in graphene because conservation of both momentum and pseudospin needs to be considered during a scattering event. At complete backscattering ( $180^\circ$ ) is not theoretically allowed since it requires a flip of the pseudo spin in the massless cone (K or K' valley) (fig. 2.9).

A clear proof of graphene intrinsic ultra high mobilities were demonstrated for suspended graphene samples in a Hall bar set-up where mobilities of  $200.000 \text{ cm}^2/(\text{V}\cdot\text{s})$  were measured.<sup>43</sup> However as graphene is deposited on a substrate mobility numbers are drastically reduced. It appears almost inevitable to find substrates for graphene that does not impact on graphene transport properties and this is probably the biggest engineering challenge graphene based devices are facing. The first groundbreaking measurements were made on exfoliated graphene samples on  $\text{SiO}_2$  with measured room temperature mobilities up to  $15\,000 \text{ cm}^2/(\text{V}\cdot\text{s})$  for both holes and electrons.<sup>5</sup> Even though such values are still impressive compared to Si, extrinsic disorder (interactions with the  $\text{SiO}_2$  substrate) reduces mobilities by more than an order of magnitude. The reason for this has been widely debated but experiments have shown that interfacial charges at  $\text{SiO}_2$ -graphene interface are the main

source of scattering.<sup>44,45</sup> Short range disorder like charged impurities can, unlike long-range disorders (deformation or bending of graphene crystal), couple to the pseudospin portion of the wave function and allow for “pseudospin backscattering” (see fig. 2.9) that could be responsible for a great portion of scattering events in graphene.<sup>45,46</sup>

For epitaxial graphene on SiC(0001) the Hall-effect mobilities are even further reduced compared to exfoliated graphene on SiO<sub>2</sub>. Tedesco et al. measured room temperature values around 1500 cm<sup>2</sup>/ (V·s).<sup>47</sup> and partially this low value is due to the substrate mediated doping described in previous section.<sup>48</sup> Jobst et al. showed that if the intrinsic charge carrier concentration ( $1.1 \cdot 10^{13} \text{ cm}^{-2}$ ) is reduced by a chemical static gate to  $5.4 \cdot 10^{10} \text{ cm}^{-2}$ , epitaxial graphene have similar low temperature (25 K) mobilities as graphene on SiO<sub>2</sub>; up to 29000 cm<sup>2</sup>/ (V·s). Surprisingly they also observed a dramatic temperature dependence of the mobility with the value only 2500 cm<sup>2</sup>/ (V·s) at room temperature. Such a temperature dependence may be due to interface phonons or crystal imperfections but exact cause remains unclear.<sup>48</sup> Substrate induced impediment of graphene transport characteristics are in general difficult to interpret and need further consideration to take full advantage of graphene intrinsic mobility in high-performance electronic devices.

### 2.2.3 Disruption of Graphene Band Structure

The perhaps biggest future challenge of graphene is to be able to maintain its unique electronic properties during and after manufacturing of graphene devices. A clear example of this was presented in previous section where graphene substrate interactions significantly

impede transport properties in graphene. In this section, intrinsic disruption and manipulation of graphene band structure shall be discussed.

The linear E-k dispersion in graphene band structure is sensitive for factors that are breaking the two dimensional A and B sublattice symmetry of the graphene unit cell and the most common example for this is when multiple graphene layers are stacked on top of each other as in the famous carbon allotrope graphite. In graphite layers are stacked in AB configuration (Bernal stacking) resulting in a 3-dimensional unit cell containing four electrons from a total of three adjacent graphene planes (fig. 2.10a). The layer separation is relatively large ( $\sim 3.35$  Å) so that only weak electronic interactions occur between adjacent layers. However such interactions can easily be observed in STM at energies low enough compared to the graphite interlayer hopping energy, usually less than 100 meV.<sup>49</sup> Figure 2.10b shows an STM image of graphite imaged at -10 meV and clearly one sub-lattice show up more intense compared to the other resulting in a triangular symmetry in the image instead of the honeycomb structure. The two sublattices are inequivalent in the layer stacking sequence (equivalent in a single layer) since there are 4 carbon atoms positions in the graphite units cell, A, A', B, B' (fig. 2.10a). One of the top-layer sublattice atoms (B) are positioned over hollow sites in the layer below while the other top-layer sublattice (A) is positioned directly over atoms (A') in the layer below (fig. 2.10c). Consequently, the low-energy density of states for the A sublattice is reduced compared to the B sublattice which is picked up in the STM morphology.

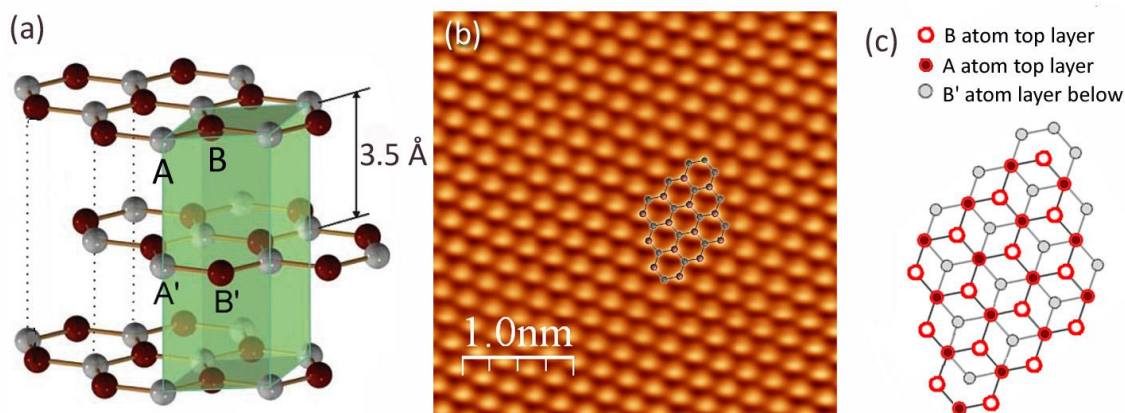


**Figure 2.8** (a) Schematic side-view of AB stacked graphene layers in graphite. Shaded area shows graphite unit cell with participating atoms from 3 layers and 2 different positions for each graphene sublattice: A, A', B, B'. Interlayer distance is 3.5 Å (b) STM of graphite imaged at Bias = -10 mV,  $I = 1$  nA where  $\pi$ -orbitals from one toplayer sublattice protrude more than the second sublattice due to AB-stacking discussed in the text. Superimposed is the full honeycomb cartoon structure from both sublattices. (c) Schematic top-view of the two top-most layers in an AB-stacked graphite structure.

As a result of this interlayer interaction, graphite has band overlap and deviations from the linear dispersion relation to a more parabolic shape such that the effective mass becomes a non-zero value.<sup>50</sup> The number of layers should thus be limited to avoid inter-plane interaction due to graphene AB-stacking which is highly relevant for epitaxial graphene grown on SiC(0001) because its layer stacking being identical to that of graphite.

Worth mentioning is that graphene grown on the C-face of SiC is stacked in a different configuration other than Bernal stacking which can lead to a reduction of inter-plane interactions. The stacking on this face is such that individual graphene layers behave as they were almost completely isolated and may explain why charge carrier mobilities are significantly higher for thick graphene films (5-100 layers) grown on the C-face compared to single layer graphene films on the Si-face of SiC(0001).<sup>51</sup>

Further, it is from a device technological aspect, motivated to intentionally manipulate graphene electronic structure by inducing a bandgap. The lack of a bandgap makes graphene impossible to operate in an insulating off-state switching mode in conventional field effect transistor geometry. The electronic band structure can however be manipulated again by breaking the equivalence of the A and B by stripping graphene into narrow nanoribbons. The edge geometry of a nanoribbon, which lacks the A and B sublattice symmetry, becomes significant for electronic structure of ribbons thinner than a few tens of nanometers. The edges then affect the density of states at the Fermi level enough to create a bandgap of finite energy between the conduction band and valence band. Energy gaps of up to 0.3 eV have been measured from a graphene ribbon width of 10 nm.<sup>52</sup>

Edge effects in a nanoribbon will also influence transport properties and there exist an inverse relationship between mobility and band gap so that for an extremely narrow graphene ribbon, large bandgap is induced but with poor mobility.<sup>53</sup> Low power applications are therefore best suited for graphene nanoribbons however to controllably pattern circuits of ribbons with sharp edges and narrow widths are experimentally very challenging to accomplish.

### **2.3 Proposed Future Graphene Devices**

As discussed in previous section, graphene might not be useful for “digital” charge based electronics because of its lack of bandgap. Instead other bandgap-independent electronic application may become the niche for graphene. Infact, IBM has already realized such device from graphene grown on SiC(0001) with graphene-FET’s and graphene-conductors in a

integrated circuit operating as a radio-frequency mixer at frequencies up to 10 GHz, about 50 times faster than the Si-based counterpart.<sup>54</sup> Another way of accommodate electric charge in a unconventional graphene device is to make use of electron optics with lensing and focusing possibilities from graphene heterojunctions.<sup>55</sup> Experiments led by Phillip Kim at Columbia University have experimentally demonstrated theoretical predictions that a graphene p-n junction structure can collimate ballistically transported carriers analogous to optical phenomena of a so called super lens (Veselago lens).<sup>55, 56</sup> This is possible due to the so called *Klein paradox* in graphene where Dirac-like fermions can tunnel through potential barriers in the absence of back scattering and conservation of momentum for the gapless chiral graphene band structure in the vicinity of the Dirac point (see. Figure 2.9). Charge carrier concentrations can be fine-tuned from either electric fields or chemical doping and if the densities on the n- and p-side of a graphene hetrojunction are equal, the normal-to-interface junction wave vector component (pseudo-spin and momentum) are preserved and can be transmitted through such symmetric potential barrier with unit probability (see. Figure 2.9). As a result, a ballistic n-p-n graphene junction can serve as an electron Veselago Lens or as a beamsplitter by electrostatically engineer the local geometry of the n- and p-doped regions as shown in figure 2.11.<sup>56</sup> In terms of the focus capabilities of such a device sub-wavelength resolution is less an issue by using electrons compared to photons in an optical lens.

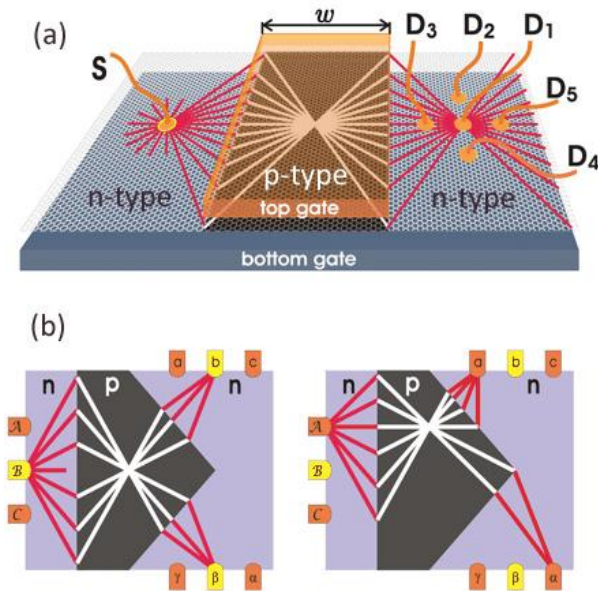


**Figure 2.9** (a) Electron Veselago lens based on graphene n-p-n junctions. By varying the charge carrier density in the p-type region by a top gate, an electron point source in one n-type region can be focused to desired position in the opposite n-type region. (b) Beam-splitter with prism-shaped p-region. From ref. [56].

The critical challenges are instead thermal energy distributions around the Fermi level for charge carriers and to achieve electrostatic barriers that are sharp enough, on the order of the electron wavelength.<sup>55</sup>

Other proposed devices that could benefit from graphene properties are touch screens, solar-cell electrodes and other flexible electronics. Graphene possess both high optical transparency and mechanical flexibility which makes it a material candidate for transparent electrodes superior to today's commercial transparent electrodes such as indium tin oxides.<sup>57</sup>

Finally to mention, exotic devices based on alternative state variables, other than electron charge based electronics, can stem from graphene's potential. Spin-valve devices for example are obvious research targets because of extremely weak spin-orbit coupling in

graphene that allows for efficient spin propagation over long distances.<sup>58</sup> A proposed spin-FET involves graphene to be used as an active channel where spin injection and detection are achieved from ferromagnetic source and drain while a ferromagnetic gate dielectric would manipulate spin to accommodate a spin filter effect.<sup>58</sup>

### 3: EXPERIMENTAL METHODOLOGY

The experimental methods utilized in this study were low energy electron diffraction (LEED), Auger electron spectroscopy (AES) and scanning tunneling microscopy (STM).

These were all part of an Omicron multi-purpose ultra high vacuum (UHV) system with two separate chambers, preparation chamber and analysis chamber.

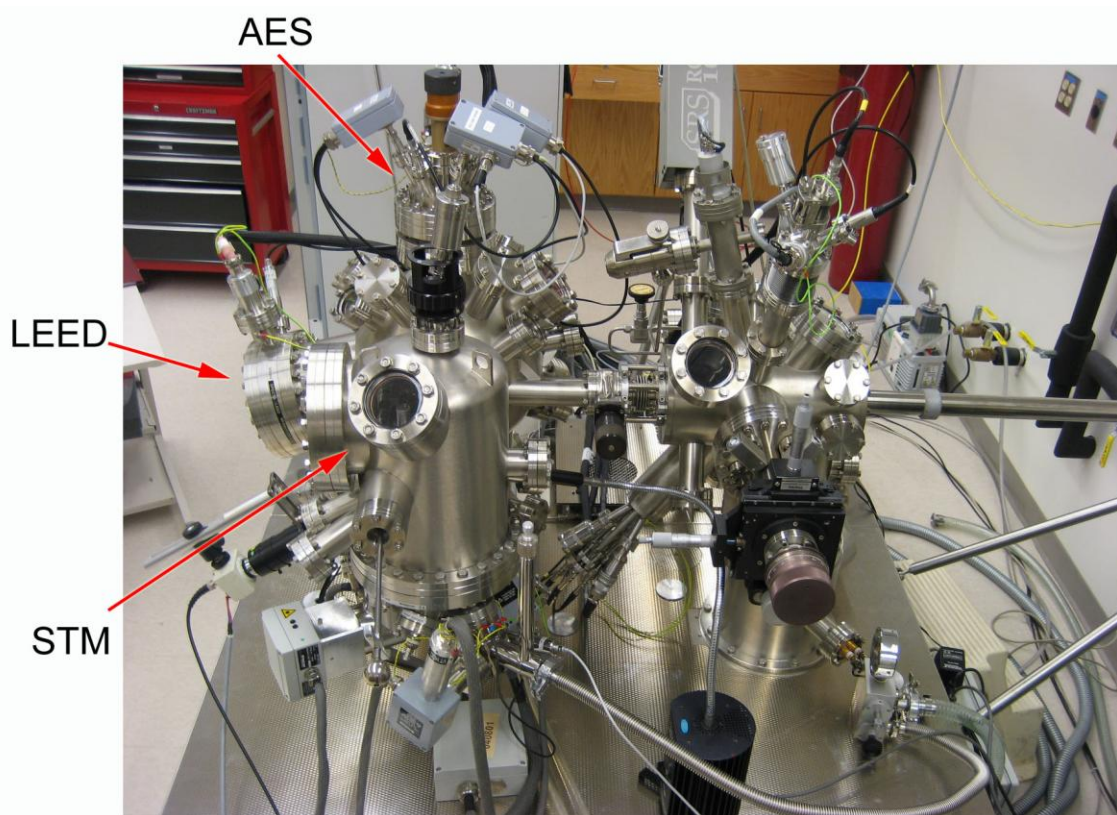


**Figure 3.1** UHV multi purpose system with two separated chambers. The methods used in this work were LEED, Auger and STM, all located in the analysis chamber.

The preparation chamber holds a base pressure of  $2 \times 10^{-9}$  mB and the analysis chamber has a base pressure of  $2 \times 10^{-11}$  mB. The system is capable of STM in variable temperatures (77 K-750 K), LEED, AES, ion beam sputtering, 4 cells for various electron beam metal deposition, residual gas analysis and fast entry lock for sample and tip exchange. The equipment used is shown in figure 3.1 and are described in the following.

### **3.1 Auger Electron Spectroscopy**

Auger electron spectroscopy (AES) is an analytical technique used to determine the quantitative chemical composition of surfaces, first described by Pierre Auger in 1925.<sup>59</sup> Electrons with moderate kinetic energy (1-10 keV) strike the specimen perpendicularly and ionize an inner electron level which is the start of an inelastic 3 step scattering process. A phase sensitive detection system makes it possible to distinguish and measure the resulting surface ejected electrons, so called Auger electrons which can be seen as finger prints of each element present on the sample surface.<sup>60</sup>

#### **3.1.1 The Auger Process**

Auger electrons normally have a kinetic energy of 30-1000 eV. The short mean free path of electrons in this energy range makes AES to a surface sensitive technique. Image 3.2 illustrates the three step process involved in Auger electron spectroscopy. High energy excitation particles (electrons, photons or even He atoms) are allowed to interact with the sample surface and ionize a core state electron. After a relaxation this creates a photoelectron and an atom with a core hole. A deexcitation proceeds to fill this core hole with a less

strongly bound electron and the excess energy from this decay ejects another less strongly bound electron.

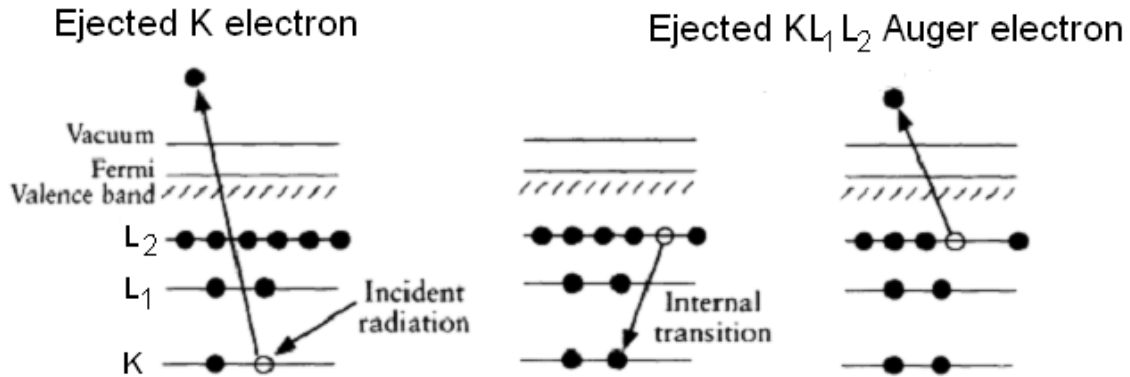


**Figure 3.2** Schematic illustration of a typical Auger transition process. The participating electron shells are a core shell (K) and shells close to the Fermi level,  $L_1$  and  $L_2$  in this case. Image taken from [61].

This ejected electron is the measured Auger electron. Hence the atom is left in a two electron ionized state after a complete Auger process. Typical notations for the type of Auger transition can be for example  $K_L L_1 L_2$  or  $L_3 V V$  where K corresponds to  $1s$ ,  $L_1 \rightarrow 2s$ ,  $L_2 \rightarrow 2p_{1/2}$ ,  $L_3 \rightarrow 2p_{3/2}$  etc. and V stands for a valence band electron. The kinetic energy of an Auger electron leaving an atomic orbital can be written as<sup>62</sup>:

$$E_{\text{kin}} = E_c - E_i - E_j - U_{\text{cor}} \quad (3.1)$$

Where  $E_c$  is the core electron energy,  $E_i$ ,  $E_j$  are the energies of the respective higher lying states and  $U_{\text{cor}}$  relates to the correlation energy between the two valence holes in the final state of the Auger process. An Auger spectrum is composed of all possible combinations of

$E_i, E_j$  in the valence band makes the Auger line shape reflecting a self-convolution of the distribution of the density of states (DOS). An example of this is the well studied KVV line shape of graphite where the DOS can be divided up in partial density of states components. Houston et al. showed that if each component is multiplied with an own specific hole correlation  $\sigma^*\sigma$ ,  $\sigma^*\pi$  and  $\pi^*\pi$  an experimental Auger line shape can be theoretically explained in terms of the chemical bonding of the carbon.<sup>63</sup>

In order to detect the Auger electrons they have to make it the way up to the surface and overcome the work function of the sample. Due to the short inelastic mean free path, scattering events during this process will create a wide range of secondary electrons.

Therefore the Auger signal will be hidden in other secondary electron noise and contains Auger information only from a few top most atomic surface layers. The Auger electrons can also give up energy to surface Plasmon's which might show up as a peak close to the Auger related peaks in the energy spectrum.<sup>63</sup>

If the sample to be investigated is insulating the two final state holes are immobile and can not easily be transported away from the surface. This results in sample charging which will strongly disturb the Auger signal.

Another consequence from the two electron ionization process is that no Auger peaks will appear from either hydrogen or helium which only has 1 and 2 electrons respectively.

Virtually any other element can be detected however the probability of radiative relaxation of the core hole (i.e. X-ray fluorescence) increases with increasing atomic number.

### 3.1.2 Detection of Auger Electron Energies

To select and collect electrons with a particular energy an electron energy analyzer is required. There exist electrostatic analyzers using dispersive or retarding field where the dispersive so called cylindrical mirror analyzer (CMA)<sup>64</sup> is the most common and used in this work. Its basic construction consists of an outer cylinder, an inner cylinder with entrance and exit slits and a detector. An electric field applied between the two coaxial cylinders (inner cylinder to ground) will deflect incoming electrons differently depending on their kinetic energy and only electrons with certain energy will make it through the exit slit and on to the detector. Scanning the potential over the coaxial cylinder will sweep electrons with different energies across the detector to generate a spectrum of  $dN(E)/dE$  where  $N(E)$  is the electron energy distribution. The fractional resolution,  $\Delta E/E$ , in a CMA is independent of energy and therefore the transmission function is proportional to the energy. Hence the measured spectrum is proportional to  $E \cdot N(E)$ . On the other hand, with increasing energy the detection efficiency  $D(E)$  of the electron multiplier is drastically decreased.<sup>65</sup> These two effects compensate for each other and therefore a whole spectrum can be recorded with the same gain. The output current  $I(E)$  is thus proportional to:

$$I(E) \propto E \cdot N(E) \cdot D(E) \quad (3.2)$$

The signal from each electron hitting the detector is greatly amplified by an electron channel multiplier, so called channeltron. Often the current of electrons reaching the detector is too large so they arrive too closely spaced to be distinguishable as separate events. This is called

the analogue mode and the current signal has to be modulated in order to separate the Auger electrons buried in a strong secondary electron background. This is accomplished by use of a lock-in amplifier which superimposes a modulation voltage on to the outer mirror voltage  $U_o$ :

$$\Delta U = A \sin(\omega t + \Phi_{\text{ext}}) \quad (3.3)$$

$\omega$  is the frequency,  $\Phi_{\text{ext}}$  is phase shift and  $A$  is the modulation amplitude.

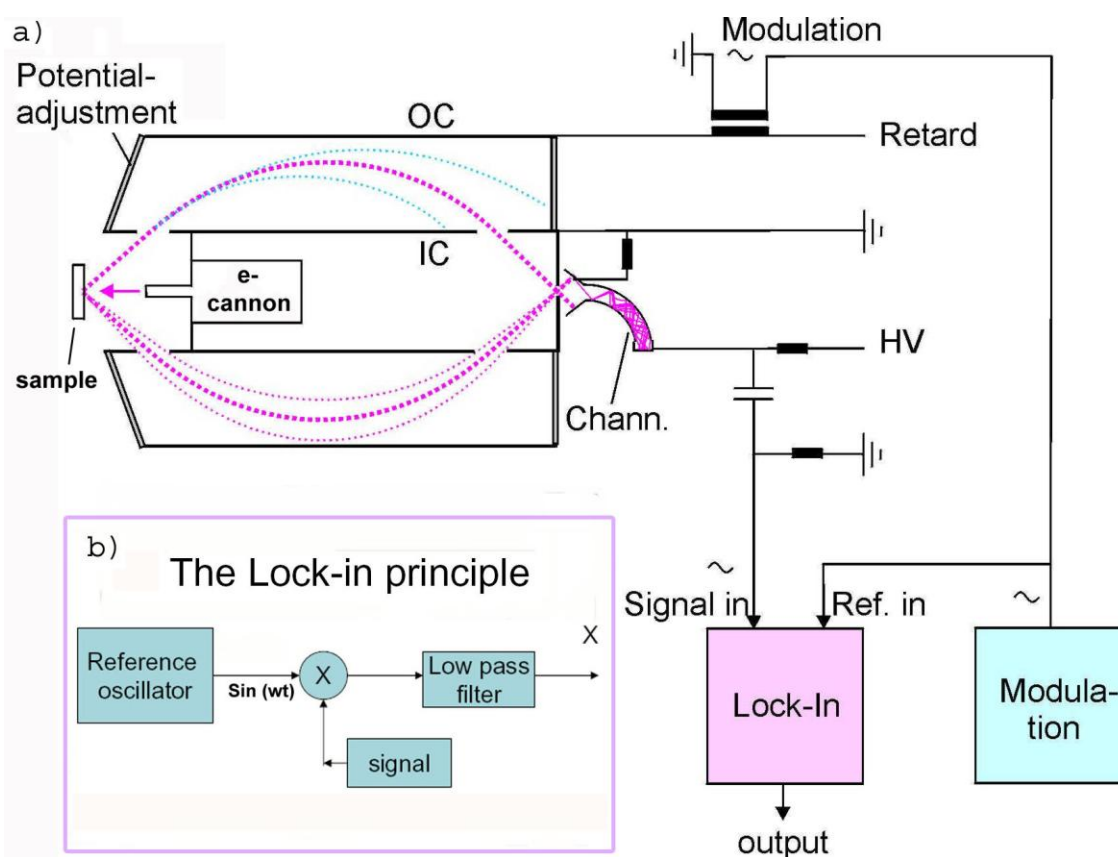


**Figure 3.3** Signal and data processing for AES analysis. (a) CMP connected to a channeltron. (b) Basic principles of a lock-in amplifier (single phase): A known reference signal is multiplied by the in-signal. An integrator acts as a low-pass filter which gives the output proportional to one half the amplitude of the signal derivative. Image (a) taken and modified from [66].

The total current out from the channeltron is then  $I(U_o + \Delta U)$  and can be written in terms of Taylor expansion

$$I(U_o + \Delta U) = I(U_o) + I'(U_o)\Delta U = I(U_o) + I'(U_o)A \sin(\omega t) \quad (3.4)$$

Second and higher order derivatives are here neglected since the modulation amplitude is assumed to be very small compared to  $U_o$ . A simplification of how a lock-in amplifier works is showed in figure 3.3b. A reference frequency is multiplied to the signal  $I(U + \Delta U)$  with a sinusoidal reference to enter a low pass filter X. An integrator acts as the low pass filter where the signal is integrated over a time much longer than the period of  $\omega$ , typically 10-300 ms. This gives a non-zero value of the signal out only if the reference signal and signal in are in phase. The in-signal for an ideal amplifier ( $\Phi_{\text{ext}} = 0$ ) gives:

$$\begin{aligned} & \sin(\omega t)_{\text{ref}} \cdot [I(U_o) + I'(U_o)A \sin(\omega t)] \\ & \sin(\omega t) \cdot I(U_o) + I'(U_o)A \frac{1}{2}(1 - \cos(\omega t)) \Rightarrow \text{lowpass} \Rightarrow I'(U_o)A \frac{1}{2} \end{aligned} \quad (3.5)$$

Hence the lock-in can measure the amplitude of  $A \cdot I'(U_o)$  which is proportional to  $dn(E)/dE$  according to equation (3.2). For this first derivative signal the signal to noise ratio is drastically reduced and clear Auger peaks can be distinguished on the spectra, thanks to the lock-in technique.

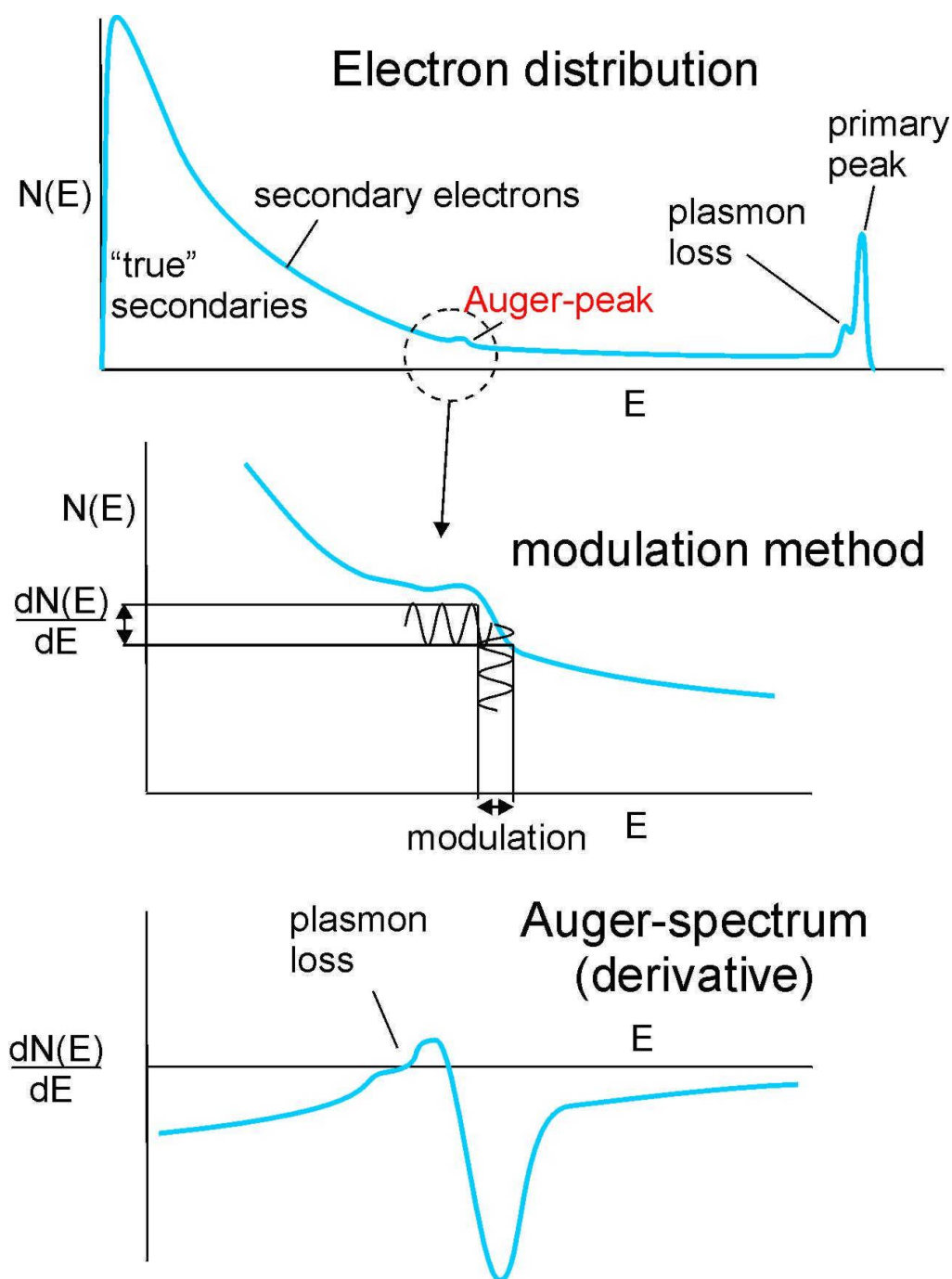


**Figure 3.4** Modulation used to increase signal to noise ratio in AES analysis. (a) Typical spectra from the electron distribution,  $N(E)$ . (b) Signal is modulated by a high frequency, low amplitude signal allowing to measure  $dN(E)/dE$ . (c) The first derivative of modulation gives a clear AES spectrum. Image taken from ref [66].

### 3.1.3 Graphene Thickness Measurement Using Auger Spectroscopy

Auger spectroscopy is utilized in this work to monitor the surface Si sublimation when annealing SiC samples. This is done by comparing Auger peaks from the carbon content and the Silicon content on the surface. Such comparison also gives a direct estimation of the graphene thickness grown on the surface. A model for the graphene thickness was developed by Li<sup>66</sup> where the Auger attenuation for Si (KLL) and C(KLL) was used for different types of layer structures underneath the graphene.

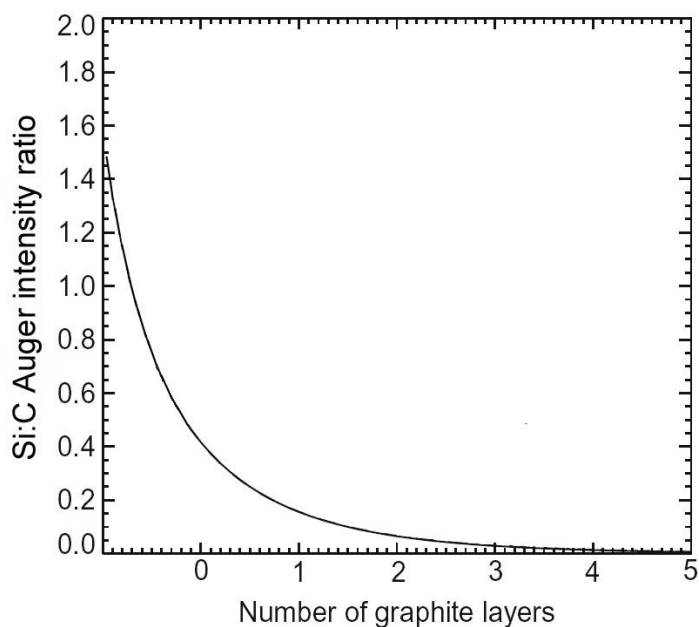


**Figure 3.5** Estimated graphene layers versus Auger peak-to-peak ration of the Si(LVV)/C(KLL). The image is taken from ref. [66] but corrected for the intermediate carbon-rich buffer layer that is always present underneath the epitaxial graphene grown on SiC. The zeroth layer simply corresponds to the buffer layer.

One part of Li's model involves a graphene lying right on top of the SiC crystal. This is not the real case because there will be an intermediate carbon buffer layer in between with the same structure and number of carbon atoms per surface area as graphene (See section 2.2.1). This will make Li's model to overestimate the graphene thickness with approximately 1 layer. This overestimation is corrected in the diagram below.

### **3.2 Low Energy Electron Diffraction**

Low Energy Electron diffraction (LEED) is based on the fact that electrons are diffracted in the same way as light is diffracted by a grating.<sup>67</sup> A LEED experiment is performed by bombarding an ordered surface with electrons and then analyze the elastically back-scattered electrons as a function of direction and intensity. The scattered electrons produce a diffraction pattern which is a scaled image of the surface atomic symmetry in reciprocal space. The incoming electrons hitting the sample surface have a relatively low kinetic energy in the range of 30-300 eV. In this energy range the electron wavelength is comparable to the lattice spacing of typical surfaces and has the lowest possible escape depth, see fig. 3.6.<sup>68</sup> This makes LEED to powerful surface geometrical analysis tool being able to probe only about the 3 top most atomic layers on a crystal surface.

Combining LEED with real space scanning tunneling microscopy usually solves surface atom arrangements in a straightforward way.<sup>69</sup>

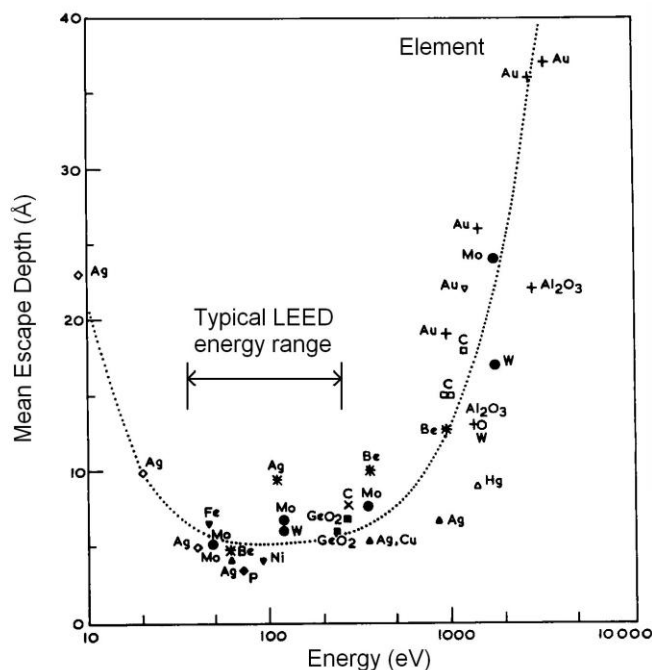


**Figure 3.6** Variations in mean escape depth of various materials as a function of electron energy. Taken from ref. [68].

### 3.2.1 Four-Grid LEED System

A standard LEED equipment design has been used in this work with the primary parts consisting of four retarding potential grids, electron gun and a phosphor screen as the collector. A filament made of thoriated tungsten (WTh) was used as the electron source in the electron gun. The filament is resistively heated to emit electrons which are accelerated by positive potential anodes relative to the gun anode. The accelerated electrons are launched on the sample surface with a  $\sim 1$  mm diameter beam. The sample sits in the center of a four-grid metal and a phosphor screen constructed as concentric hemispheres. The first grid is connected to earth to provide a field free space in between the sample and the first grid. The

second and third grid are called suppressors and have a negative potential applied acting as a high energy pass filter to only allow elastically scattered electrons through and suppress inelastic scattered electrons. Grid four is grounded to avoid a high capacity building up in between grid and the collector. This is a possibility since the collector is at a high voltage potential of 6kV in order to render the diffraction beams visible on the phosphor screen.

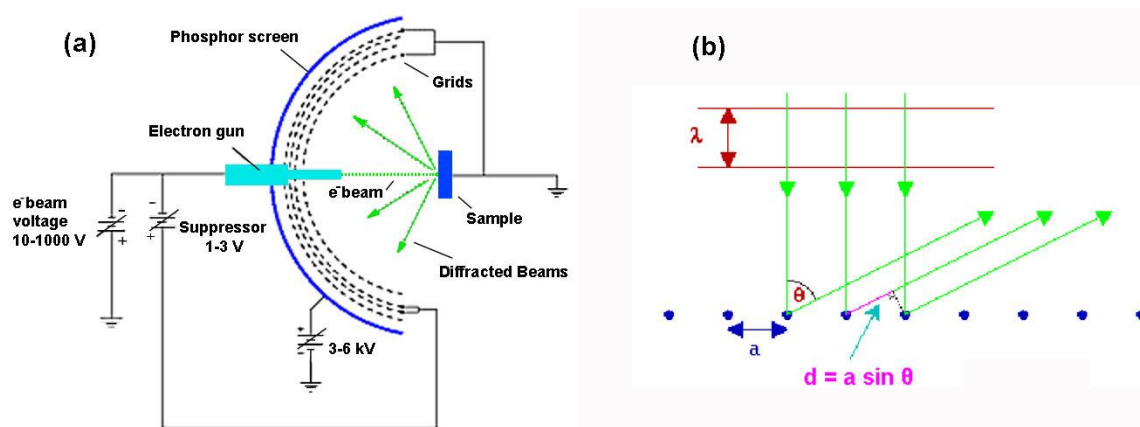


**Figure 3.7** (a) Diagram of a four-grid reverse view LEED system optics. (b) Atomic scale image in 1D of the electron beam impinging and scattered off an ordered sample surface with lattice spacing  $a$ . Laue Conditions for the normal incidence electrons are fulfilled if the phase shift  $d = a \cdot \sin \theta$  equals an integer number of the electron wave length,  $\lambda$ .

### 3.2.2 Kinematic Theory of LEED

The definition of kinematic scattering states that an electron incident on a surface is diffracted elastically only once at the surface. This theory can be considered fairly realistic due to the short penetration depth for the low energy electrons and can explain most of the basic physics involved in electron diffraction.

A free incident electron on a surface atomic unit cell can be described by a plane wave. This plane wave will be scattered in all directions but will interact with other waves scattered from neighboring surface unit cells. The waves will interfere if they are all in phase at a certain position in space meaning that their path differs by an integer number of wavelengths  $\lambda$  (assuming same phase shift from the scattering for all incoming electrons). The length of  $\lambda$  integers can be visualized in one dimension based on the lattice distance,  $a$ , and scattered angles, called Laue condition:

$$a(\sin \theta_n - \sin \theta_0) = n\lambda, \quad n = 1, 2, 3, \dots \quad (3.6)$$

Where  $\theta_0$  is incident angle for the electrons and  $\theta_n$  is the scattered angle with respect to the surface normal. For electrons at normal incidence, (3.6) reduces to  $a \sin \theta_n = n\lambda$  which is the case for LEED experiments (see fig 3.7b). 2-dimensionall generalizing (3.6) in unit vectors  $\mathbf{s}$  and  $\mathbf{s}_0$  the same expression will appear as:

$$\mathbf{a}_1 \cdot (\mathbf{s} - \mathbf{s}_0) = h\lambda, \quad h = 1, 2, 3, \dots \quad (3.7)$$

$$\mathbf{a}_2 \cdot (\mathbf{s} - \mathbf{s}_0) = k\lambda, \quad k = 1, 2, 3, \dots \quad (3.8)$$

Where  $\mathbf{a}_1$  and  $\mathbf{a}_2$  are the real space lattice vectors. It is here obvious that the diffracted beams are determined by  $\Delta \mathbf{s} = \mathbf{s} - \mathbf{s}_0$  which are given by integral multiples of the basic units  $\lambda/|\mathbf{a}_1|$  or  $\lambda/|\mathbf{a}_2|$ . It is then appropriate to define a reciprocal lattice vector such that:  $\mathbf{a}_1^* = 1/\mathbf{a}_1$  and  $\mathbf{a}_2^* = 1/\mathbf{a}_2$ . In two dimensions the real space lattice is described by the two lattice vectors  $\mathbf{a}_1$  and  $\mathbf{a}_2$

and the correspondent reciprocal lattice can then be constructed from basis vectors  $\mathbf{a}_1^*$  and  $\mathbf{a}_2^*$ . The Laue condition in (3.7) and (3.8) can thus be solved whenever

$$\Delta\mathbf{s} = \lambda(h\mathbf{a}_1^* + k\mathbf{a}_2^*) = \lambda\mathbf{g}_{hk} \quad (3.9)$$

The 2D reciprocal lattice vectors makes up rods like (01), (02) etc. and are constructed such that they are parallel to each other and perpendicular to the real space 2D plane.<sup>70</sup>

A simple geometric visualization of the kinematic diffraction process can be made with help from the so called Ewalds construction.<sup>71</sup>

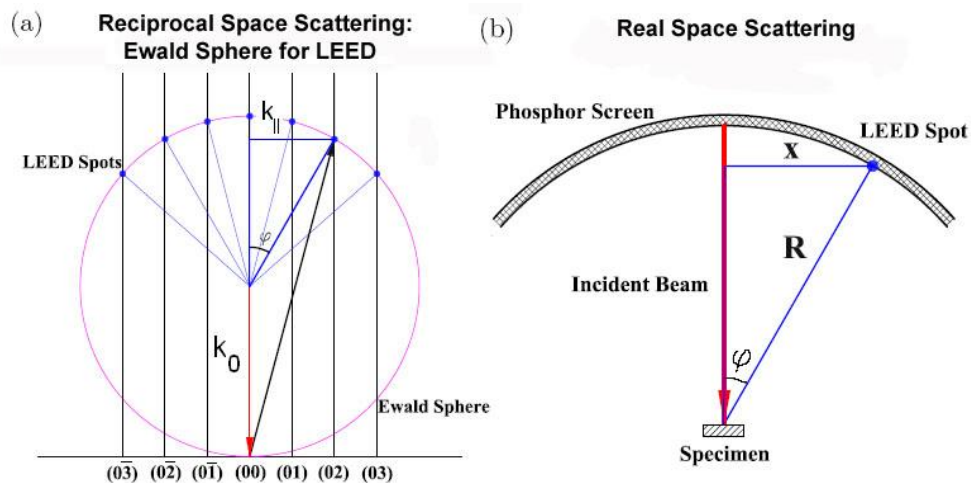


**Figure 3.8** (a) The Ewalds-sphere construction in LEED viewed parallel to the surface. (b) Real space setup of LEED. The blue triangles are analogous in the two images and determine a direct mapping of the reciprocal lattice spot projected on a phosphor screen.

The incident beam may be represented in reciprocal space by a vector  $\mathbf{k}_0$  of length  $1/\lambda$ . Now since we are dealing with elastically scattered electrons in LEED, the scattered beams will have the same length. A sphere with radius of the incident and scattered beam length can be

drawn which is called the Ewalds sphere. If the Ewalds sphere is superimposed on the reciprocal lattice rods, constructive diffraction conditions are fulfilled only when a reciprocal lattice point falls on the Ewalds sphere (see fig. 3.8a). The scattering vector component parallel to the surface must then equal a vector of the 2D surface reciprocal lattice. The real space analogous is shown in figure 3.8b as of the basic experimental setup of a LEED experiment. Due to these requirements, only a well defined periodic surface will exhibit a sharp LEED pattern.

### 3.2.3 Interpreting LEED Pattern

From the diffraction pattern visualized by the phosphor screen, the real space lattice distance can be calculated from the Laue conditions in equation (3.6). Using normal incidence electron,  $\theta_0$  will equal 0 and  $\sin \theta_n$  can be replaced by the ratio of  $x/R$  as denoted in figure 3.8b. This gives the length of the nearest neighbor distance in between the surface atoms:

$$a = \frac{R}{x} \lambda = \frac{R}{x} \frac{h}{m_0 v} = \frac{h}{\sqrt{2m_0 eV}} = \frac{R}{x} \sqrt{\frac{150.1}{E(eV)}} \quad (3.10)$$

The energy of the incident electrons is obviously changing the spacing in between the diffraction spots according to (3.10) and figure 3.8b. Large energy will give small distances and small energy will give large distances in between the spots. Hence, the electron energy, has the function analogues to a zoom effect of the diffraction pattern by lowering the kinetic electron energy.

If the lattice spacing is to be determined from a close-packed hexagonal atomic arrangement like SiC(0001), the nearest neighbor distance is shorter than the actual primitive unit cell lattice by a factor of  $\sin 60^\circ = \sqrt{3}/2$ . This factor needs therefore to be multiplied to the right hand side of equation (3.10) for a hexagonal lattice used in this work. The primitive unit cell is the smallest cell corresponding to a single lattice point of a structure with translational symmetry and since we are here dealing surfaces this symmetry is in 2D. The substrate primitive unit cell parameters are often well known of the sample prior to a LEED experiment. More of interest is the so called superlattices at surfaces. This is an additional periodicity which can be due to an intrinsic reconstruction of the clean surface or the presence of an ordered adsorbed molecular overlayer. To the different reconstructions of SiC the Wood notation<sup>72</sup> will be used to label the scheme for those superlattices. If the substrate lattice vectors are defined by  $a_1$  and  $a_2$  and the lattice vectors of the superlattice by  $b_1$  and  $b_2$  then the whole system is described with Wood notation by<sup>72</sup>:

$$\left( \begin{array}{cc} b_1 & b_2 \\ a_1 & a_2 \end{array} \right) R\alpha \quad (3.11)$$

Where  $R\alpha$  includes the possibility of rotation of the overlayer unit cell by  $\alpha$  degrees with respect to the unit cell of the substrate. For example, a common superlattice often apparent on bare SiC(0001) surfaces is the  $(\sqrt{3}\times\sqrt{3})R30^\circ$  reconstruction described according to Wood notation. This superlattice thus have unit cell vectors that are  $\sqrt{3}$  times the unit vector of the SiC substrate meanwhile being rotated 30 degrees with respect to the SiC bulk structure.

### **3.3 Scanning Tunneling Microscopy - Techniques and Principles**

Scanning tunneling microscopy is today probably the most powerful single experimental method in the field of surface science. Developed and first demonstrated in 1982 by pioneering work of Binnig et al.<sup>73</sup> STM has since then stimulated a revolution in high-resolution surface analysis and has already passed its expectations in imaging capabilities. It has been proven to be a very powerful and unique tool to determine local structural and electronic properties of surfaces down to sub-Ångstrom resolution. The strength in resolution makes it possible to distinguish single atomic defects, determine positions of empty or filled electron surface orbitals, probe local density of states etc. The list can be made long of the unique capabilities of STM that are inaccessible by other diffraction and spectroscopy techniques.

#### **3.3.1 Basic Setup and Principles**

The basic setup for an STM experiment involves a sharp metal tip brought in to close proximity to the surface to be investigated. At a typical distance of a few Ångstroms a quantum mechanical tunneling current can be established of approximately 1 nA by applying a small voltage bias in between the tip and the surface. The tunneling current is allowed if there exist an overlap of the tails of the wave functions within the vacuum gap of the tip and sample electrons and to create an image with help from this tunneling current, the tip is raster scanned over the surface at a constant current which is interpreted as a space image.

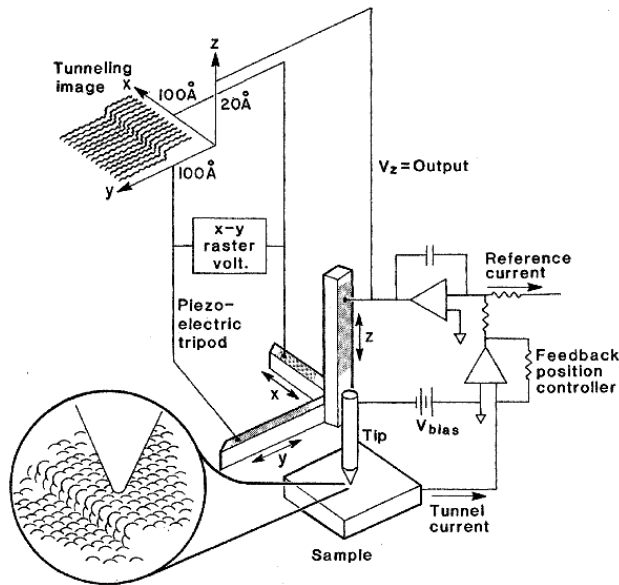


**Figure 3.9** Simplified schematic view of an STM. The tip is scanned in the two lateral dimensions while a feedback circuit is constantly adjusting the tip height to keep the current constant. The voltage supplied to the piezo drivers produces the path of the tip which gives an image of the shape of the surface. Taken from [75].

The electron wave functions decay exponentially in the vacuum gap which makes the tunneling current is extremely sensitive to the height of the tip above the surface. This can be illustrated by a simple but useful approximation of a STM tunneling process obtained from the typical finite rectangular barrier problem of quantum mechanics. The potential barrier can be seen as the vacuum region between two metal electrodes, in this case the tip and the sample surface. Within the barrier the solutions of the Schrödinger equation have the form<sup>74</sup>:

$$\Psi = e^{\pm\kappa z}, \quad \text{with } \kappa = \sqrt{\frac{2m(V_B - E_n)}{\hbar}} \quad (3.12)$$

Where  $m$  is the resting mass of the electron,  $E_n$  is the energy of the state of the electron and  $V_B$  is the potential barrier height. This potential is not constant as the rectangular barrier problem implies, however its average value is here adequate to use for simplicity.  $V_B$  can be considered to be the vacuum level of the surface and therefore  $V_B - E_n$  implies the work function. The tunneling current is proportional to the transmission coefficient  $T$ , which decays exponentially with the barrier width,  $d$ , as:

$$T = e^{-2\kappa d} \propto I \quad (3.13)$$

A work function of around 4-5 eV (as of most relevant STM samples) typically gives  $2\kappa \sim 2 \text{ \AA}^{-1}$ . Thus the tunnel current drops by approximately an order of magnitude for every 1  $\text{\AA}$  separations in between the electrodes. To keep the current stable for such small variations requires precise control of the tip and sample. This is achieved by using piezoelectric drivers for the movement of the tip. By using such drivers in each x-, y- and z-direction the tip can be moved in extremely small steps. The tip is scanned in two lateral dimensions while a feedback circuit constantly adjusts the tip to keep the tunneling current constant. Meanwhile the whole apparatus is vibration isolated from the surrounding by springs and special designed tables. It becomes very challenging to interpret high resolution STM images containing just a few surface atoms. At these small scales it is difficult to define the meaning of the word “topography” since the image is a convolution of the physical and electronic structure of the surface. To interpret unknown surface structures a profound theoretical understanding is therefore needed to understand and analyze STM images.

### 3.3.2 The Physics of Tunneling

Imagine two electrodes (tip and sample) that are allowed to be brought into close vicinity of each other. If the gap in between them is small enough, electrical equilibrium will be established, i.e. their Fermi levels will line up with each other (Fig. 3.10a). This equilibrium can be disturbed by applying a voltage  $V$  across the gap so that the Fermi levels will differ by  $eV$ . Tunneling can now occur for the electrons near the Fermi level from an occupied state to an unoccupied state in the tunneling window  $eV$  (see fig 3.10b).

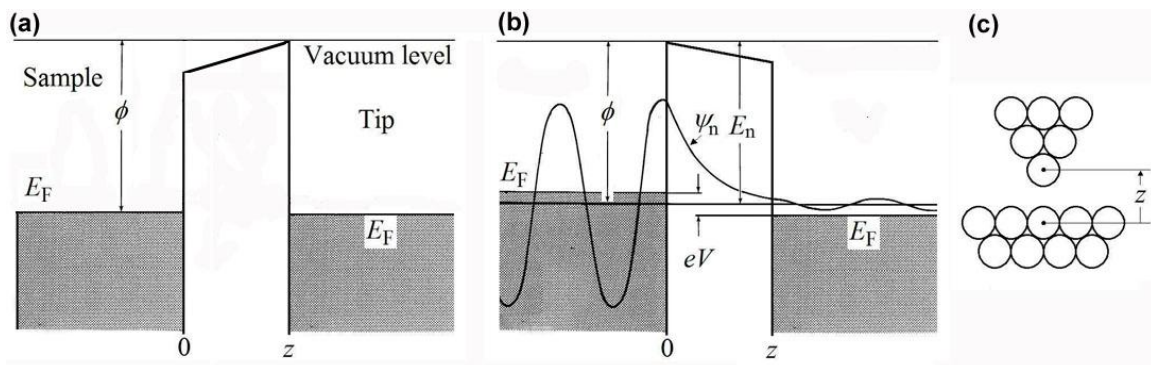


**Figure 3.10** Schematics of potential barrier between electrodes for vacuum tunneling. (a) Two electrodes with slightly different work functions are brought to close proximity so that electrical equilibrium, i.e. a common Fermi level ( $E_F$ ), is established. (b) A bias voltage  $eV$  is applied which will cause the Fermi levels to differ by  $eV$  and enable current. The sample states between energy level  $E_F - eV$  and  $E_F$  can tunnel to the tip and generate a tunneling current. The schematic illustrates tunneling of one of such state with the wave function  $\Psi_n$  with energy  $E_n$ . (c) The tip-sample distance is defined between the topmost tip atom with respect to the nucleus of the nearest atom of the sample. Image taken and modified from [76].

By applying a positive voltage over the tip and keep the sample grounded, electrons will tunnel from the sample into the tip (imaging occupied states) as suppose to applying a negative voltage which will result in electrons tunneling from the tip into the sample

(imaging unoccupied states). A powerful and convenient approximation of the tunneling current was developed by Tersoff and Hamann.<sup>77</sup> It is based on the first order perturbation theory using the wave functions for each free electrode and the electron transfer in between them as the perturbation. For a typical tip-sample separation of about 9 Å this is a reasonable approximation because of a fairly weak tip to sample coupling. The total current in first order perturbation theory becomes:

$$I = \frac{e}{\hbar} \sum_{\mu,\nu} |M_{\mu\nu}|^2 \cdot [f(E_{\mu}) - f(E_{\nu} + eV)] \delta(E_{\mu} + E_{\nu}) \quad (3.14)$$

The sum is over all possible states where  $M_{\mu\nu}$  is the matrix element between the tip states  $\Psi_{\mu}$  and the sample states  $\Psi_{\nu}$  and  $f(E)$  is the Fermi function:  $f(E) = (1 + \exp[(E - E_F)/k_B T])^{-1}$ . The applied bias is denoted  $eV$  and the delta function manifests a consideration of only elastic tunneling.<sup>78</sup> If the assumption is made that the temperature equals zero, the Fermi function become a step function and then (3.14) can be simplified to:

$$I = \frac{2\pi}{\hbar} e^2 V \sum_{\mu,\nu} |M_{\mu\nu}|^2 \delta(E_{\nu} - E_F) \cdot \delta(E_{\mu} - E_F) \quad (3.15)$$

The difficult part in this equation is evaluating the tunneling matrix elements. The simplest way will be to choose the sample surface as evaluation surface written as<sup>79</sup>:

$$M_{\mu\nu} = \frac{\hbar^2}{2m} \int d\vec{S} \cdot (\Psi_{\mu}^* \vec{\nabla} \Psi_{\nu} - \Psi_{\nu} \vec{\nabla} \Psi_{\mu}^*) \quad (3.16)$$

The actual atomic structure of the tip is generally not known. However Tersoff and Hamann showed that the tip wave functions can be approximated by those for an s-wave, i.e. spherical symmetric from a point source. This is a rather realistic model of the tip and for small voltages (3.15) reduces to:

$$I \propto \sum_{\nu} |\Psi_{\nu}(\vec{r}_0)|^2 \delta(E_{\nu} - E_F) \equiv \rho(\vec{r}_t, E_F) \quad (3.17)$$

The right hand side of this expression is simply the local density of states (LDOS), i.e. the charge density from states at the Fermi level on the surface right below the tip position. The s-wave approximation for the tip is valid for many surfaces however Chen et al. showed that for particularly close-packed metals the type of tip wave function is crucial for the surface corrugation in the STM image.<sup>80</sup>

The formalism above is widely used since it incorporates the band structure and the surface density of states into the calculations in a convenient way. Another theoretical approach would be to solve the Schrödinger equation in a scattering approach by matching an incoming wave with a reflected and a transmitted wave.

### 3.3.3 Constant Current Mode – Types of STM Images

As the tip raster over the surface the piezo crystal is adjusting the tip-sample distance to restore a constant current chosen by the operator. This is called constant current mode and gives a conventional “topographic” image of the surface which virtually always serves as the initial step in a STM experiment. The step size in the (x,y) plane represents the lateral

resolution of the data recording and in this work  $400 \times 400$  data points per frame is used. As an example, for a  $100 \times 100 \text{ nm}^2$  large image this corresponds to lateral resolution limit of 0.25 nm. This is in the same range of the atomic lattice spacing of graphene and SiC hence smaller scans are necessary if atomic resolution is wanted ( $\sim 15 \times 15 \text{ nm}^2$  and smaller). The z height resolution is independent on scan size and therefore structures such as atomic steps can be seen even on very large STM images. The physical quantity measured by STM is the tunneling current which is the function of  $\mathbf{x}=(x,y)$  and the sample-tip distance z:

$$I = I(\mathbf{x}, z) \quad (3.18)$$

The electronic feedback loop is responsible to keep the current constant at all times during the scan. When the tunneling conditions are changed in between two data acquisition points the current will change quicker than the feedback loop can respond, which will result in a “error” of the set point current  $\Delta I(\mathbf{x}, z)$ . An image based on the error signal is here simply called a current image. By varying a so called loop gain and the time interval between adjacent data points, the operator can control how fast the feedback loop should response to  $\Delta I(\mathbf{x}, z)$ . A too high loop gain will result in an amplified noise signal which will disturb the total signal. Too low gain may cause the tip to crash into the sample. If the applied voltage over the piezo crystal (in order to adjust the tip position caused by  $\Delta I(\mathbf{x}, z)$ ) is considered, a topographic STM can be collected. Topographic and current images in constant current mode are the most common ways to present STM data and are extensively utilized in this work.

### 3.3.4 Imaging SiC and Graphene with STM – Bias Voltage Dependency

Imaging semiconductor surfaces such as SiC often requires applied voltages of several volts. At these non-neglectable values of the applied bias the model by Tersoff and Hamann will not be appropriate for describing the tunneling current.

An extension of equation (3.17) is therefore needed to treat semiconductor surfaces with their discontinuous density of states. The tunneling current when imaging at finite applied biases is commonly written, based on the WBK approximation as<sup>81</sup>:

$$I(z, V) = \frac{\pi e \hbar^3 A}{2m^2} \int_{E_F}^{E_F + V} \rho_S(E) \rho_T(E - eV) T(z, V, E) dE \quad (3.19)$$

Where  $\rho_S$  and  $\rho_T$  is the density of states of the sample versus tip respectively.  $A$  is the effective tunneling junction area and  $T(z, V, E)$  denotes the transmission function which account for the exponential increase of current with increased voltage.

Equation 3.19 is important to keep in mind when interpreting STM images of bare SiC or graphene covered SiC surfaces. SiC a wide bandgap semiconductor in contrast to graphene which is a semi metal with no bandgap. Therefore, imaging bare SiC requires high voltages in the regime 1-3 eV but graphene can be imaged down to a few meV. In the case of epitaxial graphene on SiC(0001) both LDOS of the substrate interface and the graphene has to be considered. At small applied voltages graphene LDOS will have the most significant contribution to the tunneling current where the honeycomb lattice can be imaged. As the voltage is increased the SiC interface will be imaged simultaneously and completely dominate the tunneling current at around  $\pm 1.5$  eV. This makes graphene to appear transparent

at high voltages which can be beneficial when studying the interface layer as will be demonstrated in chapter 7.

### **3.4 Spectroscopy Using STM Tunneling Current**

Tunneling Spectroscopy allows additional dimensions in acquiring chemical and electronic properties of conductive surfaces. The merits of tunneling spectroscopy with an STM benefits from the precise locality and pre-selectivity under well defined conditions. Since the tunneling current is proportional to the density of states of the surface makes it possible to measure local electronic spectra with high energy resolution while collecting an STM image. The tunneling spectra energy window is limited to few eV on either side of the Fermi level as higher energies will access the field emission regime when voltage biases overcome the sample work function.

Tunneling spectroscopy can be accomplished in several different ways. I will here describe two STS techniques that have been used in this work: current-voltage spectroscopy and constant-current tip-sample distance spectroscopy.

#### **3.4.1 Current-Voltage Spectroscopy (I-V)**

I-V Spectroscopy relying on the tunneling phenomena was actually first demonstrated over two decades before the invention of the STM. The year of 1960 Giaever conducted revolutionary tunneling spectroscopy studies using two macroscopic planar electrodes separated with a very thin uniform isolated film as the tunneling junction.<sup>82</sup>

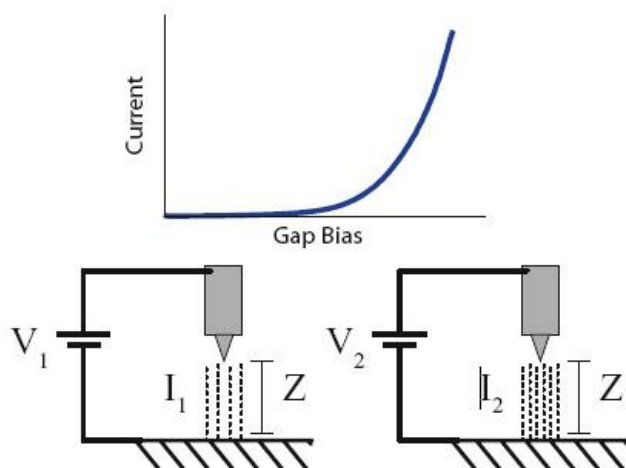


**Figure 3.11** Schematic of current-voltage (I-V) spectroscopy in STM. Taken from [81]

A sweep of applied voltage over the electrodes resulted in a tunneling current and its differentiated tunneling conductance could be correlated to the density of states of the sample electrodes. An I/V curve in STM is collected in the same manner keeping the tip at a constant height over the sample simply by disengaging the feed back loop. This method is by far the most common technique for doing spectroscopy with an STM and has been demonstrated on all kinds of surfaces. The characteristics of an I/V spectra and the fixed height positioning of the tip is visualized in figure 1. A first derivative of the spectra ( $dI/dV$ ) will reflect the sample local density of states (LDOS) as justified from Giaever's planar junction experiments.<sup>82</sup> However as the voltage is increased, current will rapidly increase due to the background tunneling transmission function growing exponentially (equation 3.19). To account for this  $dI/dV$  can be normalized in a way to better present LDOS:

$$\frac{V}{I} \frac{dI}{dV} \propto \rho_s(eV) \quad (3.20)$$

To avoid signal to noise level to increase by numerical differentiation a lock-in amplifier can be used to directly measure a dI/dV signal. The same principle applies here as for Auger Spectroscopy lock-in detection described above where a modulated AC signal is added to the DC tip-sample voltage. It is important that the modulation frequency is chosen at a significantly higher frequency than the response of the feedback loop, usually frequencies in the order of kHz is sufficient. The use of lock-in dI/dV opens up the possibility of collecting spectroscopy images at the fixed voltages used during normal imaging operation, so called dI/dV mapping. Instead of having the integrated density of states to contribute to the tunneling (equation 3.19), dI/dV mapping will give electronic structures at an energy slit in LDOS at chosen voltage. The energy resolution (width of the slit) is controlled by the modulation amplitude. An amplitude of at least a few 10's of meV is required at room temperature acquisition to avoid the signal drowning in the thermal broadening of about 100 meV at room temperature.<sup>76</sup>

### 3.4.2 Tip-Sample Distance-Voltage Spectroscopy (Z-V)

Even though I-V spectroscopy is widely used and popular it suffers from the fact that the current is drastically increased as the voltage is increasing which may disturb or interrupt the surface to be measured. This is avoided in Z(V) spectroscopy where a small constant current is maintained throughout the whole spectra.

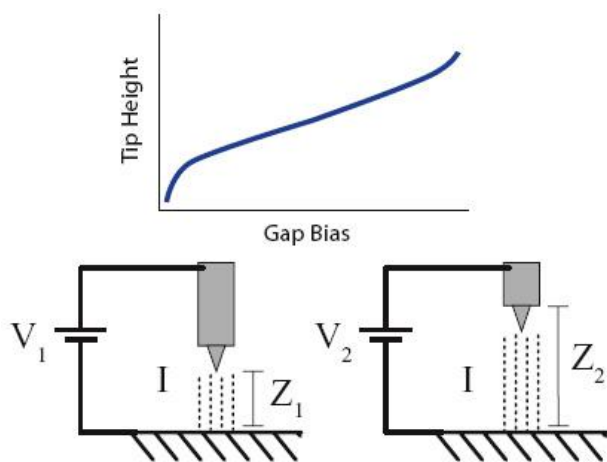


**Figure 3.12** Schematic of tip-sample distance-Voltage (Z-V) spectroscopy in STM. Taken from [81].

The principles for this technique is simple (figure 3.12): The tip is positioned over a certain spot over the surface and the voltage is swept while the feed back loop is engaged (constant current). As the voltage increases the tip will retract to maintain the chosen current set point. This tip motion is proportional to the tunneling probability which results in an increased retraction rate at voltage regimes with enhanced LDOS. Z(V) method serves suitable to study barrier resonances at large positive biases for the purpose of characterizing local surface potential variations. Possible disadvantage with this method may be when acquiring spectra at negative and positive bias simultaneously because of the risk of tip crash when crossing zero voltage.

In this work I have used z(V) to study image potential derived states for graphene on SiC(0001). These states are unoccupied and can be probed at several eV above the Fermi level. At these high bias voltages Z-V is superior over regular I-V spectroscopy because the

current can be kept at a low finite value. The image states have high LDOS and are therefore visualized as abrupt step-like features in the  $Z(V)$ . The spectra are best represented in a numerically differentiated plot ( $dZ/dV$ ) where image states appear as obvious peaks.

## **4: SELECTIVE Si-ETCHING ON SiC(0001) BY ATOMIC HYDROGEN TO AVOID PIT-FORMATION DURING GRAPHENE GROWTH**

In this chapter I will describe my research involving a new way of improving graphene growth on SiC(0001). The work is motivated from my Masters Thesis from Lund University, Sweden where I characterized the growth of graphene in UHV. From this study I concluded that pit formation of the SiC occur due to spatially inhomogeneous carbon superstructure nucleation during high temperature Si-sublimation. Here I will show that the Si-sublimation can be facilitated by selective surface etching using atomic hydrogen.

## 4.1 Abstract

We present a novel technique of growing graphene using atomic hydrogen etching of SiC(0001) surfaces. Hydrogen atoms generated from a hot Tungsten filament selectively etch Silicon surface atoms over Carbon atoms thereby facilitating the Si-sublimation process at temperatures around 1000 °C according to Auger Electron Spectroscopy. This allows for an extrinsic control of the interfacial buffer layer formation growth to yield reduced roughening of the SiC surface that is normally taking place in regular UHV growth. We demonstrate this using Scanning Tunneling Microscopy (STM) and can also precisely monitor the initial SiC step bunching taking place for the 6H-SiC(0001) upon annealing.

## 4.2 Introduction to Selective Si-Etching on SiC(0001) by Atomic Hydrogen to Avoid Pit-Formation During Graphene Growth

On the Si-terminated polar surface of SiC it was shown in 1975 that “monocrystalline graphite monolayer films” could be grown controllably in a UHV environment simply through thermal induced Si-sublimation of the SiC crystal.<sup>18</sup> Almost 3 decades later, In 2004 the interest emerged for such monolayer graphite film, defined as *epitaxial graphene*, on SiC as it was demonstrated to have interesting electronic properties that of a spatially confined two-dimensional electron gas.<sup>4</sup> Further experiments the same year on exfoliated graphene from graphite crystals fully ignited an intense research era on graphene because it was clearly demonstrated graphene could exist experimentally having extraordinary field effect mobilities.<sup>16</sup> Hidden in graphene’s unique electronic structure were charge carriers behaving

like relativistic particles with zero rest mass, aka Dirac-like fermions<sup>17</sup> that exhibit an unusual half-integer quantum Hall effect and non-zero Berry's phase.<sup>83</sup> These are quantum transport properties which make graphene a top candidate to serve as a platform for future novel carbon-based electronic devices. From a technological application point of view, the choice of substrate to support graphene is perhaps the most crucial challenge in order to avoid disturbing these unique electronic properties. From that perspective, graphene grown on SiC is a viable route towards graphene based electronic circuits because rather straightforward methods of Si-sublimation allow nearly isolated graphene to be formed onto the insulating SiC substrate.<sup>4</sup> The methods of growing flat large-area graphene on SiC(0001) have been remarkably improved during the last 4 years. The standard and most simple technique is to heat up a SiC(0001) surface to 1300 °C in UHV which will result in Si-sublimation. As a result, liberated carbon then forms a complete layer of graphene separated from the SiC surface by a carbon-rich interfacial layer, the so-called "buffer layer". However, this simple approach results in surfaces pitted morphology which will degrade graphene transport performance and impede further device construction. Sparse reports exist on the processes involved in this growth that explain the origin of pit formation on the SiC surface because it is difficult to monitor real time dynamics of the hot (above 1000 °C) SiC surfaces using common surface science techniques. Tromp and Hannon presented an excellent study of the growth kinetics that showed Si-sublimation to initially take place parallel to the surface by surface step etching where irregular etching causes pit formation.<sup>84</sup> Hupalo et al. show

that the SiC will remain flat during graphene growth if sample is *rapidly* flashed to temperatures of 1200 °C in UHV in order to minimize the time allowed for pit formation.<sup>85</sup> The most standard technique to date is however to grow the graphene at much higher background gas pressures which will significantly improve the graphene morphology by eliminating pit formation. Revolutionary reports on this method used close to atmospheric pressure of inert Argon gas at SiC temperatures between 1650-2000 °C.<sup>86, 87</sup> IBM used a background pressure of disilane to establish a thermodynamically stable phase transformation from Si-rich to carbon-rich surface superstructures.<sup>88</sup> Recently de Heer et al. demonstrated improved graphene growth by encapsulating the SiC crystals in graphite enclosures during high temperature annealing.<sup>89</sup>

Common to all these above mentioned methods is the ability to suppress and slow down the direct Si-sublimation into vacuum/growth chamber to reach more controllable growth conditions. A disadvantage of these methods is that they require exceptionally high temperatures which result in significant step bunching on the SiC substrate.<sup>86</sup>

In this report we show a completely different way of improving the graphene morphology. Rather than suppressing the Si-sublimation by using high background pressures we instead facilitate the Si-sublimation by use of atomic hydrogen etching to uniformly form the buffer layer. This allows the use of much lower temperatures while also avoiding massive step bunching of the SiC. Hydrogen-based processing is already commonly used in this research field for two crucial purposes. First to create an atomically flat SiC substrate, a technique of removing scratches from a standard mechanical polished polar SiC surface was

established.<sup>90-91</sup> By exposing the surface to molecular Hydrogen in the atmospheric pressure range and at sample temperatures of 1550-1700 °C an atomically flat surface can be obtained. At these temperatures and pressures, both Si and C atoms are isotropically etched away from the surface.

Second, hydrogen is reported to intercalate underneath the SiC-interfacial layer on SiC(0001) and saturate dangling bonds of the top-most substrate Si atoms. Remarkably, this results on a decoupling of the interfacial layer to transform it into a true, essentially neutral graphene layer.<sup>92-93</sup> .<sup>39</sup> Hydrogen intercalation was demonstrated using either molecular hydrogen at 1000 °C and atmospheric pressure or with atomic hydrogen at a pressure of  $\sim 5 \times 10^{-6}$  mbar and sample temperature  $\sim 700$  °C.<sup>93</sup> Our study reports on an additional use of hydrogen which can be integrated in a complete graphene formation and isolation cycle using *solely* hydrogen for surface planarization, buffer layer growth (described herein), and buffer layer-SiC substrate decoupling by atomic hydrogen intercalation.

### 4.3 Experimental Procedure

Highly n-doped 6H-SiC(0001) 2-inch wafers, nominally on-axis cut substrates from Cree were used. The as-received samples were CMP polished (NovaSiC) to render single bilayer SiC steps throughout the wafers. All samples were degreased by sonication in methanol for 20 minutes, acetone for 5 min, and deionized water for 5 minutes followed by removal of native oxide by dipping the sample in 10% hydrofluoric (HF) acid for 15 minutes. Prior to introduction of samples to an Omicron UHV multipurpose system samples were again dipped in de-ionized water then blown dry in a N<sub>2</sub> flow. As a final step of sample preparation the

samples were outgassed *in situ* for several hours to remove hydrocarbons and other residues from air exposure and degreasing. Carbon-rich superstructures were grown by heating the sample using direct current heating through the sample in an atomic hydrogen atmosphere generated by a hot Tungsten filament. The filament used was a thin 0.008 mm W-ribbon approximate area of  $(13 \times 4) \text{ mm}^2$  positioned 7 cm from sample surface. By resistive heating using a 9 A current resulted in a filament temperature of about 1500 °C. Ultra clean hydrogen gas was introduced to the chamber from a leak valve during the experiment which then interacts with the hot W-filament surface to form atomic hydrogen species. Since we can not accurately determine the cracking efficiency of the molecular hydrogen, pressure will be given in total pressure measured with a standard vacuum ionization gauge. For comparison graphene samples were also prepared using the more standard UHV approach by heating to 1300° C in a UHV environment with base pressure of  $5 \times 10^{-11}$  mbar. Sample temperature was monitored continuously during all experiments using an Ircon pyrometer set at emissivity 0.90.

#### **4.4 Results and Discussion**

We shall start by examining the graphene nucleation process on SiC(0001) surface upon standard thermal annealing in a UHV environment using AES and STM. These experiments will illustrate at what temperatures the Si sublimation and roughening of the surface starts to take place and will help to understand why graphene becomes pitted and non-uniform by UHV annealing.

The first step in creating graphene in UHV involves desorption of the native oxide always present on the surface despite HF treatment of the samples. Annealing of several samples with subsequent Auger Spectroscopy analysis demonstrates that oxygen desorbs from the surface at 900 °C. Figure 4.1a prove this statement where Auger scans show a sample annealed to 850 °C (black scan) and 900 °C (red scan) for 3 minutes.

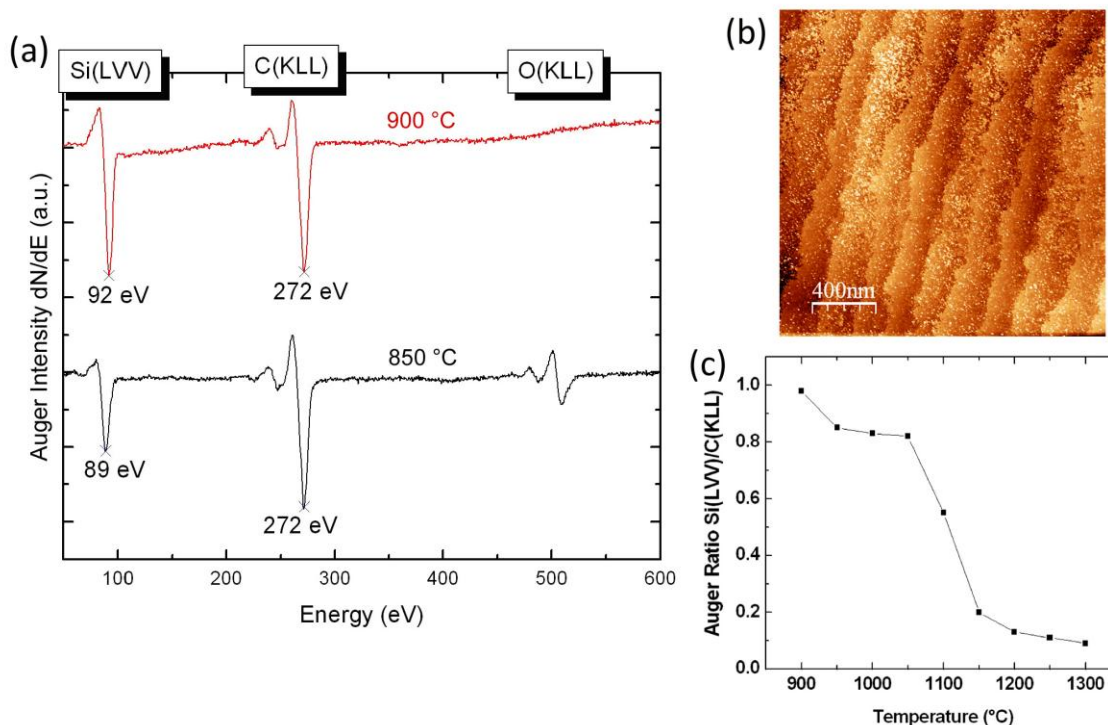


**Figure 4.1** (a) Auger electron spectroscopy of sample annealed to 850 °C (black curve) and same sample annealed to 900 °C for 3 minutes (red curve). (b) STM image of same sample annealed to 900 °C showing a bare SiC(0001) surface with step heights  $\sim 2.5$  Å. Note every third step is more rough and dissolved compare to the other steps. (c) Auger intensity ratio of Si/C peaks with respect to annealing temperature in UHV. At each data point a same sample has been annealed for 3 minutes.

The oxygen peak in the 850° C spectrum is unchanged from an as-loaded sample but is completely removed after the slightly higher 900 °C annealing procedure.. STM scans (fig. 4.1b) on the bare SiC(0001) surface after 900° C annealing show an atomically smooth surface of SiC( $\sqrt{3}\times\sqrt{3}$ )30 superlattice (confirmed by LEED, not shown) and with step heights of  $\sim 2.5$  Å, corresponding to single bilayer SiC steps. Importantly for our study, the use of CMP treated SiC samples allow us to observe the initial step bunching process during annealing because the surface is composed of single SiC-base steps. This contrasts with hydrogen-etched samples where a significant step bunching has already taken place and so cannot be correlated with growth and etch pit formation processes.

Our 6H-SiC surface is composed of an equal amount of individual bulk terminated surface terraces layer stacking sequences called S1, S2 and S3 (and their identical counterparts S1\*, S2\* and S3\* rotated 60°) after the terminology introduced by Starke.<sup>94</sup> The integer relates to the number of identical bilayer sequences before the occurrence of a 60 degree stacking fault in the 6H unit cell. Every third step across the surface in Figure 4.1b has a “rough” step which is partially dissolved into small islands distributed across the terrace on the lower side of these steps. This can be identified as the initial stage of Si-sublimation directly from the edges of particularly fast moving S1(S1\*) steps which will result in step bunching as described below. First let us examine AES of the Si-sublimation of our initial clean SiC surface (fig 4.1b) towards graphene growth for temperatures between 900 °C to 1300 °C. This is displayed by the plot in figure 4.1c of the ratio of Si and C Auger signals as the temperature is increased. The initial sublimation is slow up to about 1050 °C after it

obviously accelerates as we use higher temperatures. At about 1150 °C the sublimation rate is again significantly reduced until we reach our maximum temperature of 1300 °C. A dramatic change in surface composition is apparently taking place at 1050 °C and around this temperature we focus extra attention for further STM imaging. Figure 4.2a show the surface after annealing to 1050 °C for 3 minutes. Every third step initially roughened as described by figure 4.1b has now *completely* been etched away resulting in alternating double- and single SiC bilayer steps across the surface (see line profile fig. 4.2a).

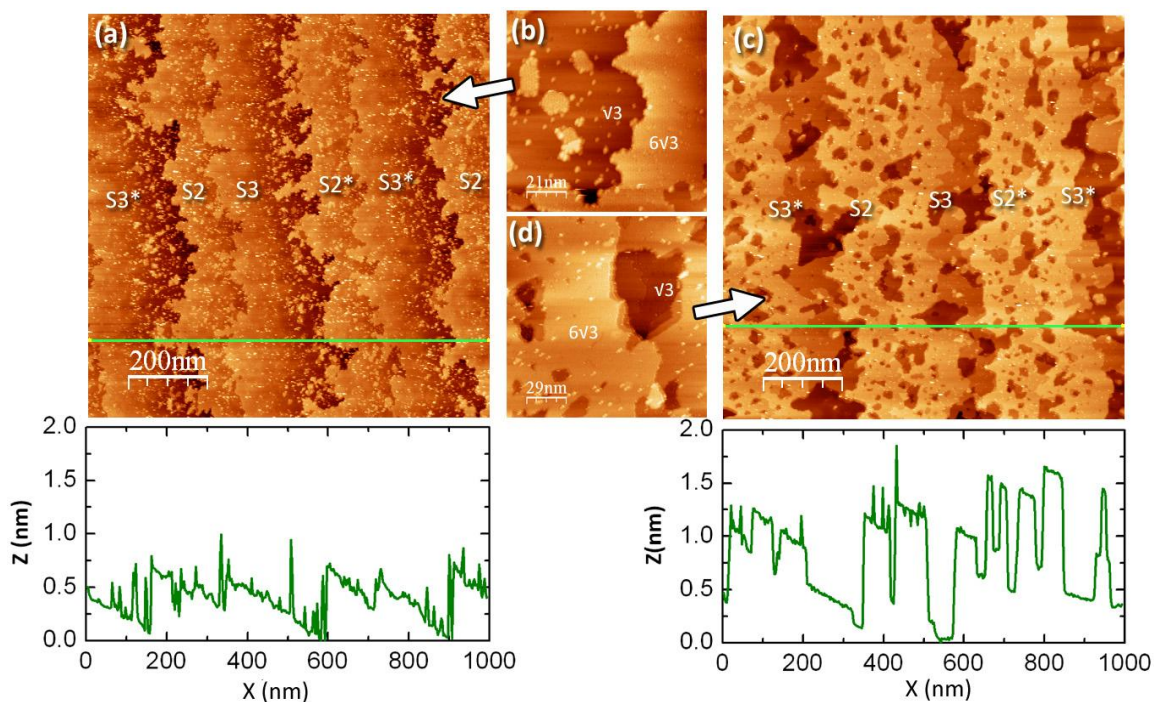


**Figure 4.2** (a) STM image and line profile of sample annealed to 1050 °C in UHV.  $I=0.1$  nA,  $U=-2$  V. (b) Close-up from a of a step separated by S3 and S2 terraces where the surface is dominated by Si-rich  $\sqrt{3}$  on the S3 terrace with random carbon-rich  $6\sqrt{3}$  domains. (c) STM image and line profile of sample annealed to 1100 °C in UHV where surface has become severely roughened. (d) close-up from c showing surface is dominated by carbon-rich  $6\sqrt{3}$  with small domains of Si-rich  $\sqrt{3}$ .  $I=0.1$  nA,  $U=2$  V.

As proposed by Hupalo et al<sup>85</sup>, one type of terrace retracts at a faster rate compared to the other two. These authors initiated rapid nucleation of graphene by fast annealing cycles of the SiC and therefore the intermediate step bunching phases shown in Figure 4.2a were not imaged. Borovikov and Zangwill performed Monte Carlo simulations on step flow etching on vicinal SiC-6H surfaces.<sup>95</sup> Their conclusion was that the S1 terrace has a faster etching rate compared to both S2 (S2\*) and S3 (S3\*) terraces. We therefore suggest that it is the S1 terraces that are catching up with the S2 terraces causing an intermediate surface morphology with alternating single ( $\sim 2.5 \text{ \AA}$ ) and double bilayer ( $\sim 5.0 \text{ \AA}$ ) SiC steps having now only S2 and S3 terraces. To our knowledge, this step bunching process has not been captured before using scanning probe microscopy. It is likely that S2 and S3 terraces have also been etched laterally to some extent but at a lower rate because we observe a significant amount of carbon-rich SiC( $6\sqrt{3} \times 6\sqrt{3}$ )R30 superstructures present on the surface as seen in fig. 4.2b. Tromp and Hannon<sup>84</sup> observed that while step etching is taking place, released excess carbon nucleates the carbon rich reconstruction at the lower side of each terrace and can diffuse across the surface. The surface condition shown in fig. 4.2a can be described as the result of this process because SiC( $6\sqrt{3} \times 6\sqrt{3}$ )R30 structure dominates the area at top sides of each terrace step while the area where S1 steps have retracted mostly contain bare Si rich SiC( $\sqrt{3} \times \sqrt{3}$ )R30 surface as seen in figure 4.2b.

Further annealing to slightly higher temperature should according to Auger spectroscopy (fig 4.1c) rapidly increase the Si-sublimation. We can confirm this by STM seen in figure 4.2c showing the same surface annealed to 1100 °C where the surface is now almost completely

covered with carbon-rich super structures. We can also notice a remarkable roughening of the surface demonstrated clearly by the profile line in the lower panel of figure 4.2c.

Interestingly the step-configuration seems to be the same as after the previous 1050 °C anneal while it is obvious that areas that were not covered with buffer layer (particularly at low sides of S2 terraces) have collapsed to form depressions. From these observations we can confidently conclude that the Si-sublimation has now started to take place *directly into vacuum* from Si-rich SiC( $\sqrt{3}\times\sqrt{3}$ )30 areas. This direct desorption from SiC( $\sqrt{3}\times\sqrt{3}$ )30 terraces to vacuum contrasts with the initial desorption *parallel* to the surface from S1 step edges. This explains why the carbon aggregation is so rapid at this point where the area for released Si atoms is much larger compared to just the steps. More importantly, it is likely that the parallel surface Si-sublimation is much faster from areas with bare SiC compared to areas covered with protecting carbon-rich buffer layer. The surface in figure 4.2a with a mix of carbon-rich versus Si-rich reconstructions will induce inhomogeneous Si-sublimation rates at different points on the surface causing severe pit formation of the SiC which is the origin of pits in the graphene formed by annealing at 1300 °C. To avoid roughened SiC surface during annealing it would be ideal to be able to controllably form a complete carbon-rich buffer layer across the whole surface at low temperatures before a rapid vertical Si-sublimation from terraces can take place. A way to accomplish this would be to find a way to assist the Si-release at lowered temperatures and allow for carbon aggregation to nucleate the buffer layer more uniformly over the surface. From multiple successful reports on etching of Si<sup>96, 97</sup>

substrates using atomic hydrogen it should be possible to selectively etch Si atoms from a SiC surface.

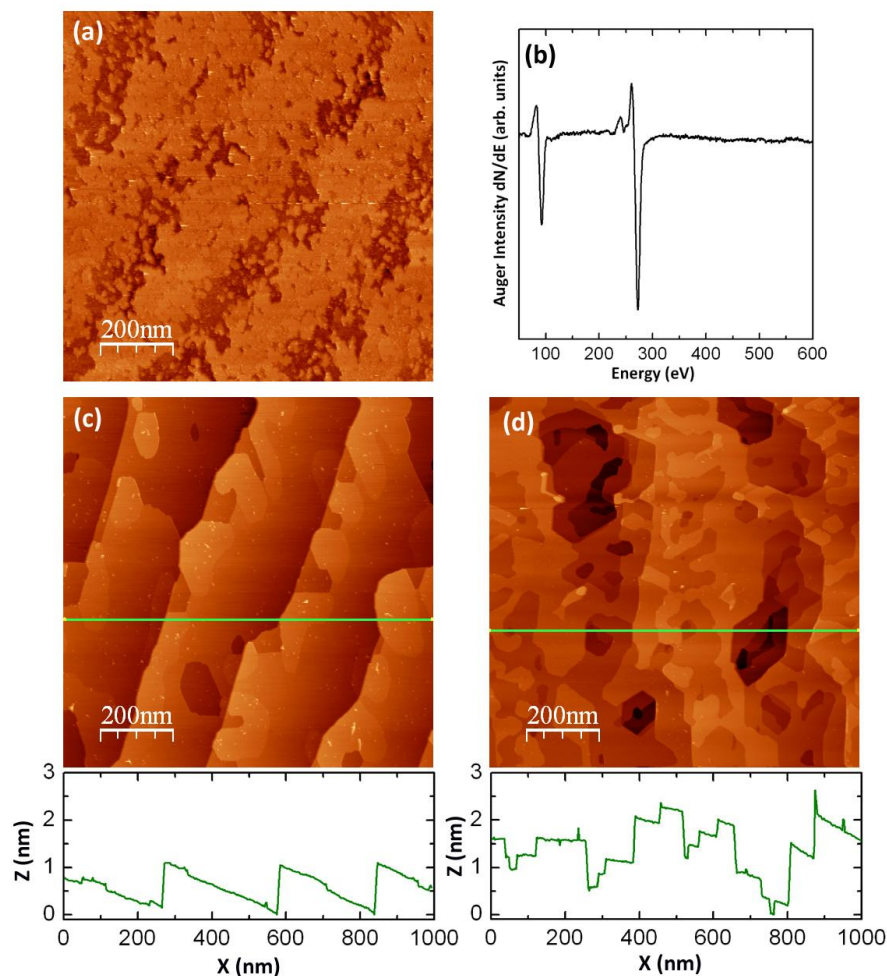


**Figure 4.3** (a) Atomic hydrogen etched surface at 1000 °C for 10 minutes at  $P=10^{-5}$  mB.  $I=0.1$  nA,  $U=-2.3$  V. (b) AES scan of hydrogen etched surface in a. (c) Same surface annealed to 1300 °C in UHV for 3 minutes.  $I=0.1$  nA,  $U=-1.9$  V. (d) Surface in figure 4.2 annealed to 1300 °C for 3 minutes.  $I=0.1$  nA,  $U=2$  V.

Figure 4.3a show a sample annealed to 1000 °C for 10 minutes while being exposed to atomic hydrogen with hydrogen background pressure of  $10^{-5}$  mbar. The surface is now

almost completely covered with carbon-rich buffer layer (as confirmed by LEED, not shown) without significantly pitting the SiC substrate. Only in areas where S1 steps have retracted during the step bunching are there still domains of bare  $\sqrt{3}$ -SiC surface as seen in fig. 4.3a. Auger spectroscopy of this surface shown in figure 4.3b proves that in fact atomic hydrogen has facilitated the Si-sublimation to form a large amount of buffer layer at a much lower temperature compared to plain UHV growth. The Si/C ratio for the Auger scan in fig. 4.3b is 0.52 which would require  $\sim 1100$  °C in UHV to achieve. It is plausible that atomic hydrogen has reacted with top-most Si atoms to form volatile SiH<sub>4</sub> species isotropically across the surface. This explanation is in agreement with earlier reports of atomic hydrogen exposure of Si-rich SiC(0001) surface but at much lower temperature, as low as room temperature.<sup>98</sup> However most importantly, the surface is much more uniform and will allow for more uniform and controlled Si-sublimation to form graphene layer on top of the buffer layer. Displayed in figure 4.3c is the same sample further annealed to 1300 °C for 3 minutes in UHV. This surface is completely covered with single layer graphene along with a small amount of bi-layer graphene and shows a remarkably flat morphology on terraces. Each step height is  $\sim 7.5$  Å which is a result of a uniform step bunching of the underlying SiC to half-unit cell heights so that the SiC substrate surface now only consists of S3 (S3\*) steps. Pit-formation normally present in a UHV-grown sample is *almost completely suppressed*. Figure 4.3d clearly demonstrates this comparison the sample in figure 4.2 (i.e. not exposed to atomic hydrogen), annealed to 1300 °C for 3 minutes. The surface is not only pitted but it has also much more irregular step edge morphology.

The above described procedure of controllably forming the buffer layer by atomic hydrogen exposure at 1000° C allows for significantly improved graphene morphology upon further high temperature UHV growth. It is not likely that the temperature where this process occurs can be lowered below 1000° C for two reasons: (1) if we expose the sample to atomic hydrogen below 500 °C the hydrogen will bond to top Si-atoms and stay on the surface. This surface passivation by hydrogen is well known for SiC and inhibits Si atom removal from the surface.<sup>99</sup> (2) during our exposure of hydrogen there is a small amount of oxygen present in the chamber. This is because the chamber is filled with a mixture of molecular hydrogen and atomic hydrogen and it is likely that atomic hydrogen will react with and release oxygen species at chamber walls and surfaces. The same phenomena has earlier been observed for hydrogen plasma exposure at 800 °C at 50 mbar which results in a ordered ( $\sqrt{3}\times\sqrt{3}$ )30 silicate adlayer on the surface.<sup>100</sup> In addition, the bare  $\sqrt{3}$ -SiC surface is extremely reactive to oxygen and any surface passivation of oxygen will completely disrupt hydrogen etching as has been reported for clean Si surfaces.<sup>101</sup> From figure 4.1a we learned that the desorption temperature for oxygen is 900 °C so any prolonged atomic hydrogen exposures below this temperature will result in a stable oxygen termination of the surface. To show this we expose a bare SiC surface to atomic hydrogen for 45 minutes at 850 °C. After such long hydrogen exposure we can detect a oxygen peak from AES suggesting we have formed a silicate layer similar to the experiments in ref. <sup>100</sup>.

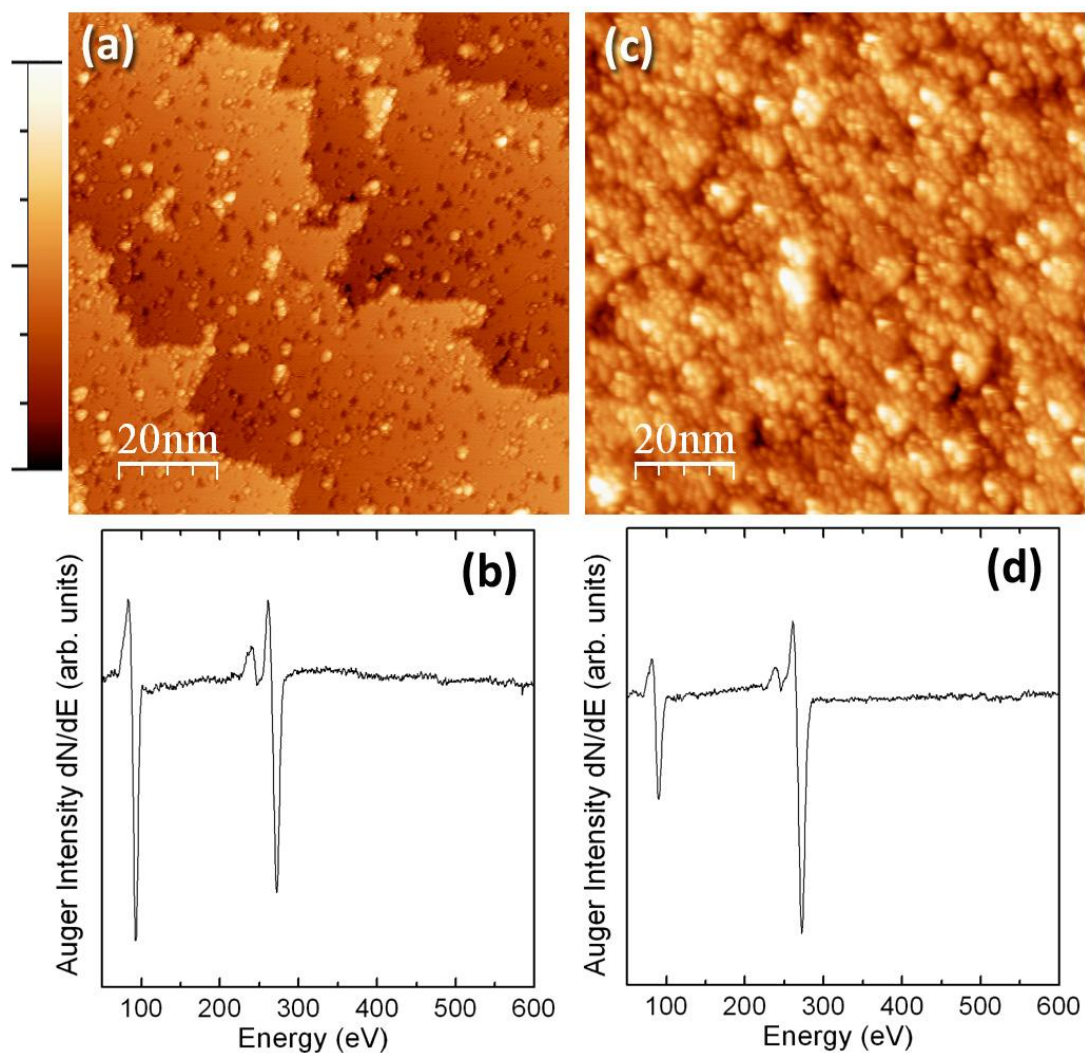


**Figure 4.4** (a) Sample exposed with atomic hydrogen for 45 minutes at 850 °C followed by a quick flash to 900 °C to remove native oxide. (b) AES of sample in a. (c) Different sample exposed with atomic hydrogen for 45 minutes at 900 °C. AES for this surface is shown in (d). Z-scale for both STM images is 1.3 nm.

We then quickly flash the sample to 900 °C just enough to remove the desorbed oxygen.

STM of this surface now reveal an extremely flat and clean  $\text{SiC}(\sqrt{3}\times\sqrt{3})\text{R}30$ , in fact the surface is even cleaner and more flat than the as-loaded sample from the CMP polishing

shown in figure 4.1b. This fact is supported by the corresponding Auger scan showing an even larger Si(LVV) peak that better represents the true stoichiometry of a clean SiC(0001) surface with regular Si-adatom ( $\sqrt{3}\times\sqrt{3}$ )R30 super structure. We repeated the experiment with atomic hydrogen exposure for the same prolonged times (45 min.) for a different sample but now with annealing temperature of 900 °C. Figure 4.4c display the morphology of this surface where barely any atomic steps can be observed. The cluster structures observed uniformly across the surface are inferred to be carbon-rich based on the AES scan shown in fig. 4.4d. The atomic hydrogen has again successfully etched away a significant amount of Si and no oxygen is allowed to stick to the surface at 900 °C. The proof of concept is however established and further improvements in this procedure would likely demand an even cleaner and more confined environment for atomic hydrogen. For example, the use of a much more efficient atomic hydrogen generator could improve this technique significantly over the simple set-up of a hot filament placed in front of the sample. In a addition, a hydrogen gas purifier may be required to avoid oxygen contaminants within the hydrogen gas that is being leaked in the UHV chamber.<sup>92</sup>

Our discovery in this paper allows for a potential complete quasi-free graphene growth cycle on SiC(0001) using *only* atomic hydrogen at low pressures and moderate elevated temperatures. The buffer layer would first be grown using the procedure described in this paper at around (1000 °C). This process will be self limiting, meaning that as a complete buffer layer has formed it will passivate the surface from further Si-etching and carbon aggregation. To transform this buffer layer to a graphene layer, the temperature needs simply

to be lowered to about 700 °C to allow hydrogen intercalation at the SiC-interface as described in earlier reports.<sup>93</sup>

## 4.5 Conclusion

We have identified the cause of pit formation during UHV growth of graphene on SiC(0001) as inhomogeneous vertical Si-sublimation directly from small  $\sqrt{3}$ –SiC domains randomly-distributed on terraces. To avoid this, we demonstrated that atomic hydrogen can selectively and *uniformly* etch Si from a SiC(0001) surface to facilitate the Si-sublimation at a lower temperature and at a more controllable rate. This results in the creation of a more uniform interfacial carbon-rich buffer layer compared to regular UHV growth. The suggested procedure could be combined with atomic hydrogen intercalation to form self limited quasi-free graphene on SiC(0001) surfaces that would be of great value to industrially-scalable graphene-based electronics.

## **5: INCOMPLETE SCREENING BY EPITAXIAL GRAPHENE ON THE Si FACE OF 6H-SiC(0001)**

In this chapter screening properties of epitaxial graphene on 6H-SiC(0001) will be presented. The following work was subject of a publication in applied physics letter in 2010, discussing the first indirect approach to probe the issue of charged impurity screening in graphene. The results demonstrate the poor screening properties by monitoring energy shifts of the image potential states at different electric fields in an STM tunneling barrier setup. These states are only accessible in the unoccupied states several electron volts higher in energy with respect to the Fermi level and it is around the Fermi level where the unique massless Dirac fermion behavior is accessible. However it is essential to explore a more complete picture of the graphene electronic structure by including image states to assess new strategies for graphene electronics. To fully understand the implication of the results in this study, extended background knowledge of the physics behind image potential states is necessary. An introduction shall here be presented to fulfill such purpose.

## 5.1 Introduction to Image Potential States

It is from a simple well known model of image charges we can derive rather complicated many-body electrostatic interactions when point charges are in the presence of boundary surfaces.<sup>102</sup> As an electric charge is located outside of an infinite perfect conductive plane at zero potential the electrostatic field will induce charge polarization in the conductive plane in order to screen the electric charge. This can be described by an equal and opposite charge placed at the mirror-image on the opposite side of the conductive plane. For a test charge of a single electron and its positive image charge will result in a coulomb interaction of:

$$V(z) = -\frac{e^2}{16\pi\epsilon_0 z} \quad (5.1)$$

Where  $z$  is the distance between the test charge and the conductive plane and zero reference energy is taken from the vacuum level of the conducting boundary. Insertion of this potential in the one dimensional Schrödinger equation with direction perpendicular to the surface and assuming infinite potential barrier at the conducting plane, will give hydrogenic-like wave functions with eigenvalues corresponding to:

$$E_n = E_{vac} - \frac{1}{16} \frac{Ry}{n^2} = E_{vac} - \frac{0.85}{n^2} \quad (5.2)$$

With  $n$  as the principal quantum number. Our test charge is hence bound just outside the surface forming Rydberg series converting to the vacuum level. These bound states are called image potential states and in a realistic situation an image state will be trapped between a gap

in the crystal potential containing the vacuum level. The maximum probability density for the first image-potential state appear several Angstroms away from the surface and increases quadratically with the quantum number  $n$ . This is in distinction to intrinsic surfaces states trapped in band gaps of free-electronlike s- and p-bands commonly known as Shockley states.<sup>103</sup> A general description of an image bound electron energies accounts from the fact that the wave functions can penetrate a non-infinite surface potential barrier with exponential attenuation. This can be taken into consideration by adding a constant to equation (5.2):<sup>104</sup>

$$E_n = E_{vac} - \frac{0.85}{(n-a)^2} \quad (5.3)$$

The constant,  $a$  is called the quantum defect and is a product of a multiple scattering approach developed by Echenique and J.B. Pendry.<sup>104</sup> Upon multiple reflections of the bound image state wave function between the bulk crystal and surface barrier a phase change is induced that depend on the structure of the gap in the crystal,  $\Phi_C$  and on the potential barrier on the vacuum side,  $\Phi_B$ . The condition for a bound image state is fulfilled when  $\Phi_C + \Phi_B = 2\pi n$  and the quantum defect is proportional to the crystal induced phase to be written as:

$$a = \frac{1}{2} \left( 1 - \frac{\Phi_c}{\pi} \right) \quad (5.4)$$

Image potential states has been detected on several metal surfaces by methods that can probe unoccupied states such as inverse photoelectron spectroscopy (IPES).<sup>105</sup> **Fel! Hittar inte referenskälla.** shows a typical IPES spectra that includes the first Rydberg series member

$n=1$  for various metal surfaces. The binding energy show values close to the hydrogenic binding energy of equation (5.3) which indicates that the simple Coulombic image potential dominates the energy balance.

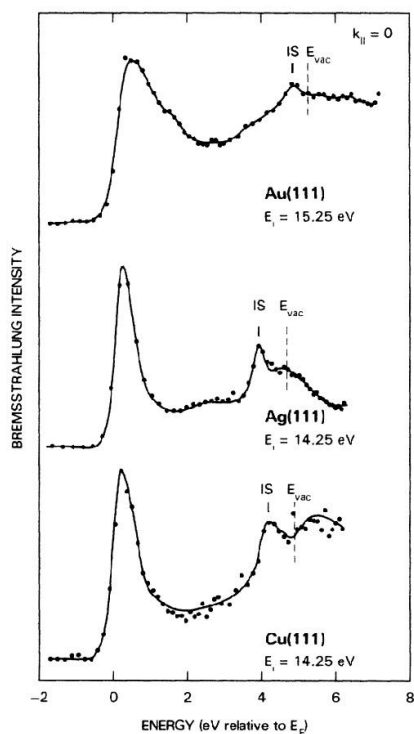


**Figure 5.1** Inverse photoemission spectra for Au(111), Ag(111), and Cu(111) for normal electron incidence. Image potential states are denoted IS. Taken from [105]

Time-resolved two-photon photoemission can also be used to probe IPS and has the advantage to resolve dynamics including image state lifetimes.<sup>106</sup> The life times may vary from a few femtoseconds to a picosecond depending on the surface material and crystal orientation. The image potential states are delocalized in the surface plane and show therefore a free electron like dispersion when the 2PPES is measured in incident angle resolved set-up.<sup>107</sup>

With a non-local one-particle potential in the vacuum side and with a long-range image potential- local density approximation hybrid for the crystal potential side, Image states can be reproduced using the density functional theory (DFT) framework.<sup>108</sup>

Image potential states have a high local density which makes them ideal to probe with an STM tip. With high spatial and energy resolution the STM allows local investigation of image potential phenomena in advantage to area-averaged experiments provided by 2PPE and IPE. Analyzing image potential spectra acquired in an STM requires additional wariness due to the strong electric field present in the tunneling junction. The electric field will cause a distortion of the image potential states by continuously shifting and expanding the hydrogenic spectrum, a phenomena referred to as “stark shift”.<sup>109</sup> The stark shift has shown to be strongly dependent on the detailed shape of the electrostatic potential at the surfaces.<sup>110</sup> The measurement artifact of the Stark shift in STM is particularly interesting in the case of graphene to gain further knowledge of possible charge impurity screening where the tip serves as a test “charge impurity”.

## **5.2 Abstract**

A biased scanning tunneling microscope (STM) tip is used to study the ability of carriers in graphene to screen external electrostatic fields by monitoring the effect of tunneling-junction width on the position of image potential-derived surface states. These states are unusually sensitive to local electric fields due to the STM tip in both single layer and bilayer epitaxial graphene. This is attributed to the incomplete screening of applied fields in epitaxial

graphene on SiC(0001). Our observations imply that charged impurity scattering is likely to be a dominant factor in the transport properties of epitaxial graphene on SiC.

### **5.3 Introduction to Incomplete Screening by Epitaxial Graphene on the Si Face of 6H-SiC(0001)**

Epitaxial graphene (EG) grown on SiC may be the most straightforward processing method for adapting the unique transport properties of this promising material to commercial applications.<sup>111</sup> It has shown remarkable 2D properties and a clear relationship<sup>112-114</sup> to the nearly ideal single-layer graphene sheets that can be created by exfoliation<sup>115</sup> or by sophisticated suspension techniques.<sup>43</sup> Despite an increasing number of transport studies<sup>111, 116</sup>, direct comparisons between the electrical transport properties of epitaxial graphene and these more idealized forms cannot be made since graphene on SiC has not yet been gated. In the absence of direct comparisons, it is crucial to develop experiments, such as the scanning tunneling spectroscopy described in this letter that will help to reveal the transport properties in epitaxial graphene on SiC.

For epitaxial graphene, room temperature Hall mobilities are high ( $\sim 1000 \text{ cm}^2/\text{Vs}$  on the Si face<sup>116</sup>) and 2D coherent scattering effects<sup>113</sup> and Landau levels<sup>117</sup> have been demonstrated. Nevertheless, the role of the SiC substrate is very significant. On the Si face of SiC(0001), epitaxial single layer graphene (SLG) is doped with electrons from the substrate so that the Fermi level intersects the upper Dirac cone (i.e. the conduction band) at a Fermi energy of  $\sim 0.2 \text{ eV}$ .<sup>114</sup> Bilayer graphene (BLG) on this surface is also doped by the substrate and exhibits a clear gap at the Dirac point due to interlayer coupling.<sup>112</sup> A major limitation in our

present understanding of the potential value of epitaxial graphene on SiC is that it has not yet been gated so its field-effect transport properties cannot be directly compared with exfoliated graphene. Exfoliated graphene has shown much higher field effect mobilities of 10,000  $\text{cm}^2/\text{Vs}$ <sup>118</sup> and suspended graphene has even higher mobilities of up to the intrinsic limit of 200,000  $\text{cm}^2/\text{Vs}$ .<sup>43</sup> In these systems, it is likely that charged impurities, which are either adsorbates<sup>119</sup> or gate-dielectric impurities, are primarily responsible for limiting the conductivity.<sup>44, 120</sup> A crucial question that must be answered about epitaxial graphene on SiC is whether the dominant scattering mechanism is the same as in the more heavily-explored exfoliated graphene. Our experiments probe this issue of charged impurity screening in epitaxial single layer and bilayer graphene on SiC(0001) by employing an STM tip as controlled charged “impurity”. We find that both SLG and BLG (Figure 5.2a) are equally ineffective in screening the applied field due to an STM tip. This allows the inference that charged impurity scattering is likely to be a dominant factor in the transport properties of epitaxial graphene on SiC.

We probe the comparative screening effects for epitaxial SLG and BLG on SiC(0001) by focusing attention on image-potential-derived surface states. These are states of an electron bound just outside of a solid surface by the polarization induced in the near-surface region (Figure 5.2c).<sup>121, 122</sup> They usually form a Rydberg series converging on the vacuum level. In STM measurements, image-potential states are “Stark-shifted” by the strong electric field of the STM tip.<sup>110, 123, 124</sup> Their energies are raised compared to zero field values (e.g. as measured by inverse photoemission) and their spacings are expanded to become more

uniform (Figure 5.2d). Image-potential states on graphene exhibit some unique features arising from reduced dimensionality. Silkin et al.<sup>125</sup> recently used hybrid pseudo-potential methods to predict a *double* Rydberg series of image states with even and odd symmetry with respect to reflection through the graphene plane. The most strongly bound state (named  $n=1+$ ) was argued to be the parent of the long-studied interlayer state of graphite<sup>126</sup> due to its spatial location at half the interlayer spacing in graphite. Remarkably, evidence for the first two members of the double Rydberg series was obtained by Bose et al.<sup>127</sup> in scanning tunneling spectroscopy experiments on epitaxial graphene on SiC(0001). The  $n=1+$  state was observed as a weak shoulder in tunneling conductance measurements at just above 3 eV above the Fermi level. The  $n=1-$  state was observed as a sharper feature close to 4 eV above the Fermi level. These experiments also support the close relationship between the  $n=1+$  state and graphite interlayer states. Our experiments focus on the  $n=1-$  state, which is analogous to the typical  $n=1$  image states studied on metal and semiconductor surfaces and can provide comparative insights into the screening properties of graphene.

## 5.4 Methods

Experiments were performed in a multichamber ultrahigh vacuum system. Graphene was prepared on the Si face of 6H-SiC(0001) crystals (Cree, N-doped) by first outgassing the SiC at 770 K overnight and then flashing to  $\sim 1500$  K. Sample cleanliness and graphene formation were confirmed by Auger electron spectroscopy and low energy electron diffraction as well as high resolution STM imaging (Figure 5.2a and 5.2b).

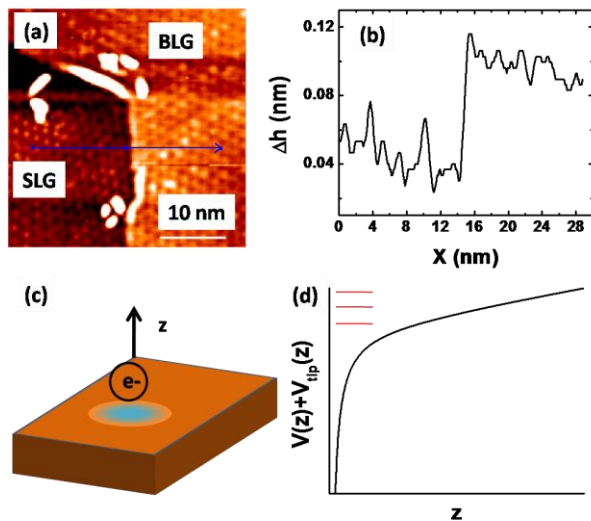


**Figure 5.2** (a) STM image (36nm x 36nm) of coexisting single layer and bilayer graphene; (b) Line profile across the blue line marked in part a showing the apparent height variation across the SLG to BLG boundary; (c) Schematic depiction of an electron bound just outside of a surface by polarization it induces; (d) Schematic depiction of (Stark shifted) image potential derived states (horizontal red lines) in an STM experiment where a potential well is created by the combined image potential and linear potential between the tip and sample.

STM was carried out at room temperature with electrochemically-etched W tips in a commercial variable temperature STM (Omicron, VT-AFM/STM). Tunneling spectroscopy was carried out in constant current distance-voltage mode, which has been extensively applied to the study image potential-derived states.<sup>110, 123, 124</sup> Tunneling junction bias was increased with constant current feedback engaged so that the tip retracts to maintain the current set-point. It has been established that this measurement protocol results in an approximately constant electric field in the tunneling junction during the spectroscopic sweep.<sup>128</sup> Resonant tunneling through Stark-shifted image potential states appears as an abrupt retraction of the tip away from the surface. Numerical differentiation of the distance

voltage spectra shows sharp peaks corresponding to the IPS's. Our approach is to vary the current setpoint at fixed initial junction bias (0.5 eV, which along with current setpoint determines the initial tip-to-sample distance) in order to systematically vary the electric field applied to our epitaxial graphene samples.

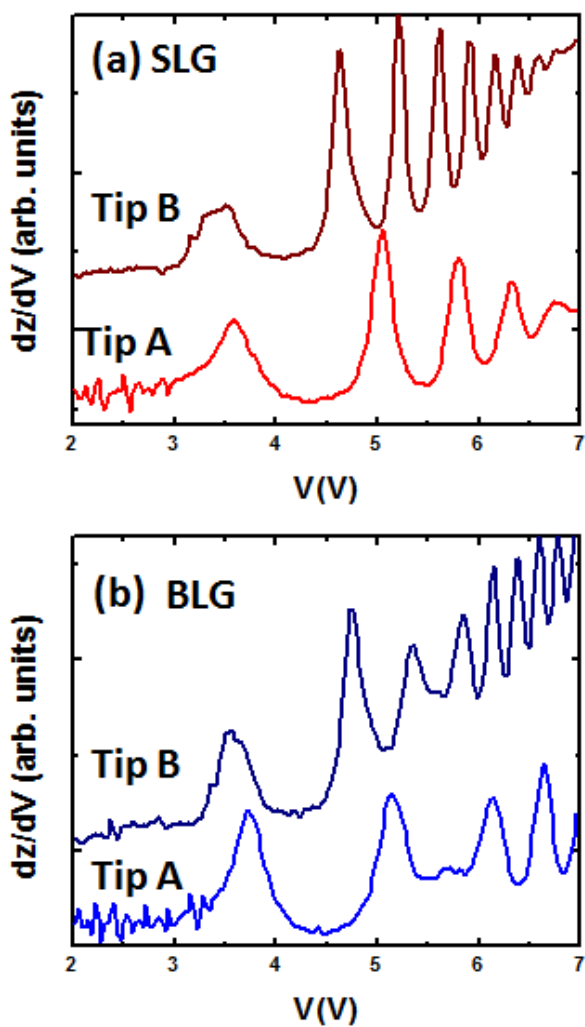


**Figure 5.3** Changes in IPS's due to unintended tip changes; (a) Single layer graphene; (b) Bilayer graphene measured with the same two tip conditions as in part a.

## 5.5 Results and Discussion

Figure 5.2a shows an STM image of a typical surface region with coexisting SLG and BLG prepared on SiC(0001). Examples of differentiated distance-voltage ( $dz/dV$ ) spectra for both SLG and BLG in such a local area are shown in Figures 5.3a and 5.3b for different STM tip conditions. We resolve the  $n=1^-$  IPS at just below 4eV and also detect evidence for the weak shoulder corresponding to the  $n=1^+$  IPS reported by Bose et al for SLG.<sup>127</sup> Also in agreement with Bose et al. is the systematic upshift of the  $n=1^-$  peak on BLG compared to SLG. Higher energy peaks reflect primarily the STM tip properties<sup>110</sup> (i.e. the shape of the barrier potential) and are not easy to interpret as derived from states intrinsic to the graphene sample.<sup>129</sup>

In the course of our experiments we found that position of the  $n=1^-$  (and also higher  $n$ ) states often changed significantly due to random, unintended tip changes. This is illustrated in example spectra for SLG and BLG respectively measured with two different tips shown in Figure 5.3a and 5.3b. The highest energy states above 5 eV are seen to vary in position and in spacing with the tip change as has been reported for similar states on metal surfaces.<sup>110</sup> The  $n=1^-$  peak also shifts in position by several tenths of a volt after the tip change. This is remarkable since such shifts are not observed for  $n=1^-$  IPS's bound at similar distances ( $\sim 0.3$  nm) outside of metal surfaces.<sup>110, 124</sup> To make a more systematic study of this uncommon sensitivity to the details of the applied field, we measured the  $n=1^-$  peak position as a function of current setpoint. As the current setpoint increases, so does the electrostatic field in the tunneling junction.

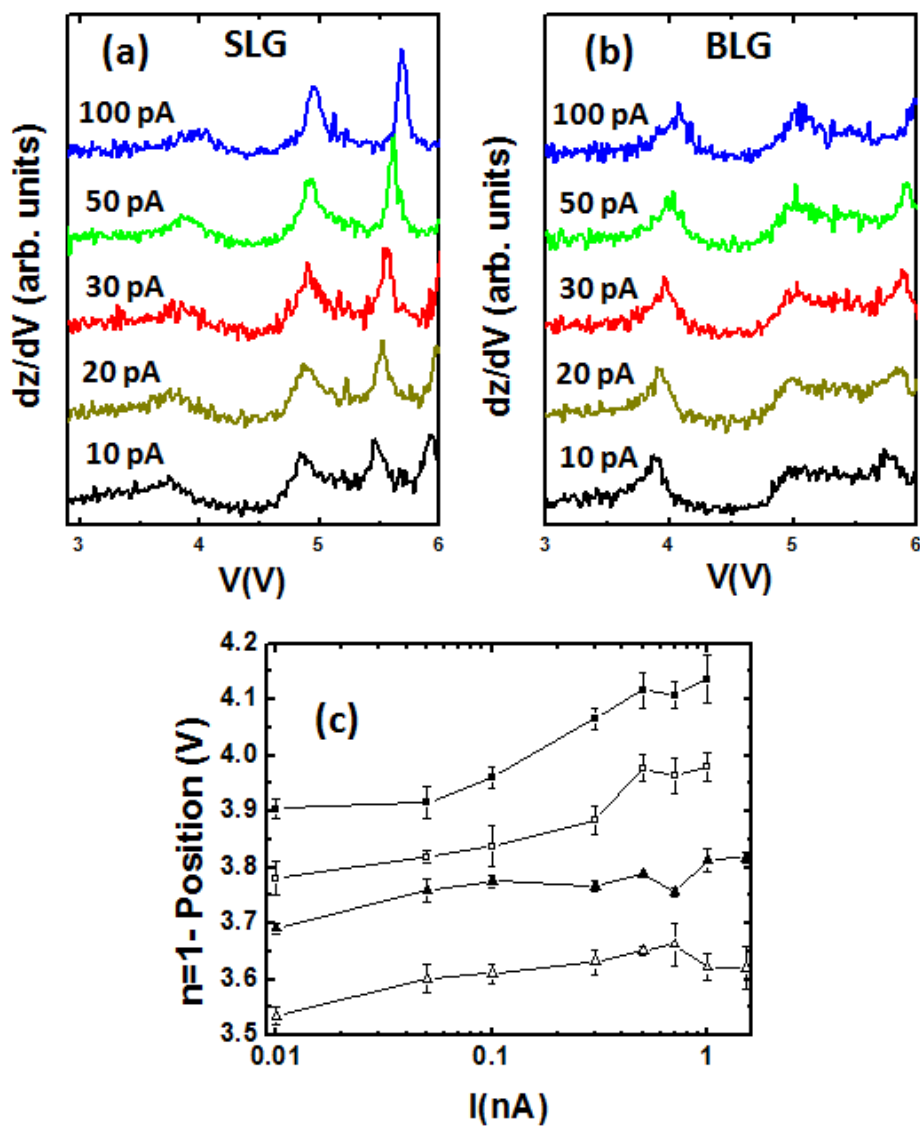


**Figure 5.4** (a) Current dependent distance-voltage spectra measured for SLG; (b) Current dependent distance-voltage spectra measured for BLG with the same tip condition as in part a); (c) Current dependent position extracted for the  $n=1$ - state of SLG (open symbols) and BLG (closed symbols). Dependencies for two different tip conditions (triangle versus squares) are shown.

Figure 5.4 shows a series of current-dependent tunneling spectra measured for SLG (Figure 5.4a) and BLG (Figure 5.4b). It is seen that the  $n=1$ - peak position shifts away from the Fermi level when current setpoint changes by as much as two orders of magnitude. Figure 5.4 shows the dependence for two different tips. We note that it is crucial to confirm by simultaneous STM imaging that the tip condition does not change at all while probing the current dependence.

The tip-induced peak-position dependence illustrated in Figure 5.4 is rather large compared to other systems where field-dependent IPS behavior has been explored by STS. For example, no current dependence has been reported for  $n=1$  IPS's on metal surfaces in the same current range to within an uncertainty of  $\sim 0.007$  eV.<sup>110</sup> This fact can be understood based on the ability of electrons in metals to efficiently screen the relatively small changes in applied electric field that result from either random tip changes or systematic setpoint current variation. The contrasting behavior observed for SLG and BLG is attributed to the incomplete screening of applied fields in this fundamentally 2D material. Despite huge carrier mobilities, graphene is very different than a metal with much lower carrier densities and thus much less free-carrier screening.

Another important point about the data presented in Figure 5.4 is that both the rate of change of peak position with current and the total magnitude of the change with current is the same for SLG and BLG. As already mentioned, there is always a systematic shift in peak position between SLG and BLG that is most likely the result of an increased work function for BLG compared to SLG<sup>130</sup>. This similarity of IPS behavior for SLG and BLG can be understood

based on the substrate-induced doping of the different layers. The effectiveness of static screening can be described by the Thomas Fermi wavevector which is proportional to density of electronic states at the Fermi level. For SLG, the Fermi level occurs  $\sim 0.2$  eV above the ideal Dirac point in the conduction band where photoemission shows that the density of electronic states of SLG is similar to that of BLG.<sup>112, 114</sup> The small reduction in substrate-induced doping for BLG apparently does not significantly alter its ability to screen the applied field of the STM tip.

Calculations of dynamical polarization in doped<sup>131</sup> and gapped<sup>132</sup> graphene also support the apparent similarity in screening behavior for the different thicknesses of epitaxial graphene. In the Thomas-Fermi approximation, the static induced charge was calculated to be the same for doped, ungapped graphene as for doped, gapped graphene. Recently, *ab initio* calculations that include the full band structure of graphene (i.e. not just the near the Dirac point) have indicated an extraordinarily diminished screening and sensitivity to local electrostatic fields.<sup>133</sup>

These observations are interesting in the context of the recent debate over the question of whether interactions with the SiC(0001) substrate open a gap around the Dirac point in SLG on the Si face of SiC.<sup>112, 114, 134</sup> Our observation of similar static screening characteristics of SLG and BLG on this surface suggests that the *practical* consequences of a gap in SLG may be minimal from the perspective of transport properties. Due to the heavy substrate-induced doping, the electronic structure near the Fermi level that is responsible for screening is very similar for the different layers regardless of the details of the dispersion near the Dirac point.

The charged impurity-limited transport properties of epitaxial graphene on SiC would be expected to depend only very weakly on whether the graphene is one or two layers thick. In summary, we have measured the tunneling current dependence of the  $n=1$ - image potential derived state for SLG and BLG on SiC(0001) as means of probing the efficiency of screening in these systems. We observe incomplete screening that is distinctly different than other tunneling measurements of IPS's on metal surfaces. This suggests that charged impurities will dominate the electrical transport properties of epitaxial graphene just as they dominate the more isolated forms of exfoliated and suspended graphene. The ability of SLG and BLG to screen applied fields due to an STM is essentially identical in our measurements. This fact is attributed to substrate-induced doping of the graphene layers that places the Fermi level in the conduction band in each layer. The measurements presented here provide qualitative insights that will aid in considering possible applications of epitaxial graphene on SiC(0001).

## **5.6 Further Discussion**

We further discuss the implications of our measurements for surface potential mapping in epitaxial graphene in the following Sections. This is conducted by including spectroscopy of the bare interfacial “buffer layer” and compare its spectra to the decoupled graphene layers growing on top. Extended discussion will also be brought upon how image potential states can probe how work functions change by the number of graphene layers on the SiC(0001) surface.

### 5.6.1 Image Potential States of Epitaxial Graphene Interface Layer

The structure of the interfacial layer between SiC and epitaxial graphene is today fairly well understood as a network of  $sp^2$  bonded carbon similar to a true graphene layer. However, strong interaction with the SiC exists through partial hybridization of  $p_z$  orbitals with Si dangling bonds of the SiC(0001) surface. This substrate interaction results in a distortion of the delocalized  $\pi$  bands and completely wash out the linear dispersion around the Fermi level as of a true graphene layer. Analyzing the image potential states of the bare buffer layer can however give us valuable information for the interpretation of high energy unoccupied states spectroscopy of SLG and BLG. Fig 5.5 show  $dz/dV$  spectra acquired on a buffer layer on two different samples. First to mention is that we see similar structure of the image potential states on this surface as for single and bilayer graphene with an intense series of peaks starting with the first member right around 4 eV. We can therefore confidently identify the peak around 4 eV to be the the  $n=-1$  IPS member which corresponds to the  $n=1$  state in a regular single Rydberg series. This peak is shifted in energy by about 0.2 eV from sample A and sample B. Similar to single and bilayer graphene such shifts are observed when the tip state is unintentionally changed during spectra acquiring from the same area, i.e. the spectra in figure 5.5 are collected with two different “tip states”. This observation suggests the buffer layer has at least just as poor ability to screen the electric field induced by the STM tip as SLG and BLG.

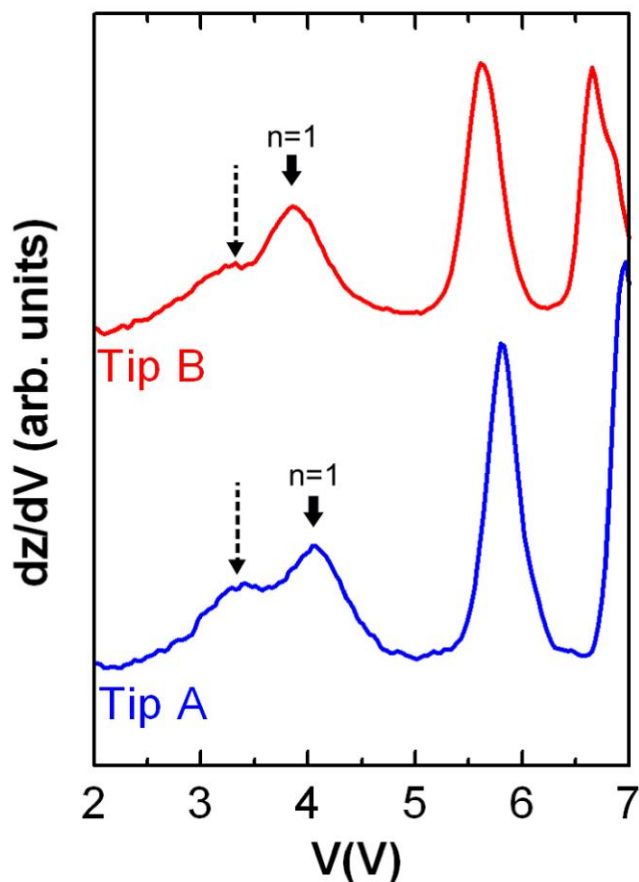


**Figure 5.5** Differentiated constant-current distance-voltage spectra measured for buffer layer at two different samples. Currents; Tip A: 0.2 nA, Tip B: 0.1 nA

No systematic control of the screening could be made at different electric fields (different current set point) due to the inability of exhibit reproducible structure for currents higher than 0.2 nA. However, the screening is predicted to be poor since the  $6\sqrt{3}$  has no states at the Fermi level and manifest semi conducting properties. What is further interesting is that a small peak appears at  $\sim 3.3$  eV, about 0.70 eV below  $n=-1$  IPS (marked with dashed arrow in fig. 5.5). Silkin et al. predicted a double Rydberg series of even and odd symmetry image potential states on perfectly flat graphene that arises from the even symmetry of a single

isolated graphene sheet.<sup>125</sup> Bose et al., later claimed they observed the most strongly bound ( $n=+1$ ) even Rydberg member as a weak peak right around 3.3 eV for both single and bilayer graphene grown on SiC(0001). The predicted energy value of  $n=+1$  was 2.94 eV above the Fermi and Bose et al. suggested a stark shift of this peak to be positioned around 3.3 eV.<sup>127</sup> The lower peak in Figure 5.5 looks identical to the peak Bose et al reported which suggests the buffer layer manifest double Rydberg series as well. The peak tends to be independent on changes of tip geometry and is seen to appear at a rigid energy value. If this is the  $n=+1$  state this observation is not surprising because the predicted wave function for  $n=+1$  in perfect graphene has a maximum located only  $\sim 1.5$  Å from the carbon layer<sup>125</sup> which is substantially closer to the surface than the corresponding maximum for an IPS on a metal surface. A significant stark shift due to trapezoidal distortion of the tunneling junction by the applied field should therefore be less obvious compared to the  $n=-1$  state located further out on the vacuum side.

It will however be hard to argue that the low energy peak in Figure 5.5 is originating from the  $n=+1$  even Rydberg series present in the buffer layer. Though the buffer layer is structurally the same as the SLG it is strongly coupled to the substrate and should therefore completely destroy the even symmetry as for an isolated sheet of graphene. In addition, the buffer layer is not flat but modulated and significantly warped by the underlying SiC substrate. This corrugation itself should result in the loss of the “double” Rydberg series even if the buffer was decoupled from the substrate.

A more convincing explanation for the peak below  $n=1$  is that it arises from a surface state for the buffer layer which was previously reported in IPES experiments at approximately the same energy.<sup>135</sup> This surface state may therefore be observed through single and bilayer graphene for low temperature measurements (4.2 K) as in the report from Bose et al.<sup>127</sup> In this room temperature experiments the peak only weakly observed for SLG but is clearly observed for spectra taken on the bare buffer layer.

The higher energy peak at around 4 eV on the buffer layer is consistent with the usual (Stark shifted) single Rydberg series seen on SLG, BLG and on other surfaces. It is not particularly surprising that the regular image potential states for a carbon rich surface reconstruction are similar to true graphene layers since they all originate from a long range electrostatic potential.

### 5.6.2 Image Potential States and its Correlation to Work Functions

The description of the peaks in our spectra as image-potential-derived states permits a simple interpretation of the origin of differences between buffer layer, SLG and BLG peak positions in terms of work function changes. Small changes in the surface potential barrier are picked up in the Image potential states which make them a sensitive probe of surface electrostatic potential variations across a surface, sometimes loosely describe as “local work function” variations.<sup>123,136, 137</sup> Recent Kelvin Probe Force Microscopy (KPFM) experiments have shown that the contact potential difference (CPD) increases by  $0.135 \pm 0.009$  eV in going from SLG to BLG.<sup>130</sup> PEEM experiments reported on a change in work function of about 0.1 eV.<sup>138</sup> Displayed in figure **Fel! Hittar inte referenskälla..6a** We observe an almost identical

shift of  $0.14 \pm 0.02$  eV for the  $n=1$  peak observed for SLG and BLG grown on 4H- and 6H-SiC(0001). It is important to point out that such shift is measured simultaneously with “identical tip states” on an area coexisting of SLG and BLG. The observed lower energy of the  $n=1$  peak precisely correlates with a differential “n-doping” effect of the SiC substrate on epitaxial graphene. As already mentioned, the n-type SiC(0001) substrate transfers charge to the graphene overlayers, partially occupying the conical conduction band and pulling the Dirac point below the Fermi level. Furthermore, the Dirac point of SLG is known to be located  $\sim 0.13$  eV below that of BLG from photoemission measurements.<sup>114, 139</sup> In other words, due to its proximity to the SiC(0001) surface, SLG is slightly more n-doped than BLG. Consistent contact potential differences, PEEM work function measurements and  $n=1$  shifts in these experiments therefore confirms that the work function change is purely due by different substrate induced doping and that the Vacuum level can be considered as rigid at same energy for both SLG and BLG. The same argument can be extended to the case of work function changes going from buffer layer to SLG. In figure 5.6b the  $n=1$  peak is at essentially the same energy for buffer layer and SLG. The work function is therefore suggested to have the same value for the interfacial buffer layer and the additional first decoupled graphene layer. This implies that the Fermi level is positioned at the same energy for the two surfaces which is supported from other reported experiments. ARPES measurements showed that the occupied bands of buffer layer and SLG are the same except for the single  $\pi$ -band around the Fermi level for SLG.<sup>140</sup>

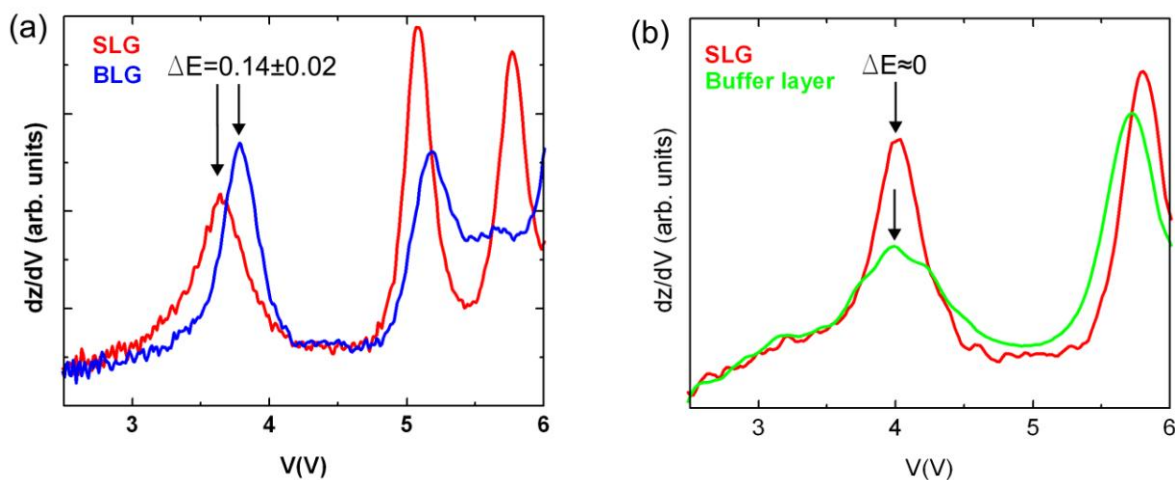


**Figure 5.6** (a) Differentiated constant-current distance-voltage spectra measured with identical tips comparing (a) SLG with BLG and (b) buffer layer with SLG.

Ab initio calculations also supported this and demonstrated that the Fermi level is at the same energy relative to both occupied and unoccupied bands when ignoring the Dirac cone of SLG.<sup>39</sup>

An additional observation of the spectra in figure 5.6b is that the buffer layer  $n=1$  peak is more broad than the corresponding peak of SLG. Same trend can be seen in the comparison of SLG with BLG. This may be an indication of longer life time of image states as the number of graphene layers increases.<sup>110</sup>

## **6: COMBINED THEORETICAL-EXPERIMENTAL STUDY OF IRON PHTHALOCYANINE ON GRAPHENE**

This chapter will cover a combined theoretical and experimental study of paramagnetic molecule Iron Phthalocyanine (FePc) deposited on epitaxial graphene on SiC(0001). The work was done in close collaboration with Dr Marco Buongiorno-Nardelli at the time from the physics department at North Carolina State University and with Dr Arrigo Calzolari at the CNR-NANO Institute of Nanoscience in Italy who performed DFT calculations. Their calculations predict a novel intermixing between graphene  $sp^2$  carbon network and the molecule center metal atom unique for partially filled d-band metal Phthalocyanines such as FePc. This theoretical discovery motivates my experimental study of how FePc molecules order and electronically interact with the epitaxial graphene grown on SiC(0001). Based on the results of this study, such interfaces may serve as possible spin injection channels for future hybrid graphene-organic spin field effect devices.

## 6.1 Abstract

Density functional calculations performed on the paramagnetic molecule Iron-Phthalocyanine (FePc) on graphene predict a novel electronic mixing between molecule Fe metal unoccupied d-band and graphene  $\pi$ -bands. The interaction results in a spin-dependent delocalized hybrid state and is also predicted for multilayer graphene substrates. The crystallographic and electronic structure of monolayer and sub-monolayer FePc films are experimentally studied on graphene grown on SiC(0001) using Scanning Tunneling Microscopy & Spectroscopy (STM & STS) and Low Energy Electron Diffraction (LEED). At monolayer coverage Iron-Phthalocyanine (FePc) form a square, flat-lying and densely-packed structure oriented  $10^\circ$  relative to the graphene principle lattice direction. At sub-monolayer coverage in room temperature, FePc forms a unique 2D molecular gas suggesting small diffusion barrier in the molecular assembly and an enhanced residence time near defects. The gas is almost completely condensed at liquid Nitrogen temperatures. Scanning Tunneling Spectroscopy data suggests the possibility of a hybrid molecule-graphene state in the unoccupied density of both states near the Fermi level.

## 6.2 Introduction to Combined Theoretical-Experimental Study of Iron Phthalocyanine on Graphene

Future solid state nano-devices require low dimensional structures and interfaces that can control both electric charges and individual spins extremely accurately.<sup>141, 142</sup>

To fulfill those requirements attention has been paid to new emerging inter disciplinary technologies such as molecular electronics<sup>143</sup> and spintronics.<sup>144</sup> Promising molecular candidates in those fields are organic molecules like metal-Phthalocyanines (MPc's). These are macrocyclic molecules with a single metal atom in the center bonded to the ligand via nitrogen heteroatoms on the macrocycle. They are structurally stable and can withstand high temperatures in air without decomposing. Because Metal Phthalocyanines also possess versatile optical and semiconducting properties they can be adapted to numerous applications such as dyes, solar cells, and as active channels in field-effect transistors.<sup>145</sup> The flexibility for demanding electronic and magnetic properties can be mainly explained by the possibility of switching out the central atom from various metal atoms with restored the stability and atomic geometry within the molecule.

This makes MPc's tunable individual nanomagnets where each individual intrinsic spin can be controlled depending on the choice of center metal atom.

Adding the possibility that these molecules form stable self assembled monolayers on various surfaces, several studies have attempted to explain how the substrate may influence the molecule. For example, the triplet spin ground state of FePc can be switched from the easy plane of the bulk to the easy axis of the molecule when deposited on an oxidized Cu(110)

surface.<sup>146</sup> In addition, an individual CoPc molecule has shown a remarkable spin-dependent orbital mixing with a ferromagnetic surface.<sup>147, 148</sup> This clearly demonstrates why MPC's are promising candidates for future spintronic devices.

Another essential component in spintronic devices is a material that can carry and preserve spin over long times and long distances. An excellent spin carrier is the novel two dimensional  $sp^2$  carbon material graphene. It can exhibit extraordinarily long spin relaxation times thanks to extremely small spin-orbit coupling.<sup>58</sup> The discovery of this material was recently awarded the Nobel Prize as a result of several remarkable intrinsic properties including huge charge carrier mobilities<sup>16</sup>, mechanical strength<sup>6</sup> and superb thermal conductance<sup>149</sup>.

A graphene-MPc hybrid may therefore serve as core building block in future quantum computing and other operational spintronic components. In fact, Candini et al. recently constructed a graphene- Phthalocyanine device that electrically could detect magnetic flux from individual TbPc<sub>2</sub> molecules.<sup>150</sup> Extraordinary sensitivity in the coulomb blockade regime was demonstrated which could be of value in future high density information storage. There are many fundamental issues that need to be addressed to thoroughly understand the organic-graphene interface to realize graphene-organic hybrid spintronic devices. To date only sparse studies have been reported on this interface. Among those, MPC's were deposited on graphene grown on the metals Ni(111) and Ru(0001).

Graphene grown on these metal surfaces exhibit a Moire pattern due to a lattice mismatch with the metal. Remarkably, a distinct Moire-driven adsorption was found for FePc deposited

on graphene on Ru(0001).<sup>151,152</sup> Mao et al. proved by STM that the FePc molecules nicely replicate the graphene/Ru(0001) Moire in the form of a Kagame' lattice in a flat lying orientation. Zhang et al. also used STM to clearly show coverage dependent adsorption where the FePC molecule picks specific sites in the Moire pattern upon adsorption. The assembly process of molecules on the graphene was described by lateral electrostatic dipoles driving the molecules to specific sites by interacting with the highly polarizable FePc molecule.

Similar Moire driven adsorption was also found for FePc deposited on graphene on Ni(111). LEED data showed that the FePc molecules adsorbs in a way that perfectly matches the Moire pattern resulting in restored reciprocal symmetry.<sup>153</sup> Even though the exact real space structure of the FePc monolayer was not determined on this surface, a flat lying orientation of the molecules was concluded from x-ray absorption near edge structure (NEXAFS).

In another study FePc substrate interaction with graphene/Ni(111) was compared with compounds that have higher d-band filling such as CuPc and ZnPc. It was concluded from high-resolution electron energy loss spectroscopy experiments that the d-band occupation number has prominent effect on the bonding to the substrate.<sup>154</sup>

It is important to point out that in the case of monolayer graphene grown on the metal surfaces Ni(111)<sup>155,156</sup> and Ru(0001)<sup>157, 158</sup> the graphene substrate does *not* have the usual graphene electronic properties such as linear momentum-energy dispersion around the K-point. The interaction between the first carbon layer and the substrate is strong due to hybridization of the graphene  $\pi$  bands with the substrate. Such an interaction may result in

interesting phenomena such as Rashba splitting of surface states but cannot be regarded as ideal substrates to study the pure graphene-Phthalocyanine interaction.

In this paper we report on novel electronic intermixing between FePc and the graphene  $\pi$ -bands that is mediated by the FePc LUMO and localized to the center Iron atom in the molecule. Our calculations from first principles show that this unique hybridization is strongly dependent on spin and only occurs for partial d-band filling in Phthalocyanines. It is present for both single and multilayer graphene. To investigate FePc structures on graphene, we deposit FePc on graphene grown on SiC(0001) and perform STM and LEED. Local density of states of the molecular layers are measured using the STM in single point dI/dV mode. The choice of epitaxial graphene on SiC(0001) as a substrate is justified by the fact that it is one of the most promising industrially-scalable platforms for future graphene based nanoelectronic technology<sup>54</sup> and has been extensively studied in the last decade.<sup>27, 36</sup> In addition, the graphene coupling to the SiC substrate is weak enough that true Dirac cones exist for charge carriers around the Fermi level reminiscent of isolated graphene. Our discovery discussed in this report leads the way to new insights into the role of organic molecules and graphene integration in quantum gates and spin devices.

### 6.3 Methods

Theoretical DFT calculations were performed using the quantum-ESPRESSO software package with the generalized gradient approximation (GGA), the Perdew-Becke-Ernzerhof functional and a correction for dispersion forces [DFT(D)]. Further computational details can be found in ref. [<sup>159</sup>]. In the experiments reported below sample of CMP polished nitrogen

doped single crystal 4H-SiC(0001) crystals (from Cree) were used. These samples were first degreased in acetone for 20 min followed by methanol for 5 min and then dipped in deionized water. The native oxide was removed by dipping samples in 10:1 HF solution for 15 minutes. Final step of ex-situ sample cleaning followed rinse in deionized water and sample drying in a Nitrogen gas flow. After mounting in a UHV chamber the samples were outgassed in UHV for several hours at  $\sim 500$  °C. Mostly single-layer graphene was grown on the SiC surface through Si-sublimation at 1300 °C with some regions of bi-layer graphene. Molecules of FePc were deposited at room temperature using a Knudsen cell shuttered source located in a preparation chamber separated from the main chamber at typical thicknesses that were estimated to be multilayers. In the main chamber samples were annealed in the range of 300-400 °C to desorb multilayers of FePc and achieve monolayer thickness as determined by STM images. STM measurements (Omicron VT-AFM) were acquired at both room temperature and 110 K using either etched tungsten and/or Pt-Ir tips. In addition, we collected  $dI/dV$  spectra using a sinusoidal modulation of frequency 770 Hz and amplitude of 100 meV. We observed ordering using LEED performed with a 4-grid Omicron (model SPECTALEED) with beam energies of no more than 20 eV to avoid rapid beam damaging of molecular films.

## 6.4 Results and Discussion – Theory

We shall start by discussing theoretical results of FePc on graphene which will motivate a thorough experimental investigation of this system. Figure 6.1a shows the calculated spin resolved band structure of FePc on single layer graphene. The linear energy momentum dispersion around the Fermi level (aka Dirac cone) reminiscent of isolated graphene is undisturbed and empty for the spin up sub-bands. For spin down, the situation is remarkably different. Here, a small gap opens at the Dirac point and a new electronic state is present in the gap. This state is a delocalized hybrid graphene-molecule state with density on both the graphene substrate and the central Fe atom of FePc. This state primarily involves the LUMO of the molecule and is displayed in Fig. 6.1b. We further conclude that this FePc/graphene interaction is also valid for multiple graphene sheets (1-4 layers) stacked in a Bernal configuration which suggests that FePc will interact in a similar manner with graphite as it does with graphene. The prediction that the d-band filling factor of the centre metal atom plays a major role in the interaction with graphene for MPC's agrees with recent experimental studies from Dou et al..<sup>154</sup> They showed using HREELS that FePc (d=6) and CoPc (d=7) couples significantly stronger compared to more filled d-band MPC's such as CuPc (d=8) and ZnPc (d=10). To confirm this in theory we repeated the above calculations for CuPc on a sheet of graphene. Indeed our results agree with experiments since the band structure of graphene around the Fermi level is unperturbed for both spin sub-bands as seen in figure 6.1c.

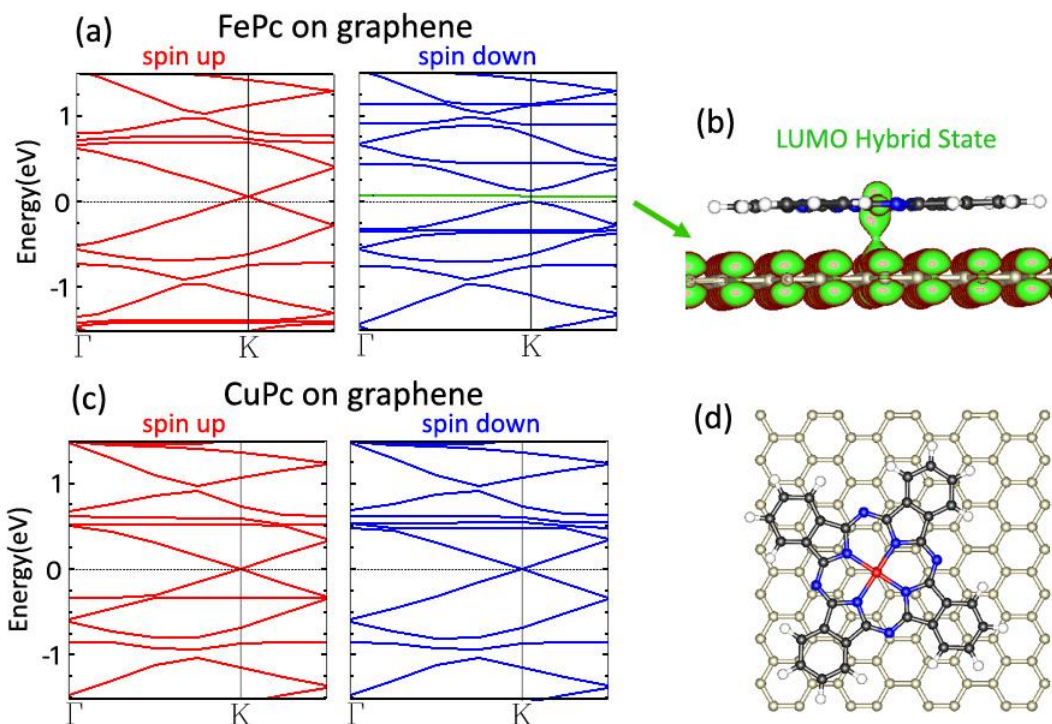


**Figure 6.1** Results of DFT calculations. (a) Individual spin-band structures of FePc on graphene. Dirac cone is intact and empty for spin up while Dirac cone is split and empty for opposite spin. A mixed graphene-molecule state is present at the Fermi level marked in green. (b) side-view of LUMO orbitals originating from mixed graphene-molecule state of spin down. (c) Individual spin bandstructures of CuPc on graphene. (d) Relaxed computational cell of a FePc molecule lying flat in on-top site with a C atom in the graphene. Red=Fe, blue=Nitrogen, black=carbon and white=hydrogen. For calculations with CuPc only the center metal Fe atom is replaced with a Cu atom.

## 6.5 Results and Discussion – Experiments

Our calculations predict a unique electronic mixing of states between FePc and graphene. We further investigate the geometric and electronic structure of the FePc molecules on graphene experimentally by depositing FePc on graphene grown on SiC(0001). We shall especially

study the FePc molecules at monolayer coverage and submonolayer coverage and compare its electronic structure to FePc on graphite using scanning tunneling spectroscopy.

### 6.5.1 Monolayer coverage

Figure 6.2a shows an STM image after the adsorption of a full monolayer of FePc on single layer graphene (SLG) and bilayer graphene (BLG) on SiC(0001). The structure is identical for both SLG and BLG. We further confirm that this structure is also identical to that present for FePc on graphite in agreement with an earlier report.<sup>160</sup> The structure is a standard densely-packed monolayer which has been observed on numerous of other substrates for different kinds of Phthalocyanines.

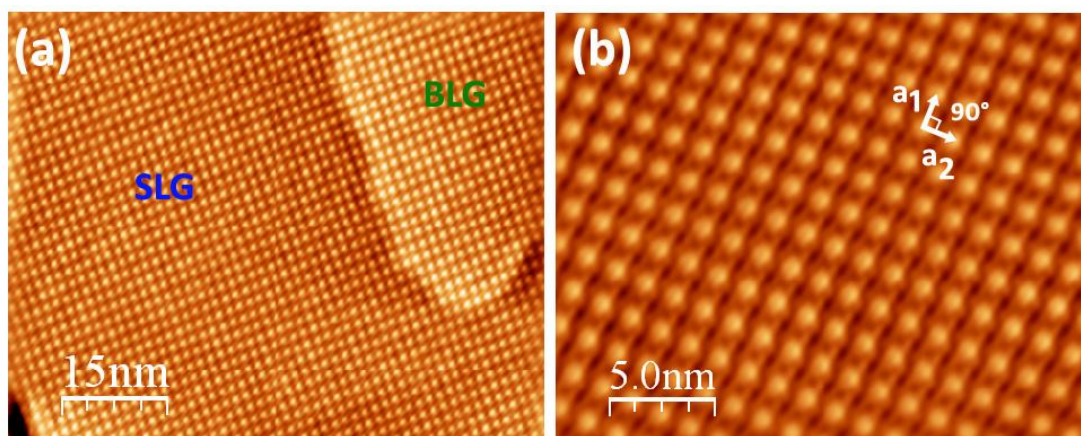


**Figure 6.2** (a) Single domain of square close-packed FePc on both single- and bilayer graphene,  $U=1.5$  V,  $I=50$  pA (b) close-up of a differently oriented square close-packed FePc domain showing the unit vectors  $A$  and  $B$  separated by  $\sim 90^\circ$ ,  $U=1.3$  V,  $I=50$  pA.

Most related to this work is a study by Gopakumar et al. of PdPc on graphite.<sup>161</sup> They report on a close-packed square lattice of PdPc with one of the unit vectors oriented  $\pm (10^\circ \pm 1^\circ)$  from a principle direction of graphite. Since there are 3 principle direction of the graphite

lattice this result in 6 equivalent PdPc domains. For the case of monolayer FePc coverage we observe the identical structure as seen for PdPc on graphite with the unit vectors are  $A=B \approx 1.4$  nm separated with the angle  $90^\circ$  with 6 possible domains coexisting on the surface. To further support our interpretation of the STM images, we collected LEED patterns for both bare graphene and monolayer FePc on graphene at 14 eV electron beam energies. Figure 6.3a shows the bare graphene with 6 spots in hexagonal pattern. These spots are rotated by 30 degrees relative to the graphene first order spots and arise from the fact that the graphene is corrugated in a hexagonal periodicity of SiC(6 $\times$ 6) in the true epitaxial graphene-SiC unit cell of SiC(6 $\sqrt{3}\times 6\sqrt{3}$ )R30 $^\circ$ . Figure 6.3b shows the LEED pattern of monolayer FePc on graphene. Weak substrate hexagonal spots can still be seen along with ring-like pattern induced by the FePc monolayer. This pattern is a superposition in reciprocal space of the six possible real space domains oriented  $10^\circ$  from the graphene principle direction observed in the STM. It is identical to the LEED pattern observed for monolayer PdPc on graphite<sup>161</sup>. Since the unit vector of the SiC(6 $\times$ 6) corrugation is known to be 1.85 nm we extract the real space unit vectors of FePc knowing its lattice is square symmetric from STM imaging. The ratio of reciprocal unit vector SiC(6 $\times$ 6)/FePc is  $1.22 \pm 0.2$  which results in FePc unit vectors of  $\sim 1.35$  nm. With the STM and LEED observation and assuming each molecule is sitting on identical high symmetry points on the graphene the only plausible structure of FePc on graphene is the square lattice shown in figure 6.3c.

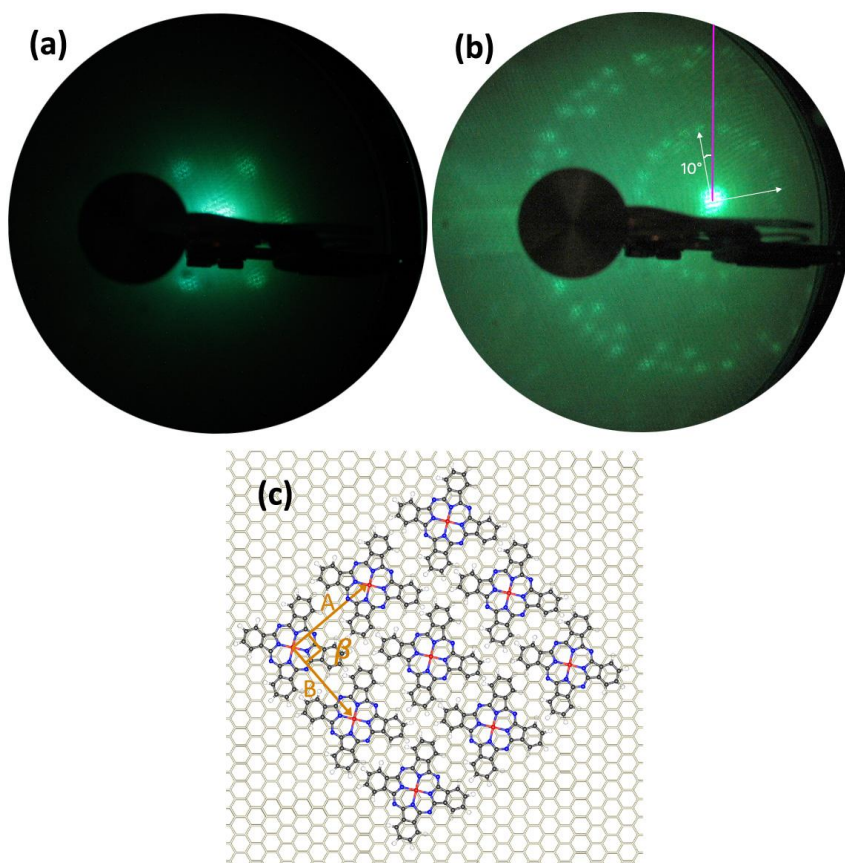


**Figure 6.3** (a) LEED of clean graphene on SiC(0001),  $E=14$  eV. (b) LEED of monolayer FePc on graphene on SiC(0001),  $E=14$  eV. Reciprocal lattice vectors for one out of six identical but differently oriented FePc domains on the graphene marked with white arrows. Purple line shows the direction of a graphene reciprocal lattice vector. (c) Atomic model of the real space FePc lattice on top of the graphene lattice. Unit vectors have magnitude  $A=1.37$  nm,  $B=1.30$  nm both separated by  $90^\circ$ .

Figure 6.3c displays one out of the six possible equivalent domains where unit vector A is 1.37 nm long and rotated 10 degrees from one of the graphene unit vectors. Unit vector B is 1.3 nm long and oriented  $20^\circ$  from the other corresponding graphene unit vector. This proposed model is identical to the model proposed by Gopakumar et al. for PdPc on graphite. This shows that the 2D crystallography of the layer is largely driven by the ordinary Van der

Waals interactions between molecules and with the graphitic substrate and is not strongly influenced by the unusual hybridization predicted by theory.

### 6.5.2 Sub-Monolayer Coverage

As we anneal the sample from full monolayer coverage to even higher temperatures we are able to slowly desorb molecules from the surface as confirmed by a decrease of Nitrogen Auger peak in Auger electron Spectroscopy measurements (not shown here). After heating the sample to 480 °C for 15 minutes and allowing sample to cool down to room temperature STM measurements show dramatic changes. There are no obvious molecular structures visible, instead we can see a weak substrate corrugation and around graphene defects we observe ring-like structures. We can also observe boundaries (fig. 6.4b) of such domains with domains of ordered close-packed FePc molecules (as described above) where the apparent height across the domain boundary is the same. We interpret the unique domain on the right of the image in Figure 6.4b as a “molecular gas” where the molecules rapidly move on the surface at much higher rates than the tip rastering rate. The corrugation seen in this domain in STM represents a map of the average residence time of 2D gas-phase molecules. As molecules quickly move across the surface they may bounce many times off of edges of rigid close packed FePc domains appearing in STM to have the same thickness as the molecule height. We can confirm the dynamic origin of the observed 2D gas domains by significantly lowering the temperature of the surface. Figure 6.4c show the sample in fig. 6.4a at 110 K which is low enough to allow FePc molecules to slow down and condense to locally form

their close-packed square structure. Edges of FePc domains now show an obvious height difference of approximately  $3.5 \text{ \AA}$ , similar to the apparent height of the FePc molecules. While 2D gas phases are known to exist for low surface coverages in some molecular systems,<sup>162</sup> the FePc gas on graphene is unique in appearance in showing relatively smooth, noise free areas with distinct ripples near defects. This structure has not been reported on HOPG, and may be related to small differences in the magnitude of the orbital mixing between FePc and graphene compared to FePc and graphite. Such differences are predicted theoretically in our DFT calculation to be minor but could account for the unusual behavior of the 2D molecular gas of FePc on graphene. In the next section, we describe more direct spectroscopic evidence that the molecule surface mixing interaction is subtly different depending on the number of graphene layers on which FePc adsorbs.

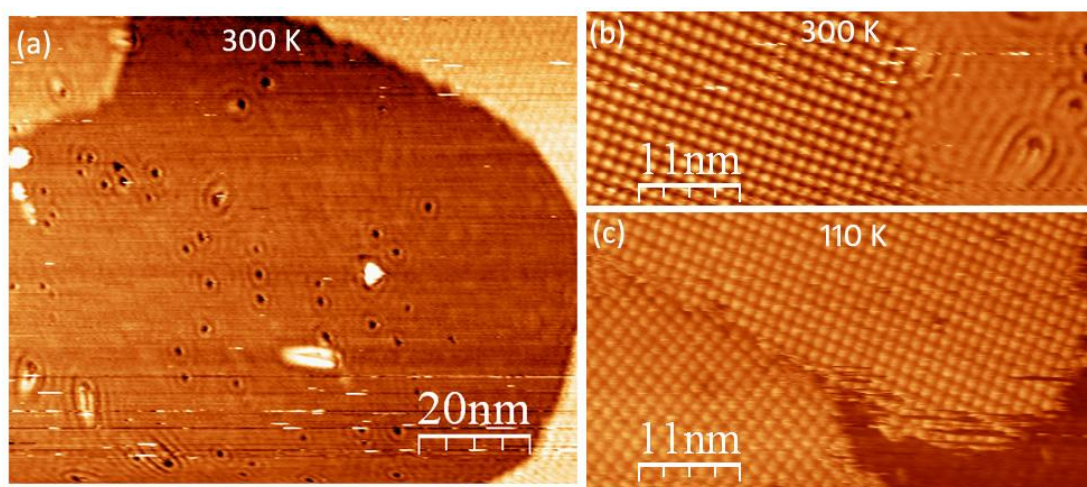


**Figure 6.4** (a) Molecular gas of FePc at sub-monolayer coverage at room temperature. (b) Boundary of ordered FePc(left side) molecules with FePc molecule gas (right side of image). (c) Same coverage as in (a) but at 110 K showing a boundary of close-packed FePc molecules and bare graphene (lower right corner).

### 6.5.3 Tunneling Spectroscopy

Investigation of the electronic structure of close-packed ordered FePc on graphene and graphite is performed using  $dI/dV$  spectroscopy as shown in figure 6.5.

For graphite (blue curve, figure 6.5) the highest occupied molecular orbital (HOMO) onset shows up at around -1.7 eV. This is in good agreement with reported photoemission studies of FePc monolayers on graphite<sup>163</sup> and a similar HOMO onset can also be seen for FePc on graphene (blue curve). The lowest unoccupied molecular orbital (LUMO) appears at about 0.5 eV above the Fermi level for FePc on graphene.

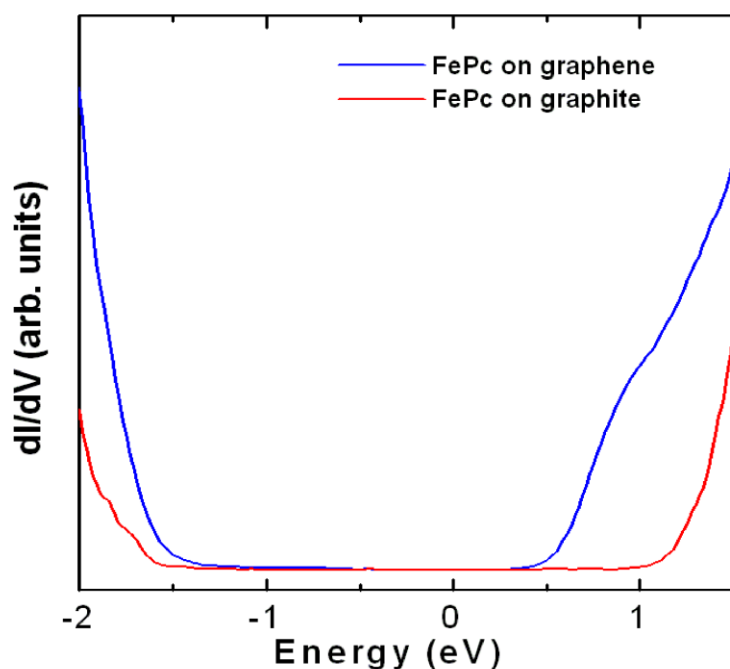


**Figure 6.5**  $dI/dV$  spectroscopy of monolayer FePc on single layer graphene on SiC(0001) (blue curve) on SiC(0001) and monolayer FePc on graphite (red curve).

This LUMO state is within the gap of isolated FePc and is also significantly lower in energy compared to STS studies of the LUMO's of other MPC's.<sup>164</sup>

Most importantly, the LUMO for FePc on graphite shows up at significantly higher energy as an onset at about 1.2 eV above the Fermi level as shown in Figure 6.5. We interpret the abnormally low LUMO energy for FePc on graphene as evidence for the theoretically-predicted unoccupied orbital mixing. Theory also predicts such mixing for FePc on multiple graphene layers that approximate graphite. Since we observe clear electronic differences between the two substrates, we infer that the hybrid state on graphene must extend further into vacuum than its counterpart on graphite. This would allow better coupling to the STM tip and more pronounced features in STS spectra as observed. Further low temperature spin-polarized STM or spin-polarized photoemission measurements may reveal more evidence for the electronic mixing suggested by theory.

## 6.6 Summary

We have reported experimental evidence for a new type of theoretically predicted interaction taking place between the functional organic compound Iron Phthalocyanine and graphene. This interaction is a spin-dependent electronic hybridization arising from unoccupied d-orbitals on the FePc molecule. The adsorption of FePc on graphene was experimentally studied by STM and LEED showing monolayer FePc to prefer flat-lying densely packed square structure oriented  $10^\circ$  from the graphene principle direction. Due to the three-fold and two fold symmetry of graphene and the FePc lattice this results in six differently oriented FePc domains coexisting on the surface. For submonolayer coverage FePc molecules have a

low diffusion barrier which results in the formation of an unusual 2D molecular gas on graphene that was not observed on graphite. This gas allows stable STM imaging of the time-averaged site occupancy of rapidly moving FePc molecules. It suggests subtle differences in molecule-surface interaction between graphene and graphite. Scanning tunneling spectroscopy studies shows further differences in the form of a possible hybrid molecule-graphene state at about 0.5 eV above the Fermi level. These results suggest that molecular functionalization of graphene should be considered as a promising route toward optimizing graphene-based spintronic device applications.

## **7: MULTIPLE COEXISTING INTERCALATION STRUCTURES OF SODIUM IN EPITAXIAL GRAPHENE- SiC INTERFACES**

In this chapter, Intercalation of Sodium in epitaxial graphene on SiC(0001) will be discussed. This work was done in close collaboration with post-doctorial theorist Thushari Jayasekera in the group of Professor Marco Buongiorno-Nardelli here at North Carolina State University and is based on a paper which was recently published in Physical Review B.

Intercalation of graphene is one of the fastest emerging sub-fields of epitaxial graphene at the moment because of the fascinating possibilities of manipulating the interface between SiC and graphene both structurally and electronically. Particularly, by insertion of foreign atomic species at the interface a decoupling the buffer layer can be realized which results in a transformation of this layer into a true graphene layer positioned right over the bulk terminated SiC substrate. The work here involves both experimental and theoretical results and emphasizes several novel aspects listed below.

It is the first report on real space imaging of various intercalation structures that can exist for epitaxial graphene on SiC(0001). Since we have two different interfaces for the epitaxial graphene: The SiC-buffer layer interface and the buffer layer-graphene interface, intercalation is likely to occur at both these interfaces which may render coexisting domains across the surface. This possible spatial inhomogeneity of intercalation structures needs careful consideration and precaution especially since a large portion of graphene intercalation

studies up to date have been conducted with spatially averaging techniques such as angle resolved photoemission spectroscopy (ARPES).

The paper is also important because it proves that the decoupling of the buffer layer is actually allowed both in theory and experiments.

A final important aspect to consider is how graphene intercalation studies can benefit and be compared to the well known graphite intercalation compounds (GIC's). The GIC of alkali metals has been studied for decades where all alkalis form intercalation compounds except for just Sodium. That makes Sodium rather unique in this sense and motivates this study on how Sodium will interact differently with graphene. In fact, the paper shows that Sodium intercalates graphene readily even at room temperature and gives an excellent example of how fundamentally different and versatile the intercalation is in graphene compared to intercalation in graphite.

## 7.1 Abstract

We show using scanning tunneling microscopy, spectroscopy, and *ab initio* calculations that two intercalation structures coexist for Na in epitaxial graphene on SiC(0001). Intercalation takes place at room temperature and Na electron-dopes the graphene. It inserts in-between single-layer graphene and the interfacial layer and also penetrates beneath the interfacial layer and decouples it to form a second graphene layer. Decoupling is accelerated by annealing and is verified by Na deposition onto the interface layer combined with computational modeling of the two new decoupled buffer layer structures.

## 7.2 Introduction to Multiple Coexisting Intercalation Structures of Sodium in Epitaxial Graphene-SiC Interfaces

Graphene is the most promising electronic material to be discovered in the past decade.<sup>115</sup> Its high carrier mobility and chemical and mechanical robustness suggest important applications in electronics that have already started to be realized in prototype devices.<sup>165</sup> A crucial goal in ongoing graphene research is to find ways to control its physical properties by chemical doping.

One strategy for controlling the physical properties of graphene has been adapted from the field of graphite intercalation compounds.<sup>166</sup> It is possible to insert impurity atoms in between sheets of graphite, where they become chemically bound. The most striking example is calcium intercalation in graphite which results in a superconducting solid ( $\text{CaC}_6$ ) with a transition temperature of above 11 K.<sup>167</sup> Unfortunately, intercalation processes in

graphite are often inhibited by slow kinetics.<sup>168, 169</sup> Intercalation beneath *graphene* may be more efficient since intercalating species have only to be inserted beneath a single layer or perhaps a few atomic layers.

Several atomic species have been intercalated beneath epitaxial graphene grown on both SiC(0001) and metallic substrates. On the Si terminated SiC(0001) surface, graphene is allowed to grow nearly decoupled from substrate supported by an interfacial carbon rich layer (aka “buffer layer”) that can be seen as a covalently bonded graphene-like sheet<sup>170</sup> with a large bandgap and vanished Dirac cone band structure<sup>37</sup>. Recent studies<sup>92, 171, 172</sup> demonstrated that this buffer layer could be “activated” by intercalation of hydrogen atoms at high temperatures. Hydrogen intercalation breaks covalent bonds between the buffer layer and the SiC substrate to transform this interfacial layer into a purely  $sp^2$  bonded sheet of graphene.

Other experimental studies have demonstrated intercalation structures for oxygen<sup>173</sup> and for compounds that can alternate the carrier concentration in the graphene. Fluorine intercalation gives p-doped graphene<sup>174</sup> versus n-doped graphene from alkali metal (Li) intercalation.<sup>175,</sup><sup>176</sup> Gold intercalation beneath single layer graphene on SiC(0001) was reported to p-dope the graphene layer.<sup>177, 178</sup> Theoretical studies demonstrated that modifications in the chemical composition of the buffer can lead to significant changes of the graphene bands, allowing for a fine tuning of the electronic structure of the system with band offsets up to 1.5 eV and even induce magnetism of the graphene.<sup>179</sup>

Alkali metal adsorption on graphene has been used extensively to study the effects of electron doping. Potassium deposition on graphene on SiC(0001) has enabled detailed studies of quasiparticles<sup>180</sup> and the discovery of plasmarons<sup>181</sup> in graphene. The additional dipole field from adsorbed potassium can also act to break the sublattice symmetry in graphene to induce bandgap opening.<sup>112</sup> Doping induced by intercalation in graphene may be more significant and could enable studies of correlated electron phenomena such as superconductivity or ferromagnetism in graphene due to the presence of extended van Hove singularities.<sup>182</sup> The intercalation of Ca was reported by McChesney et al. to result in electron doping of epitaxial graphene on SiC(0001) that moved the Dirac point an additional  $\sim 0.5$  eV below the Fermi level.<sup>182</sup>

The most prominent studies of doping induced by intercalation have been carried out using angle-resolved photoemission spectroscopy (ARPES). Since this technique samples a macroscopic area of the sample, it may average over spatially inhomogeneous structures with different electronic properties. The purpose of this letter is to report on the coexistence of two distinct intercalation structures of Na at interfaces in the epitaxial graphene on SiC(0001) system. We describe scanning tunneling microscope (STM) studies of the intercalation of sodium in epitaxial graphene on SiC(0001) at room temperature and the effects of subsequent annealing on the intercalation structures. Sodium atoms form complex spatially-inhomogeneous structures that include intercalation directly underneath single layer graphene (SLG) and intercalation beneath the carbon-rich interfacial “buffer layer”. The location of Na in these intercalation structures and its impact on electronic structure (in particular buffer

layer decoupling<sup>92</sup>) has been modeled with *ab initio* density functional theory (DFT) calculations.

Electron doping effects in each new intercalation structure are inferred from the scanning tunneling spectroscopy (STS) study of image potential-derived surface states (IPS's). These states arise outside of a surface due to polarization of surface charge<sup>122</sup> and have recently been connected with the formation of interlayer states in graphite<sup>127, 183</sup> and used to understand screening and doping effects in epitaxial graphene in SiC(0001).<sup>184</sup> Changes in work function due to doping are often visible as corresponding shifts in the energy of IPS's<sup>136</sup> and demonstrate doping effects in sodium intercalated epitaxial graphene. Most importantly, STS results have been connected with work function changes calculated from first principles that unambiguously distinguish the different locations of Na in the intercalation structures.

### 7.3 Experimental Methods

The SiC samples used in this study were chemical-mechanical polished (NovaSiC) 4H-SiC(0001) wafers. They were cleaned *ex situ* with acetone, methanol, and HF before introduction to an ultrahigh vacuum (UHV) system (Omicron). Using direct current heating the samples were annealed in UHV (base pressure  $\sim 2 \times 10^{-11}$  torr) to 1300 °C for 3 minutes to grow graphene. Surfaces prepared in this way typically show primarily single layer graphene with small domains ( $\sim 10$ -20% surface coverage) of bilayer graphene. Different layers can be easily distinguished by the reduction in substrate-induced corrugation in the bilayer and by the systematic energy differences in image-potential derived surface states in STS.<sup>184</sup>

By choosing a lower annealing temperature (1000 °C for 10 minutes) of the SiC substrate we can prepare a surface that consists of mainly bare buffer layer coexisting with small domains of single layer graphene as confirmed by STM imaging, low energy electron diffraction, and analysis of the shape of C KLL Auger peaks.

The samples were allowed to cool for several hours to approximately room temperature. Sodium was then deposited from an outgassed getter source (SAES). STM images were measured using a commercial instrument (Omicron) in constant current mode at room temperature with electrochemically-etched tungsten tips. Annealing experiments after sodium deposition were carried out using a calibrated tungsten heater in the sample manipulator and are expected to be accurate to about 20 °C. Scanning tunneling spectroscopy was performed in distance-versus-voltage (“z(V)”) mode with constant current feedback engaged. The junction voltage is swept in a positive large bias interval where high local density of states is observed as an increased rate of tip retraction.<sup>81</sup> This measurement is the most useful form of STS for studying high energy IPS’s, where normal STS in constant height mode leads to high currents and tip instability.

## 7.4 Computational Methods

Theoretical calculations were carried out using plane-wave, pseudopotential, DFT as implemented in the quantum-ESPRESSO software package<sup>185</sup> with the generalized gradient approximation (GGA) and the Perdew-Becke-Ernzerhof functional and a correction for dispersion forces (DFT(D)). Other computational details are the same as in Ref<sup>179</sup>. All calculations include 1 Na atom per 8 graphene carbon atoms in a computational unit cell that

includes a carbon rich buffer layer strongly bonded to the SiC surface but leaving several unsaturated dangling bonds.<sup>179</sup>

## 7.5 Results and Discussion

At low coverages, sodium exposure on SLG results in the appearance of linear chains on the surface following the 3-fold symmetric directions of the SiC substrate as shown in Figure 7.1a. In Figure 7.1b, at higher submonolayer coverage, the chains become more densely packed and coalesce into islands which have the same  $6\times 6$  corrugation as the bare single layer graphene (Figure 7.1c). The STM images in Figure 7.1d clearly show these domains to be covered with a honeycomb graphene lattice. We infer that sodium is intercalated in between the buffer layer and the graphene layer. We abbreviate the compact domain in Figure 7.1c as SiC/B/Na/G where B stands for buffer layer and G for graphene layer. Judging from the apparent height and continuity of this intercalation structure, the islands are locally the same (e.g. SiC/B/Na/G) as the chains. A recent DFT study supports the idea that Na intercalation between the buffer layer graphene is preferred over Na adsorption on top of the graphene layer.<sup>186</sup> Sodium atoms completely avoid domains of bilayer graphene (BLG, marked in Fig. 7.1b). Our experimental observation of intercalation in epitaxial single layer graphene is unexpected since Na does *not* form intercalation compounds on graphite<sup>168</sup> without help from catalytic impurities.<sup>108</sup> The detailed mechanism of this process is a significant open question.

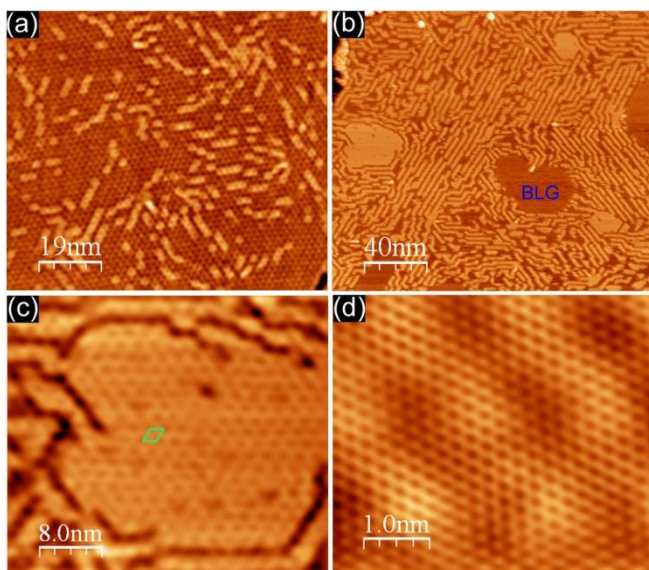


**Figure 7.1** STM images of Na intercalated between buffer and graphene layer, SiC/B/Na/G. (a) Low coverage Na chains ( $V=-2.18$  V, 62 pA); (b) Intermediate coverage with chains and islands. ( $V=-2.0$  V,  $I=50$  pA); (c) Na island in figure b with (6x6) quasi-cell indicated ( $V=-2.3$  V,  $I=50$  pA); Graphene lattice of island in figure c ( $V=-0.55$  V,  $I=350$  pA).

An additional intercalation structure coexists with SiC/B/Na/G after exposing epitaxial graphene to Na as illustrated in Figure 7.2a-7.2c. It exists in small domains immediately after deposition of Na at room temperature, but dominates the surface by heating of the sample after Na deposition. Figure 7.2a shows an area of a sample that has been annealed to approximately 180 °C that is now strikingly different from the SiC/B/Na/G layers in Figure 7.1. It exhibits a flat morphology with no sign of periodic 6×6 corrugation from the substrate. Instead, domains have randomly-distributed depressions and line defects. Figure 7.2b directly demonstrates the comparison between this surface and bare SLG and BLG. The vanishing corrugation from the substrate is reminiscent of recent STM observations of hydrogen-exposed graphene on SiC where the hydrogen has intercalated at the SiC-buffer layer,

decoupling the buffer layer to create a second graphene layer.<sup>172</sup> Figure 7.2c shows a close up of an intercalated domain after annealing of the sample where it is apparent that the surface is covered graphene but now with a triangular symmetry of the graphene honeycomb. This is strong evidence that we now have two layers of graphene sheets that are stacked in regular Bernal stacking (AB).

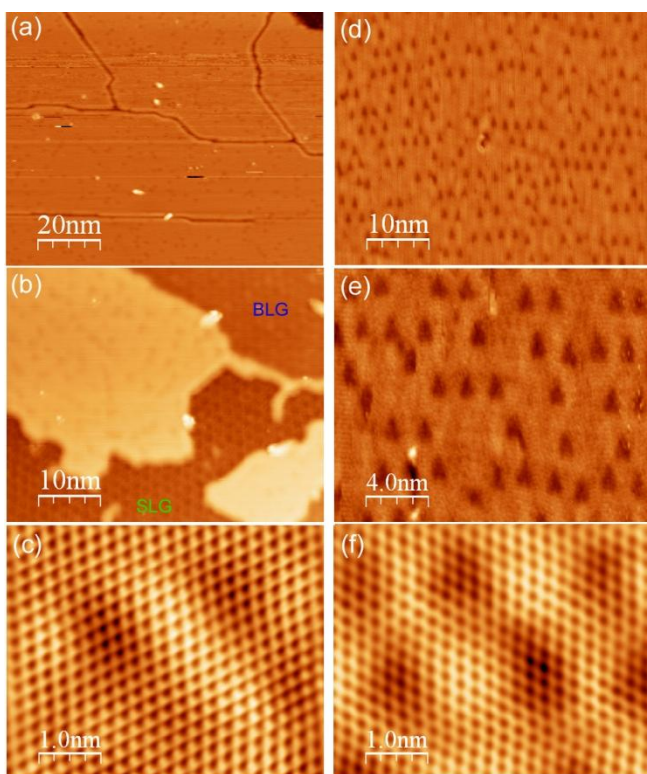


**Figure 7.2** STM images of Na intercalated at SiC interface after heating of sample: SiC/Na/G/G (a)-(c) and SiC/Na/G (d)-(f); (a)  $\sim 180$  °C with full coverage SiC/Na/G/G ( $V=-1.93$  V,  $I=200$  pA); (b)  $\sim 530$  °C showing an area of coexisting SLG, BLG, and SiC/Na/G/G ( $V=-1.7$  V,  $I=50$  pA); (c) Graphene lattice on SiC/Na/G/G ( $V=-0.37$  V,  $I=150$  pA); (d)  $\sim 180$  °C with full coverage SiC/Na/G ( $V=-2.6$  V,  $I=50$  pA), (e) Triangular depressions covering SiC/Na/G surface ( $V=-1.8$  V,  $I=50$  pA); (f) Graphene lattice on SiC/Na/G ( $V=-0.14$  V,  $I=0.11$  nA).

We therefore conclude that the sodium has penetrated beneath the buffer layer and converted it into a second graphene layer just like the case for lithium,<sup>175, 176</sup> hydrogen,<sup>92, 171, 172</sup> oxygen,<sup>173</sup> and fluorine<sup>174</sup> intercalation. We abbreviate this intercalation structure SiC/Na/G/G.

To directly verify that the buffer layer can convert to a second graphene layer due to Na intercalation, we repeated the measurement with a surface prepared to consist of bare buffer layer. Images in Figures 7.2d-7.2f show such a surface after Na deposition and annealing to  $\sim 180$  °C. The sodium has intercalated at the buffer layer-SiC interface across the whole surface. We label this geometry as SiC/Na/G. Its surface morphology is similar to the previously described structure SiC/Na/G/G where the  $6\times 6$  surface corrugation has vanished. The STM image in Figure 7.2e proves that the buffer layer is decoupled since the graphene honeycomb lattice is clearly visible.

To further characterize the three intercalated structures, we measured their IPS's using STS and compared them to a fixed energy reference on the  $n=1$  IPS of SLG as described below. Our expectation is that the variation in energy of these states between different intercalation structures will reflect variations in the Na doping-induced changes in work function compared to SLG.<sup>136</sup> Figure 7.3 displays differentiated distance-voltage ( $dz/dV$ ) spectra for intercalated structures relative to SLG (red curve, with single  $n=1$  IPS peak defined as 0 eV) where the peak corresponds to the first member of the (odd<sup>183</sup>) Rydberg series that we refer to as  $n=1$ . Since the  $n=1$  peak position of epitaxial graphene is sensitive to different tip states due to poor screening in the graphene sheet,<sup>184</sup> it is important to keep track of the tip state.

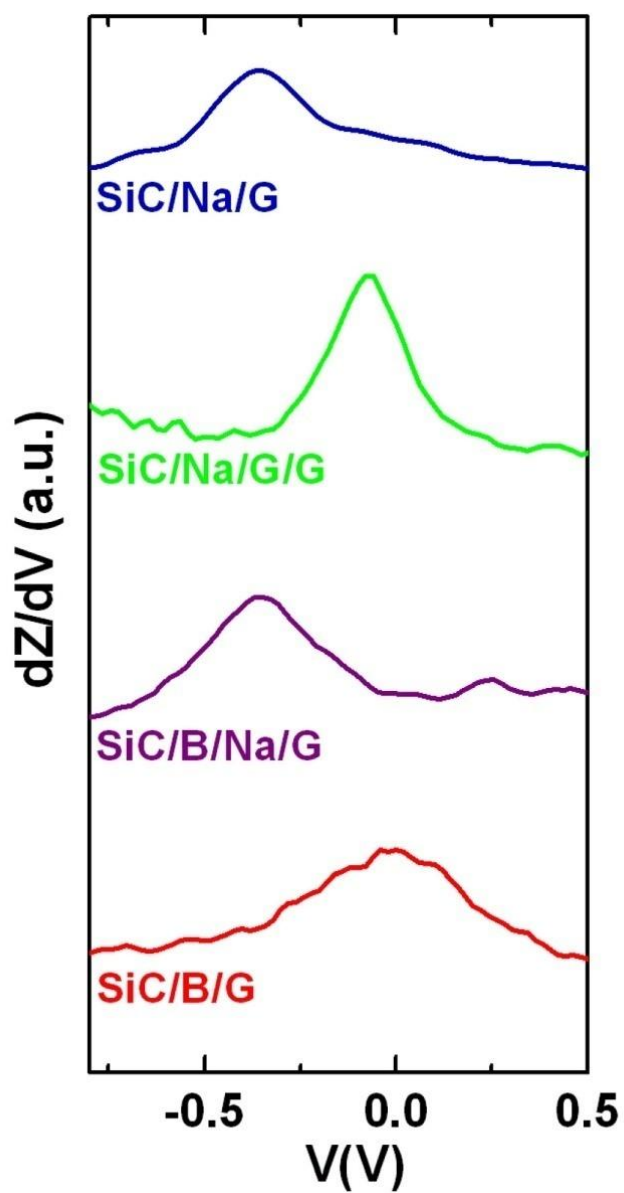


**Figure 7.3** Differentiated ( $dz/dV$ ) distance-voltage spectra  $z(v)$  of the  $n=1$  IPS for different intercalation structures relative to the  $n=1$  IPS on SLG (red). All spectra are recorded with a constant current set-point of 50 pA.

We collected the STS data for intercalation structures SiC/Na/G, SiC/Na/G/G and SLG simultaneously (i.e. with the same tip state) for use as an internal reference (in contrast to usual STS studies where the substrate Fermi level is the most useful reference).

Intercalation structure SiC/B/Na/G was measured simultaneously with BLG and referenced to SLG using the known  $0.14 \pm 0.02$  eV difference in IPS energy between these two.<sup>184</sup>

For SiC/B/Na/G, the  $n=1$  state is shifted down (purple curve) compared to bare SLG on SiC(0001). This shift can be attributed to a lowering of the work function as sodium electron-dopes the graphene through charge transfer.

For SiC/Na/G/G, the  $n=1$  IPS is shifted up again and is slightly lower in energy compared to SLG (green curve). This reversal in direction of work function can be explained by the hypothesis that Na atoms penetrate beneath the buffer layer so that their doping of both layers appears reduced compared to when sodium sits between buffer and graphene layer. This is analogous to the differences in substrate-induced doping between single layer and bilayer epitaxial graphene on SiC(0001).<sup>187</sup> For SiC/Na/G (blue curve) the downshift in  $n=1$  IPS implies that electron doping is increased and work function decreased in a similar manner to SiC/B/Na/G. This similarity is expected since both these structures have Na intercalated directly under one graphene sheet.

Our interpretation of the location of intercalated Na atoms and associated electron doping effects of the three different intercalation structures can be substantiated using first principles electronic structure calculations. Figure 7.4 displays theoretical band structures for SLG (Figure 7.4a) along with SiC/B/Na/G (Figure 7.4b), SiC/Na/G/G (4c) and SiC/Na/G (4d). For

SLG, Si dangling bonds at the SiC- buffer layer interface are responsible for a charge transfer which induces a shift of the Dirac Point to 0.49 eV below the Fermi level (red dashed line in Figure 7.4). For SiC/B/Na/G the Dirac point is shifted down further to 1.09 eV below Fermi level. This is consistent with an earlier calculation made for a similar geometry that first predicted the stability of SiC/B/Na/G compared to Na adsorbed on top of graphene.<sup>186</sup> In addition, the shift is similar in size to the shift of the Dirac point reported for Ca intercalation by McChesney et al.<sup>182</sup> It would be of great interest to extend our calculations to consider the possibility of spin polarized band structure similar to the calculations for Mn in Ref. [17]. Our DFT calculations for SiC/Na/G/G shown in Figure 7.4c prove theoretically that the Na atoms between the buffer layer and SiC surface decouple the buffer layer. Such a decoupling has been addressed theoretically for the case of H intercalation beneath epitaxial graphene on SiC<sup>188</sup>, but not for the case of alkali metal atoms. This growing body of both theoretical understanding and experimental observations suggests that such decoupling is likely to be a routine feature of intercalation processes on SiC. The electron doping for the AB stacked graphene layers that remain after buffer layer decoupling to make SiC/Na/G/G is reduced compared to SiC/B/Na/G and a 0.29 eV gap opens around the Dirac point with mid gap located 0.65 eV below the Fermi level. For SiC/Na/G (Figure 7.4d), doping from intercalated Na results in a downshift of its Dirac point to 0.99 eV below the Fermi level.

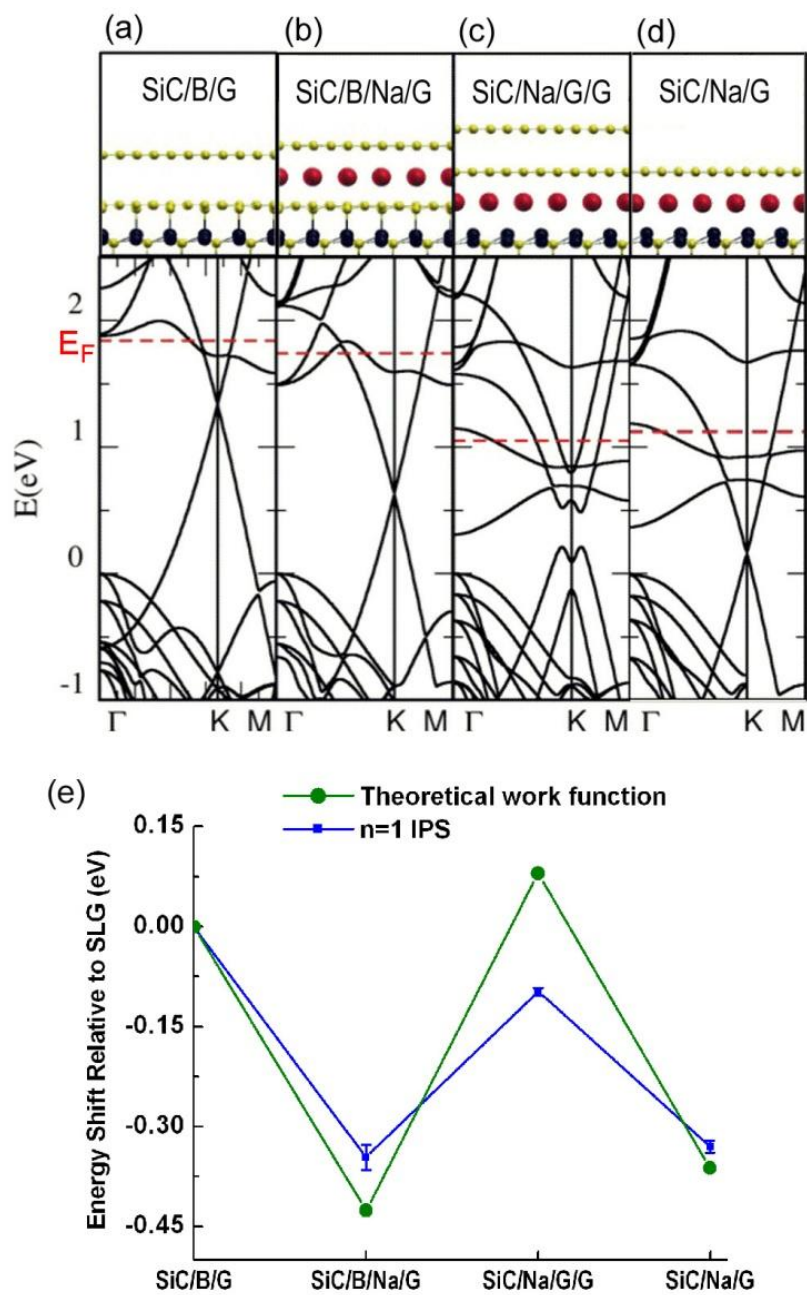


**Figure 7.4** Calculated electronic bands- and atomic structures for (a) SLG on top of SiC(0001); (b) SiC/B/Na/G (c) SiC/Na/G/G (Layers are AB-stacked); and (d) SiC/Na/G. Yellow atoms are C, black are Si, and red are Na. (e) Shift in measured  $n=1$  IPS energy (blue squares) and shift in calculated work function from SLG (green circles) for each intercalation structure.

Importantly, the linear band structure around the Dirac point is maintained in this isolated, activated buffer, indicating that it is a true graphene sheet in accordance with the direct STM imaging in Figure 7.3f.

To compare IPS energy shifts with theory we used the results of *ab initio* calculations to extract work functions for each structure. Image 4e displays IPS n=1 position and calculated work function shift relative to the reference point of SLG. The trend of the calculated work function changes agrees with the STS measurements of the change in n=1 IPS peak position. The most important correspondence from the comparison in Figure 7.4e is the reversal in direction of work function change in going from SiC/B/Na/G to SiC/Na/G/G intercalation. This verifies the hypothesis that heating of the sample initiates Na atom intercalation *beneath* the buffer layer and not in direct contact with the upper graphene layer.

## 7.6 Summary and Conclusions

In summary, we observed the intercalation of sodium deposited on single layer graphene grown on SiC(0001). Contrary to graphite, sodium intercalates readily at the surface at room temperature and forms two different structures. At first, the sodium goes in between the top single graphene layer and the carbon buffer layer. Over time, or with annealing, sodium penetrates through the buffer layer converting this into a second graphene layer. Buffer layer decoupling by intercalation is directly observed by deposition of Na onto bare buffer layer followed by annealing.

First principles DFT calculations directly show the electronic structure and work function trends for these structures. The later compare favorably with measured shifts in IPS energies.

These observations point out the rich possibilities for tailoring electronic structure by intercalation of graphene. The very strong electron doping reported here for Na intercalation could be valuable in the further exploration of superconductivity and magnetism in graphene.<sup>182</sup> Moreover, the efficiency of the intercalation processes identified for Na suggests that intercalation of epitaxial graphene may be an even more versatile strategy for functional modification than it is for graphite since Na does not intercalate graphite. Importantly, the diversity of structures that we have observed as well as their co-existence with one another must be carefully considered in order to correctly interpret spatially-averaging experiments on intercalated graphene.

## 7.7 Further Discussion

This study shows an example of how intercalation in epitaxial graphene can open up new possibilities for graphene electronics by controlling and manage charge carriers and substrate interfacial atomic structures. Despite remarkable capabilities for nano engineering and manipulating of carbon structures on SiC, it is a research field only in its infancy and needs more careful and thorough research before being applicable in functioning devices. In contrast, intercalation compounds in graphite that has been carried out for decades and is well understood especially in terms of the actual atomic structure. Graphite intercalation structures (GIS's) are non-stoichiometric meaning they can vary in actual composition for in-plane ordering but can also vary intraplanar with occupation periodically arranged in a matrix of graphite layers. This staging phenomena has led to classification of GIC's by a stage index  $n$  denoting the number of graphite layers between adjacent intercalate layers.<sup>166</sup> Because of

the two dimensionality of graphene, only the atomic structure of intercalants between the graphene and its substrate is of interest but that does not necessarily means it may an easy task to determine. For the case of this study of Sodium intercalation in epitaxial graphene there is no distinct super lattice seen in neither STM nor LEED to give some clue to accurately determine the sodium coverage. A semi quantitative analysis could be made by Auger electron spectroscopy but since this technique is spatial averaging and the fact that the sodium atoms are positioned underneath graphene makes the analysis unusually complicated. Instead X-ray experiments are more suitable for revealing the in-plane atomic structure of graphene intercalation structures which has been extensively used for for GIC's composition characterization.<sup>166</sup> Transmission electron microscopy could also be used to give a real space picture of the interfacial structure of Na bounded between the graphene and the SiC substrate.

There are several other observations in this study that deserve more attention and additional discussion which will be discussed below.

### **7.7.1 Dynamics of Intercalation**

The first thing that the reader may wonder upon reading the paper is how it is possible for foreign atoms as large as sodium to penetrate through a graphene layer or the buffer layer, even at as low as room temperatures. It has been demonstrated both experimentally<sup>189</sup> and in theory<sup>190</sup> that graphene sheets are completely impermeable to gases including helium. The detailed dynamics of alkali atom penetration in this case is beyond our capabilities to explore concerning the experimental methods used and we can only speculate possible outcomes by

studying the final intercalation structures. Theoretical reports have tried to propose possible mechanisms for this in the case for Li intercalation in carbon nanotubes<sup>191</sup> and buffer layer<sup>192</sup> structure. The main conclusion from these studies is again that penetration is essentially impossible through a perfect hexagon carbon lattice simply because of the size confinement. As an example, Li et al.<sup>192</sup> found that the rate coefficient for Li through perfect buffer layer was  $10^{-13}$  per second at a temperature as high as 600 °C. Instead the, intercalation may be described as purely defect mediated through topological ring-like nonhexagonal defects in the carbon lattice such as heptagons and octagons. As seen in our graphene samples such defects are not present from several high resolution STM investigations. Only defects appearing as elongated and point protrusions which can be explained by local bending of the graphene named nanotube, carbon vacancies or Si atoms substituted into the graphene lattice.<sup>193</sup>

By looking at figure 7.1b and 7.1c the sodium can be seen to nucleate in the structure (SiC/B/Na/G) across the whole surface with coverage density much larger than initial defects that can be observed for *in situ* grown graphene. Hence, permanent graphene defects created upon the growth can not be responsible for Sodium being able to diffuse through the graphene. Instead the sodium atom themselves must induce a temporary defect that can locally induce intercalation. Such process can in fact be possible upon charge transfer to the graphene. Carlsson and Scheffler reported on a reduction of formation energies for graphene defects as the graphene is doped.<sup>194</sup> Since Na strongly n-dopes the graphene by donation of

the lonely valence electron such explanation is plausible for alkali intercalation in epitaxial graphene on SiC(0001).

### 7.7.2 Selective Intercalation of Na on Single Layer Graphene

As briefly mention, sodium is completely avoiding areas of bilayer across the surface. Hence the Sodium atoms are as they adsorb on the surface, quickly diffusing of the bilayer domains until they reach single layer graphene domains where they intercalate at room temperature.

There are two reasonable explanations for this process when Na selectively intercalates single layer graphene and not bilayer graphene.

Firstly, as Sodium does not intercalate graphite it suggests that Sodium is not actually stable in between adjacent AB-stacked graphene layers as in graphite or as bilayer grown on SiC(0001). The size of the sodium atoms should not be an obstacle for intercalation in between multiple graphene sheets since this has been demonstrated earlier with an even bigger alkali metal, rubidium, which intercalates multilayer graphene grown on SiC(0001).<sup>195</sup>

A  $2 \times 2$  periodicity of rubidium is formed in multilayer graphene on SiC(0001) in agreement with  $C_8Rb$  first stage intercalation compound, very familiar in pyrolytic graphite.<sup>196</sup> In the literature there is now clear explanation for why Sodium does not intercalate multilayer graphene. The charge transfer interaction with graphite seems strongly inhibited and even no ordered overlayer can be observed by LEED at temperatures as low as 100 K.<sup>197</sup> STM experiments later found that Na grows layer by layer in (110)-oriented islands on top of the graphite at temperatures below 90 K.<sup>198</sup>

The second reason why Sodium are avoiding bilayer graphene can be drawn from a surface kinetics point of view meaning that the sodium atoms have a higher diffusion rate on bilayer compared to single layer. This can be explained by the fact that bilayer has a smaller interface induced corrugation compared to single layer graphene by being positioned further away from the SiC interface. On the other hand a single layer graphene is less corrugated compared to the buffer layer. If kinetics has an impact in the adsorption Sodium should then avoid single layer graphene if deposited on a buffer layer/SLG surface. Figure 7.5 demonstrates this is in fact the case. Figure 7.5a displays Na deposited at sub monolayer coverage on a surface with mainly buffer layer and small domains of single layer (SLG).

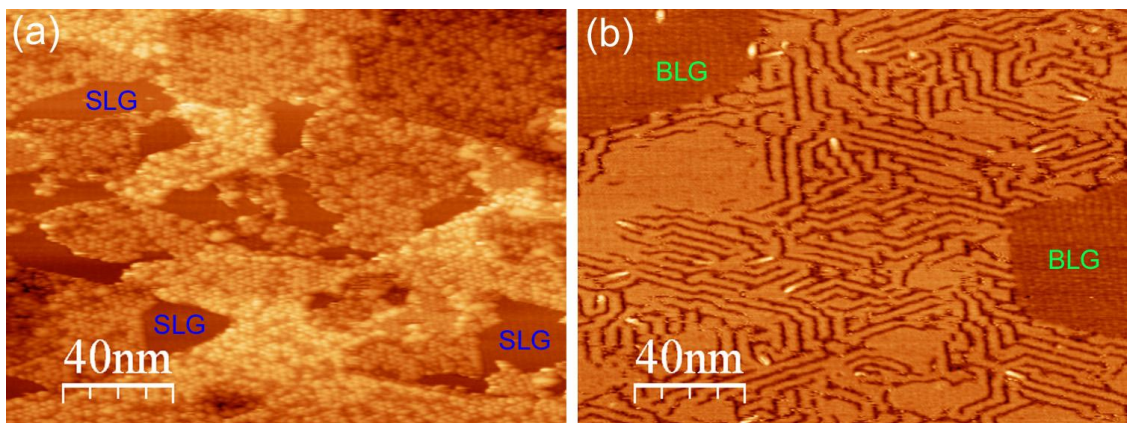


**Figure 7.5** (a) Submonolayer Na deposited on buffer layer where the sodium avoids small domains of coexisting single layer graphene. For clarity some SLG domains are marked SLG in blue color. (b) Submonolayer deposition of Na single layer graphene while avoiding small domains of coexisting bilayer graphene. Bilayer domains marked as BLG in green text.

Surprisingly the SLG domains are clean from Na and the buffer layer are covered with sodium in a  $6 \times 6$  super lattice. For comparison figure 7.5b shows submonolayer coverage of Na only present on SLG domains while completely avoiding the bilayer domains.

### 7.7.3 Triangular Defect Structure of Decoupled Buffer Layer

A characteristic feature of the decoupled buffer layer structure (SiC/Na/G) is the defects with distinct triangular shape shown in figure 7.3d and 7.3e. These are only present on this intercalation structure and can be explained by specific type of atomic structures present at the high symmetry points at the SiC-buffer layer interface. They are trimer-like structures that was first reported by Rutter et al<sup>199</sup> and was later more extensively studied using special Fe-coated Tungsten tips where they appear more clear in STM.<sup>200</sup>

Qi et al. proposed a plausible model for appearance of these defects and as for clarity to the reader a modified figure from this reference is shown in figure 7.6. The trimer like features appear along with rosette like defects all positioned at the SiC(6×6) high symmetry points as seen in figure 7.6a. Their appearance are due to pentagons (H<sub>5</sub>) and heptagons (H<sub>7</sub>) inserted in the buffer layer with two different arrangements at high symmetry points in the full (6√3×6√3)R30 epitaxial unit cell as visualized in figure 7.6b. The two types of high symmetry points are carbon atoms in nearly on-top sites with Si atoms of the SiC substrate (blue color in fig. 7.6b) or in hollow sites (red color in fig. 7.6b) with Si atoms of the SiC substrate. Hence the buffer layer deviates from a perfect hexagonal mesh (H<sub>6</sub>) at the symmetry points which causes a rather significant C-C bond distortion and warping of the buffer layer but preserves the long range translational integrity of the graphene lattice. Figure 7.6c show calculated DOS of on-top sites symmetry appearing as trimers in STM. Also shown in figure 7.6d are hollow sites which results in rosette-like defects in STM.

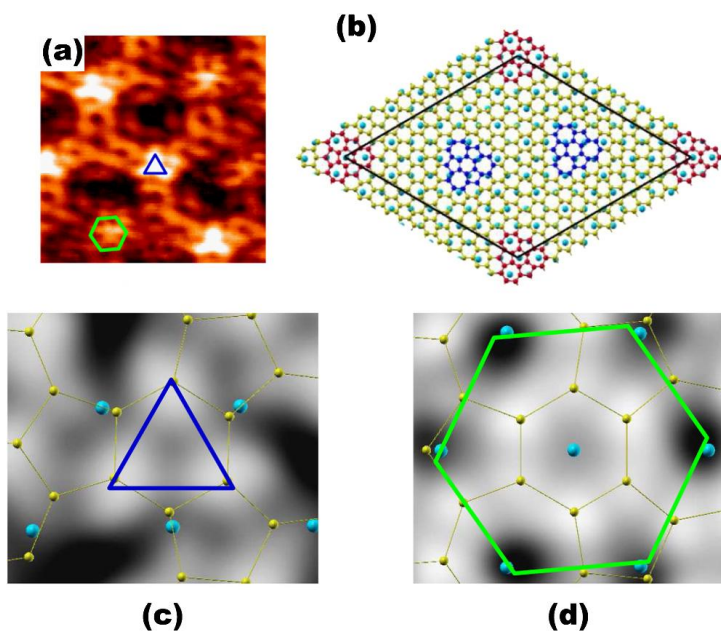


**Figure 7.6** From ref [200]. (a) STM image of epitaxial graphene on 6H-SiC(0001) with the two different types of defects occurring at the buffer layer SiC interface: trimer-like marked with blue triangle and rosette-like marked with green hexagon.  $E=-0.1$  V,  $I=0.3$  nA (b) Proposed model of buffer layer  $(6\sqrt{3}\times 6\sqrt{3})R30$  unit cell with  $H_{5,6,7}$  top and hollow defects without causing dislocations. (c-d) Calculated DOS isosurfaces for occupied states between -0.1 eV and the Fermi level for the (c) top and (d) hollow variants. Carbon atoms are represented by small balls; Si, by larger balls.

An interesting remark is that the surface density of the defects is highly dependent on the growth condition of the epitaxial graphene but the trimers are always significantly more populated than rosettes. At the trimer defects, the buffer layer is pulled closer towards the SiC substrate with  $0.3 \text{ \AA}$  from the Si-C nominal interplanar separation. The depression of the buffer layer can explain the triangular defects seen in decoupled buffer layer by Na intercalation as shall be discussed below.

Figure 7.7a shows an area of coexisting areas of SLG and structure SiC/Na/G. the triangular defects are present in similar population and separated with same distance in structure

SiC/Na/G as the trimer defects seen in the SLG. A conceivable theory is therefore as the buffer layer is warped towards SiC at trimer defects it causes a size confinement of the Na atoms resulting in Na vacancies at these sites. The Na vacancies seems however not to interrupt the decoupling of the buffer layer as perfect honeycombs are observed even in the center of triangular defects (figure 7.3f). Also, because only honeycombs are seen in the decoupled buffer layer (fig 7.3f), the carbon atoms must rearrange them selves from  $H_{5,6,7}$  structure to pure  $H_6$  normal hexagonal structure after the intercalation of Na has occurred. Such self healing process is certainly possible since no carbon atoms has to be added nor removed as the number of heptagons and pentagons are the same at the original defect sites.

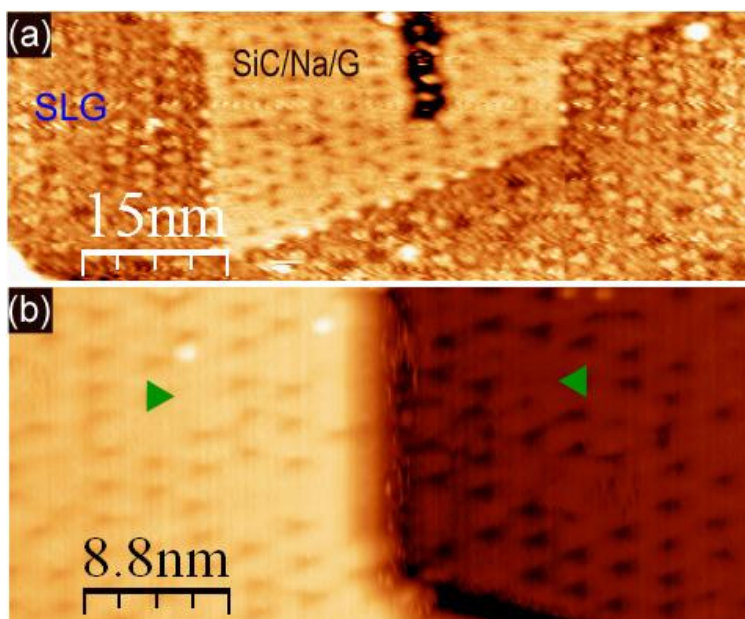


**Figure 7.7** (a) Surface of coexisting epitaxial graphene (SiC/B/G) and SiC/Na/G trimer top site defects shown as small protrusions in (SiC/B/G) and triangular defects seen as depressions on (SiC/Na/G). (b) (SiC/Na/G) coexisting on both S and S\* bulk SiC surfaces where the two possible orientations of the triangular defects are marked out in green color.

Another strong argument that the triangular defects in SiC/Na/G are induced by SiC interface structures is that they reveal the surface chirality of the SiC(0001). As described in chapter 1 the SiC consist of two types of hexagonal surfaces (S and S\*). They are rotated by 60 degrees from each other which make them look identical in the hexagonal bare  $(\sqrt{3}\times\sqrt{3})R30$  surface and in the hexagonal graphene surface. The triangular symmetry of the defects however clearly exposes the two possible surface orientations. Figure 7.7b shows an area of SiC/Na/G on coexisting S and S\* SiC(0001) with the only two different orientations possible for the triangular defects, rotated 60 degrees with respect to each other.

## 8: REFERENCES

1. J. Chelikowsky, MRS Bulletin **27**, 951-960 (2002).
2. M. Lundstrom, Science **299** (5604), 210-211 (2003).
3. G. E. Moore, Electronics **38** (8) (1965).
4. C. Berger, Z. Song, T. Li, X. Li, A. Y. Ogbazghi, R. Feng, Z. Dai, A. N. Marchenkov, E. H. Conrad, P. N. First and W. A. de Heer, The Journal of Physical Chemistry B **108** (52), 19912-19916 (2004).
5. A. K. Geim and K. S. Novoselov, Nat Mater **6** (3), 183-191 (2007).
6. C. Lee, X. Wei, J. W. Kysar and J. Hone, Science **321** (5887), 385-388 (2008).
7. K. S. Kim, Y. Zhao, H. Jang, S. Y. Lee, J. M. Kim, K. S. Kim, J.-H. Ahn, P. Kim, J.-Y. Choi and B. H. Hong, Nature **457** (7230), 706-710 (2009).
8. D. W. Jorgenson, Annual Report, 2005.
9. L. D. Landau, Phys. Z. Sowjetunion **11**, 26-35 (1937).
10. P. R. Wallace, Physical Review **71** (9), 622-634 (1947).
11. S. Iijima and T. Ichihashi, Nature **363** (6430), 603-605 (1993).
12. D. S. Bethune, C. H. Klang, M. S. de Vries, G. Gorman, R. Savoy, J. Vazquez and R. Beyers, Nature **363** (6430), 605-607 (1993).
13. S. Frank, P. Poncharal, Z. L. Wang and W. A. d. Heer, Science **280** (5370), 1744-1746 (1998).
14. S. J. Tans, A. R. M. Verschueren and C. Dekker, Nature **393** (6680), 49-52 (1998).
15. K. S. Novoselov, D. Jiang, F. Schedin, T. J. Booth, V. V. Khotkevich, S. V. Morozov and A. K. Geim, Proceedings of the National Academy of Sciences of the United States of America **102** (30), 10451-10453 (2005).
16. K. S. Novoselov, A. K. Geim, S. V. Morozov, D. Jiang, Y. Zhang, S. V. Dubonos, I. V. Grigorieva and A. A. Firsov, Science **306** (5696), 666-669 (2004).

17. K. S. Novoselov, A. K. Geim, S. V. Morozov, D. Jiang, M. I. Katsnelson, I. V. Grigorieva, S. V. Dubonos and A. A. Firsov, *Nature* **438** (7065), 197-200 (2005).
18. A. J. Van Bommel, J. E. Crombeen and A. Van Tooren, *Surface Science* **48** (2), 463-472 (1975).
19. S. T. Allen, S. T. Sheppard, W. L. Pribble, R. A. Sadler, T. S. Alcorn, Z. Ring and J. W. Palmour, *MRS Online Proceedings Library* **572** (1999).
20. G. A. Slack, *Journal of Applied Physics* **35** (12), 3460-3466 (1964).
21. A. O. Konstantinov, Q. Wahab, N. Nordell and U. Lindefelt, *Applied Physics Letters* **71** (1), 90-92 (1997).
22. Z. C. Feng, *SiC Power Materials: Devices and Applications*. (Springer-Verlag, 2004).
23. J. A. Cooper, *Materials Science Forum* **389-293** (2002).
24. S. E. Saddow and A. K. Agarwal, *Advances in Silicon Carbide Processing and Applications*. (Artech House, Norwood, 2004).
25. Cree, (Durham, 2011).
26. U. Starke, J. Bernhardt, J. Schardt and K. Heinz, *Surface Review and Letters* **06** (06), 1129-1141 (1999).
27. J. Hass, W. A. De Heer and E. H. Conrad, *Journal of Physics: Condensed Matter* **20** (32), 323202 (2008).
28. V. Y. Aristov, G. Urbanik, K. Kummer, D. V. Vyalikh, O. V. Molodtsova, A. B. Preobrajenski, A. A. Zakharov, C. Hess, T. Hanke, B. Buchner, I. Vobornik, J. Fujii, G. Panaccione, Y. A. Ossipyan and M. Knupfer, *Nano Letters* **10** (3), 992-995 (2010).
29. U. Starke, *MRS Online Proceedings Library* **742**, 1 (2002).
30. X. N. Xie, N. Yakolev and K. P. Loh, *The Journal of Chemical Physics* **119** (3), 1789-1793 (2003).
31. D. Chung, *Journal of Materials Science* **37** (8), 1475-1489 (2002).
32. R. Saito, G. Dresselhaus and M. S. Dresselhaus, *Physical Properties of Carbon Nanotubes*. (Imperial Collage Press, London, 1998).

33. J. C. Charlier, P. Eklund, J. Zhu and A. Ferrari, (Springer Berlin / Heidelberg, 2008), Vol. 111, pp. 673-709.
34. E. McCann, in *Graphene Nanoelectronics: Metrology, Synthesis, Properties and Applications*, edited by H. Raza (Springer, 2012).
35. J. González, F. Guinea and M. A. H. Vozmediano, *Physical Review Letters* **77** (17), 3589-3592 (1996).
36. C. Riedl, C. Coletti and U. Starke, *Journal of Physics D: Applied Physics* **43** (37), 374009 (2010).
37. K. V. Emtsev, F. Speck, T. Seyller, L. Ley and J. D. Riley, *Physical Review B* **77** (15), 155303 (2008).
38. T. Seyller, *Graphene Nanoelectronics: Metrology, Synthesis, Properties and Application*. (Springer, Iowa City, 2012).
39. A. Mattausch and O. Pankratov, *Physical Review Letters* **99** (7), 076802 (2007).
40. S. V. Morozov, K. S. Novoselov, M. I. Katsnelson, F. Schedin, D. C. Elias, J. A. Jaszczak and A. K. Geim, *Physical Review Letters* **100** (1), 016602 (2008).
41. R. S. Muller and T. I. Kamins, *Device Electronics for Integrated Circuits*, 3rd ed. (Wiley, 2002).
42. J. Zhu, *Graphene Nanoelectronics*. (Springer, Atlanta, 2012).
43. K. I. Bolotin, K. J. Sikes, Z. Jiang, M. Klima, G. Fudenberg, J. Hone, P. Kim and H. L. Stormer, *Solid State Commun.* **146** (9-10), 351-355 (2008).
44. J. H. Chen, C. Jang, S. Adam, M. S. Fuhrer, E. D. Williams and M. Ishigami, *Nat. Phys.* **4** (5), 377-381 (2008).
45. E. H. Hwang, S. Adam and S. Das Sarma, *Physical Review Letters* **98** (18), 186806 (2007).
46. T. Ando and T. Nakanishi, *Journal of the Physical Society of Japan* **67** (5), 1704-1713 (1998).
47. J. L. Tedesco, B. L. VanMil, R. L. Myers-Ward, J. M. McCrate, S. A. Kitt, P. M. Campbell, G. G. Jernigan, J. C. Culbertson, J. C. R. Eddy and D. K. Gaskill, *Applied Physics Letters* **95** (12), 122102 (2009).

48. J. Jobst, D. Waldmann, F. Speck, R. Hirner, D. K. Maude, T. Seyller and H. B. Weber, *Physical Review B* **81** (19), 195434 (2010).
49. G. M. Rutter, J. N. Crain, N. P. Guisinger, P. N. First and J. A. Stroscio, 2008 (unpublished).
50. B. Partoens and F. M. Peeters, *Physical Review B* **74** (7), 075404 (2006).
51. J. Hass, F. Varchon, J. E. Millán-Otoya, M. Sprinkle, N. Sharma, W. A. de Heer, C. Berger, P. N. First, L. Magaud and E. H. Conrad, *Physical Review Letters* **100** (12), 125504 (2008).
52. M. Y. Han, B. Özyilmaz, Y. Zhang and P. Kim, *Physical Review Letters* **98** (20), 206805 (2007).
53. B. Obradovic, R. Kotlyar, F. Heinz, P. Matagne, T. Rakshit, M. D. Giles, M. A. Stettler and D. E. Nikonov, *Applied Physics Letters* **88** (14), 142102 (2006).
54. Y.-M. Lin, A. Valdes-Garcia, S.-J. Han, D. B. Farmer, I. Meric, Y. Sun, Y. Wu, C. Dimitrakopoulos, A. Grill, P. Avouris and K. A. Jenkins, *Science* **332** (6035), 1294-1297 (2011).
55. A. F. Young and P. Kim, *Nat Phys* **5** (3), 222-226 (2009).
56. V. V. Cheianov, V. Fal'ko and B. L. Altshuler, *Science* **315** (5816), 1252-1255 (2007).
57. S. Bae, H. Kim, Y. Lee, X. Xu, J.-S. Park, Y. Zheng, J. Balakrishnan, T. Lei, H. Ri Kim, Y. I. Song, Y.-J. Kim, K. S. Kim, B. Ozyilmaz, J.-H. Ahn, B. H. Hong and S. Iijima, *Nat Nano* **5** (8), 574-578 (2010).
58. Y. G. Semenov, K. W. Kim and J. M. Zavada, *Applied Physics Letters* **91** (15), 153105 (2007).
59. P. Auger, *J. Phys. Radium* **6**, 205-208 (1925).
60. D. F. Stein and A. Joshi, *Annual Review of Materials Science* **11** (1), 485-504 (1981).
61. J. F. Watts and J. Wolstenholme, *An introduction to surface analysis by XPS and AES*. (John Wiley & Sons, 2003).
62. D. R. Jennison, *Journal of Vacuum Science and Technology* **20** (3), 548-554 (1982).

63. J. E. Houston, J. W. Rogers, Jr., R. R. Rye, F. L. Hutson and D. E. Ramaker, *Physical Review B* **34** (2), 1215-1226 (1986).
64. P. W. Palmberg, G. K. Bohn and J. C. Tracy, *Applied Physics Letters* **15** (8), 254-255 (1969).
65. G. C. Smith, *Surface Analysis by Electron Spectroscopy: Measurement and Interpretation*. (Plenum Press, New York, 1994).
66. T. Li, Georgia Institute of Technology, 2006.
67. C. J. Davisson and L. H. Germer, *Proc Natl Acad Sci U S A.* **14** (4), 317-322 (1928).
68. J. C. Riviere, *Contemporary Physics: Auger electron spectroscopy*,. (Taylor and Francis, 1973).
69. L. J. Clarke, *Surface Crystallography: An introduction to Low Energy Electron Diffraction*. (Wiley-Interscience, 1985).
70. M. A. Van Hove, W. H. Weinberg and C. M. Chan, *Low-Energy Electron Diffraction, Publisher*. (Springer Verlag, 1986).
71. P. Ewald, *Acta Crystallographica Section A* **25** (1), 103-108 (1969).
72. E. A. Wood, *Journal of Applied Physics* **35** (4), 1306-1312 (1964).
73. G. Binnig, H. Rohrer, C. Gerber and E. Weibel, *Physical Review Letters* **49** (1), 57-61 (1982).
74. J. A. Stroscio and W. J. Kaiser, *Scanning tunneling Microscopy*. (Academic Press, San Diego).
75. H.-J. Güntherodt and R. Wiesendanger, *Scanning tunneling microscopy I: general principles and applications to clean and adsorbate-covered surfaces*. (Springer Verlag, 1994).
76. C. J. Chen, *Introduction to Scanning Tunneling Microscopy*, second ed. (Oxford University Press, 2008).
77. J. Tersoff and D. R. Hamann, *Physical Review B* **31** (2), 805-813 (1985).

78. L. E. van de Leemput and H. van kempen, *Reports on Progress in Physics* **55**, 1165 (1992).
79. J. Bardeen, *Physical Review Letters* **6** (2), 57-59 (1961).
80. C. J. Chen, *Physical Review Letters* **65** (4), 448-451 (1990).
81. A. Pronschinske, D. J. Mardit and D. B. Dougherty, *Physical Review B* **84** (20), 205427 (2011).
82. I. Giaever, *Physical Review Letters* **5** (4), 147-148 (1960).
83. Y. Zhang, Y.-W. Tan, H. L. Stormer and P. Kim, *Nature* **438** (7065), 201-204 (2005).
84. J. B. Hannon and R. M. Tromp, *Physical Review B* **77** (24), 241404 (2008).
85. M. Hupalo, E. H. Conrad and M. C. Tringides, *Physical Review B* **80** (4), 041401 (2009).
86. K. V. Emtsev, A. Bostwick, K. Horn, J. Jobst, G. L. Kellogg, L. Ley, J. L. McChesney, T. Ohta, S. A. Reshanov, J. Rohrl, E. Rotenberg, A. K. Schmid, D. Waldmann, H. B. Weber and T. Seyller, *Nat Mater* **8** (3), 203-207 (2009).
87. C. Virojanadara, M. Syväjarvi, R. Yakimova, L. I. Johansson, A. A. Zakharov and T. Balasubramanian, *Physical Review B* **78** (24), 245403 (2008).
88. R. M. Tromp and J. B. Hannon, *Physical Review Letters* **102** (10), 106104 (2009).
89. W. A. de Heer, C. Berger, M. Ruan, M. Sprinkle, X. Li, Y. Hu, B. Zhang, J. Hankinson and E. Conrad, *Proceedings of the National Academy of Sciences* **108** (41), 16900-16905 (2011).
90. F. Owman, C. Hallin, P. Mårtensson and E. Janzén, *Journal of Crystal Growth* **167** (1-2), 391-395 (1996).
91. V. Ramachandran, M. Brady, A. Smith, R. Feenstra and D. Greve, *Journal of Electronic Materials* **27** (4), 308-312 (1998).
92. C. Riedl, C. Coletti, T. Iwasaki, A. A. Zakharov and U. Starke, *Physical Review Letters* **103** (24), 246804 (2009).

93. C. Virojanadara, A. A. Zakharov, R. Yakimova and L. I. Johansson, *Surface Science* **604** (2), L4-L7 (2010).
94. U. Starke, J. Schardt and M. Franke, *Applied Physics A: Materials Science & Processing* **65** (6), 587-596 (1997).
95. V. Borovikov and A. Zangwill, *Arxiv* (2009).
96. J. Abrefah and D. R. Olander, *Surface Science* **209** (3), 291-313 (1989).
97. Y. Wei, L. Li and I. S. T. Tsong, *Applied Physics Letters* **66** (14), 1818-1820 (1995).
98. C. R. Stoldt, C. Carraro and R. Maboudian, *Surface Science* **466** (1-3), 66-72 (2000).
99. N. Sieber, B. F. Mantel, T. Seyller, J. Ristein, L. Ley, T. Heller, D. R. Batchelor and D. Schmeisser, *Applied Physics Letters* **78** (9), 1216-1218 (2001).
100. J. Bernhardt, J. Schardt, U. Starke and K. Heinz, *Applied Physics Letters* **74** (8), 1084-1086 (1999).
101. S. Veprek, C. Wang and M. G. J. Veprek-Heijman, *Journal of Vacuum Science & Technology A: Vacuum, Surfaces, and Films* **26** (3), 313-320 (2008).
102. J. D. Jackson, *Classical electrodynamics Third Edition*. (Wiley, 1999).
103. W. Shockley, *Physical Review* **56** (4), 317-323 (1939).
104. P. M. Echenique and J. B. Pendry, *J. Phys. C: Solid St. Phys.* **11**, 2065 (1978).
105. D. Straub and F. J. Himpsel, *Physical Review B* **33** (4), 2256-2262 (1986).
106. K. Giesen, F. Hage, F. J. Himpsel, H. J. Riess and W. Steinmann, *Physical Review Letters* **55** (3), 300-303 (1985).
107. T. Fauster and W. Steinmann, *Electromagnetic Waves: Recent Developments in Research*. (North-Holland, Amsterdam, 1994).
108. S. L. Hulbert, P. D. Johnson, M. Weinert and R. F. Garrett, *Physical Review B* **33** (2), 760-764 (1986).
109. G. Binnig, K. H. Frank, H. Fuchs, N. Garcia, B. Reihl, H. Rohrer, F. Salvan and A. R. Williams, *Physical Review Letters* **55** (9), 991-994 (1985).

110. D. B. Dougherty, P. Maksymovych, J. Lee, M. Feng, H. Petek and J. T. Yates, *Physical Review B* **76** (12), 9 (2007).
111. T. Seyller, A. Bostwick, K. V. Emtsev, K. Horn, L. Ley, J. L. McChesney, T. Ohta, J. D. Riley, E. Rotenberg and F. Speck, *Phys. Status Solidi B-Basic Solid State Phys.* **245** (7), 1436-1446 (2008).
112. T. Ohta, A. Bostwick, T. Seyller, K. Horn and E. Rotenberg, *Science* **313** (5789), 951-954 (2006).
113. G. M. Rutter, J. N. Crain, N. P. Guisinger, T. Li, P. N. First and J. A. Stroscio, *Science* **317** (5835), 219-222 (2007).
114. S. Y. Zhou, G. H. Gweon, A. V. Fedorov, P. N. First, W. A. De Heer, D. H. Lee, F. Guinea, A. H. C. Neto and A. Lanzara, *Nat. Mater.* **6** (10), 770-775 (2007).
115. A. K. Geim and K. S. Novoselov, *Nat. Mater.* **6** (3), 183-191 (2007).
116. J. L. Tedesco, B. L. VanMil, R. L. Myers-Ward, J. M. McCrate, S. A. Kitt, P. M. Campbell, G. G. Jernigan, J. C. Culbertson, C. R. Eddy and D. K. Gaskill, *Applied Physics Letters* **95** (12), 3 (2009).
117. D. L. Miller, K. D. Kubista, G. M. Rutter, M. Ruan, W. A. de Heer, P. N. First and J. A. Stroscio, *Science* **324** (5929), 924-927 (2009).
118. J. H. Chen, C. Jang, S. D. Xiao, M. Ishigami and M. S. Fuhrer, *Nat. Nanotechnol.* **3** (4), 206-209 (2008).
119. C. Jang, S. Adam, J. H. Chen, D. Williams, S. Das Sarma and M. S. Fuhrer, *Physical Review Letters* **101** (14), 4 (2008).
120. J. H. Chen, C. Jang, M. Ishigami, S. Xiao, W. G. Cullen, E. D. Williams and M. S. Fuhrer, *Solid State Commun.* **149** (27-28), 1080-1086 (2009).
121. P. M. Echenique, J. Osma, M. Machado, V. M. Silkin, E. V. Chulkov and J. M. Pitarke, *Prog. Surf. Sci.* **67** (1-8), 271-283 (2001).
122. P. M. Echenique and J. B. Pendry, *Journal of Physics C-Solid State Physics* **11** (10), 2065 (1978).
123. G. Binnig, K. H. Frank, H. Fuchs, N. Garcia, B. Reihl, H. Rohrer, F. Salvan and A. R. Williams, *Physical Review Letters* **55** (9), 991-994 (1985).

124. P. Wahl, M. A. Schneider, L. Diekhoner, R. Vogelgesang and K. Kern, *Physical Review Letters* **91** (10), 4 (2003).
125. V. M. Silkin, J. Zhao, F. Guinea, E. V. Chulkov, P. M. Echenique and H. Petek, *Physical Review B* **80** (12), 4 (2009).
126. M. Posternak, A. Baldereschi, A. J. Freeman and E. Wimmer, *Physical Review Letters* **52** (10), 863 (1984).
127. S. Bose, V. M. Silkin, R. Ohmann, I. Brihuega, L. Vitali, C. H. Michaelis, P. Mallet, J. Y. Veuillen, M. A. Schneider, E. V. Chulkov, P. M. Echenique and K. Kern, *New J. Phys.* **12**, 023028 (2010).
128. A. J. Caamaño, Y. Pogorelov, O. Custance, J. Méndez, A. M. Baró, J. Y. Veuillen, J. M. Gómez-Rodríguez and J. J. Sáenz, *Surface Science* **426** (1), L420-L425 (1999).
129. H. Yang, G. Baffou, A. J. Mayne, G. Comtet, G. Dujardin and Y. Kuk, *Physical Review B* **78** (4), 4 (2008).
130. T. Filleter, K. V. Emtsev, T. Seyller and R. Bennewitz, *Applied Physics Letters* **93** (13), 3 (2008).
131. B. Wunsch, T. Stauber, F. Sols and F. Guinea, *New J. Phys.* **8**, 15 (2006).
132. P. K. Pyatkovskiy, *J. Phys.-Condes. Matter* **21** (2), 8 (2009).
133. M. van Schilfgaarde, Katsnelson, M.I., [arXiv:1006.2426v1](https://arxiv.org/abs/1006.2426v1) [cond-mat.mes-hall] (2010).
134. S. Y. Zhou, D. A. Siegel, A. V. Fedorov, F. El Gabaly, A. K. Schmid, A. H. C. Neto, D. H. Lee and A. Lanzara, *Nat. Mater.* **7** (4), 259-260 (2008).
135. C. Benesch, M. Fartmann and H. Merz, *Physical Review B* **64** (20), 10 (2001).
136. D. B. Dougherty, P. Maksymovych, J. Lee and J. T. Yates, Jr., *Physical Review Letters* **97** (23), 236806 (2006).
137. H.-C. Ploigt, C. Brun, M. Pivetta, F. Patthey and W.-D. Schneider, *Physical Review B* **76** (19), 195404 (2007).
138. H. Hibino, H. Kageshima, M. Kotsugi, F. Maeda, F. Z. Guo and Y. Watanabe, *Physical Review B* **79** (12), 125437 (2009).

139. T. Ohta, A. Bostwick, J. L. McChesney, T. Seyller, K. Horn and E. Rotenberg, *Physical Review Letters* **98** (20), 206802-206804 (2007).
140. A. Bostwick, K. Emtsev, K. Horn, E. Huwald, L. Ley, J. McChesney, T. Ohta, J. Riley, E. Rotenberg, F. Speck and T. Seyller, edited by R. Haug (Springer Berlin / Heidelberg, 2008), Vol. 47, pp. 159-170.
141. S. A. Wolf, D. D. Awschalom, R. A. Buhrman, J. M. Daughton, S. von Molnár, M. L. Roukes, A. Y. Chtchelkanova and D. M. Treger, *Science* **294** (5546), 1488-1495 (2001).
142. D. D. Awschalom and M. E. Flatte, *Nat Phys* **3** (3), 153-159 (2007).
143. A. Aviram and M. A. Ratner, *Chemical Physics Letters* **29** (2), 277-283 (1974).
144. S. Sanvito, *Chemical Society Reviews* **40** (6), 3336-3355 (2011).
145. R. W. I. d. Boer, A. F. Stassen, M. F. Craciun, C. L. Mulder, A. Molinari, S. Rogge and A. F. Morpurgo, *Applied Physics Letters* **86** (26), 262109 (2005).
146. N. Tsukahara, K.-i. Noto, M. Ohara, S. Shiraki, N. Takagi, Y. Takata, J. Miyawaki, M. Taguchi, A. Chainani, S. Shin and M. Kawai, *Physical Review Letters* **102** (16), 167203 (2009).
147. J. Brede, N. Atodiresei, S. Kuck, P. Lazić, V. Caciuc, Y. Morikawa, G. Hoffmann, S. Blügel and R. Wiesendanger, *Physical Review Letters* **105** (4), 047204 (2010).
148. C. Iacovita, M. V. Rastei, B. W. Heinrich, T. Brumme, J. Kortus, L. Limot and J. P. Bucher, *Physical Review Letters* **101** (11), 116602 (2008).
149. S. Ghosh, I. Calizo, D. Teweldebrhan, E. P. Pokatilov, D. L. Nika, A. A. Balandin, W. Bao, F. Miao and C. N. Lau, *Applied Physics Letters* **92** (15), 151911 (2008).
150. A. Candini, S. Klyatskaya, M. Ruben, W. Wernsdorfer and M. Affronte, *Nano Letters* **11** (7), 2634-2639 (2011).
151. J. Mao, H. Zhang, Y. Jiang, Y. Pan, M. Gao, W. Xiao and H. J. Gao, *Journal of the American Chemical Society* **131** (40), 14136-14137 (2009).
152. H. G. Zhang, J. T. Sun, T. Low, L. Z. Zhang, Y. Pan, Q. Liu, J. H. Mao, H. T. Zhou, H. M. Guo, S. X. Du, F. Guinea and H. J. Gao, *Physical Review B* **84** (24), 245436 (2011).

153. M. Scardamaglia, G. Forte, S. Lizzit, A. Baraldi, P. Lacovig, R. Larciprete, C. Mariani and M. Betti, *Journal of Nanoparticle Research* **13** (11), 6013-6020 (2011).
154. W. Dou, S. Huang, R. Q. Zhang and C. S. Lee, *The Journal of Chemical Physics* **134** (9), 094705 (2011).
155. I. Pletikosić, M. Kralj, P. Pervan, R. Brako, J. Coraux, A. T. N'Diaye, C. Busse and T. Michely, *Physical Review Letters* **102** (5), 056808 (2009).
156. A. Grüneis and D. V. Vyalikh, *Physical Review B* **77** (19), 193401 (2008).
157. S. Marchini, S. Günther and J. Wintterlin, *Physical Review B* **76** (7), 075429 (2007).
158. P. W. Sutter, J.-I. Flege and E. A. Sutter, *Nat Mater* **7** (5), 406-411 (2008).
159. T. Jayasekera, B. D. Kong, K. W. Kim and M. Buongiorno Nardelli, *Physical Review Letters* **104** (14), 146801 (2010).
160. J. Åhlund, J. Schnadt, K. Nilson, E. Göthelid, J. Schiessling, F. Besenbacher, N. Mårtensson and C. Puglia, *Surface Science* **601** (17), 3661-3667 (2007).
161. T. G. Gopakumar, M. Lackinger, M. Hackert, F. Müller and M. Hietschold, *The Journal of Physical Chemistry B* **108** (23), 7839-7843 (2004).
162. D. B. Dougherty, W. Jin, W. G. Cullen, J. E. Reutt-Robey and S. W. Robey, *The Journal of Physical Chemistry C* **112** (51), 20334-20339 (2008).
163. C. Isvoranu, J. Ahlund, B. Wang, E. Ataman, N. Martensson, C. Puglia, J. N. Andersen, M.-L. Bocquet and J. Schnadt, *The Journal of Chemical Physics* **131** (21), 214709 (2009).
164. K. Walzer and M. Hietschold, *Surface Science* **471** (1-3), 1-10 (2001).
165. Y.-M. Lin, C. Dimitrakopoulos, K. A. Jenkins, D. B. Farmer, H.-Y. Chiu, A. Grill and P. Avouris, *Science* **327** (5966), 662 (2010).
166. M. S. Dresselhaus and G. Dresselhaus, *Advances in Physics* **30** (2), 139-326 (1981).
167. T. E. Weller, M. Ellerby, S. S. Saxena, R. P. Smith and N. T. Skipper, *Nat Phys* **1** (1), 39-41 (2005).
168. M. S. Dresselhaus and G. Dresselhaus, *Advances in Physics* **51** (1), 1-186 (2002).

169. W. Metz and L. Siemsglüss, *Materials Science and Engineering* **31**, 119-121 (1977).
170. A. Mattausch and O. Pankratov, *Physical Review Letters* **99** (7), 4 (2007).
171. C. Virojanadara, A. A. Zakharov, R. Yakimova and L. I. Johansson, *Surface Science* **604** (2), L4-L7 (2010).
172. S. Watcharinyanon, C. Virojanadara, J. R. Osiecki, A. A. Zakharov, R. Yakimova, R. I. G. Uhrberg and L. I. Johansson, *Surface Science* **605** (17-18), 1662-1668 (2011).
173. S. Oida, F. R. McFeely, J. B. Hannon, R. M. Tromp, M. Copel, Z. Chen, Y. Sun, D. B. Farmer and J. Yurkas, *Physical Review B* **82**, 041411R (2010).
174. A. L. Walter, K. J. Jeon, A. Bostwick, F. Speck, M. Ostler, T. Seyller, L. Moreschini, Y. S. Kim, Y. J. Chang, K. Horn and E. Rotenberg, *Applied Physics Letters* **98** (18), 184102 (2011).
175. C. Virojanadara, S. Watcharinyanon, A. A. Zakharov and L. I. Johansson, *Physical Review B* **82** (20), 205402 (2010).
176. C. Virojanadara, A. A. Zakharov, S. Watcharinyanon, R. Yakimova and L. I. Johansson, *New J. Phys.* **12**, 125015 (2010).
177. Y. C. Cheng and U. Schwingenschlogl, *Applied Physics Letters* **97** (19), 193304 (2010).
178. B. Premlal, M. Cranney, F. Vonau, D. Aubel, D. Casterman, M. M. De Souza and L. Simon, *Applied Physics Letters* **94** (26), 263115 (2009).
179. T. Jayasekera, B. D. Kong, K. W. Kim and M. B. Nardelli, *Physical Review Letters* **104** (14), 146801 (2010).
180. A. Bostwick, T. Ohta, T. Seyller, K. Horn and E. Rotenberg, *Nat. Phys.* **3** (1), 36-40 (2007).
181. A. Bostwick, F. Speck, T. Seyller, K. Horn, M. Polini, R. Asgari, A. H. MacDonald and E. Rotenberg, *Science* **328** (5981), 999-1002 (2010).
182. J. L. McChesney, A. Bostwick, T. Ohta, T. Seyller, K. Horn, J. Gonzalez and E. Rotenberg, *Physical Review Letters* **104** (13), 136803 (2010).

183. V. M. Silkin, J. Zhao, F. Guinea, E. V. Chulkov, P. M. Echenique and H. Petek, *Physical Review B* **80** (12), 121408R (2009).
184. A. Sandin, A. Pronschinske, J. E. Rowe and D. B. Dougherty, *Applied Physics Letters* **97** (11), 113104 (2010).
185. P. Giannozzi, S. Baroni, N. Bonini, M. Calandra, R. Car, C. Cavazzoni, D. Ceresoli, G. L. Chiarotti, M. Cococcioni, I. Dabo, A. Dal Corso, S. de Gironcoli, S. Fabris, G. Fratesi, R. Gebauer, U. Gerstmann, C. Gougoussis, A. Kokalj, M. Lazzeri, L. Martin-Samos, N. Marzari, F. Mauri, R. Mazzarello, S. Paolini, A. Pasquarello, L. Paulatto, C. Sbraccia, S. Scandolo, G. Sclauzero, A. P. Seitsonen, A. Smogunov, P. Umari and R. M. Wentzcovitch, *J. Phys.-Condes. Matter* **21** (39), 395502 (2009).
186. S. M. Choi and S. H. Jhi, *Applied Physics Letters* **94** (15), 153108 (2009).
187. T. Filleter, K. V. Emtsev, T. Seyller and R. Bennewitz, *Applied Physics Letters* **93** (13), 113117 (2008).
188. B. Lee, S. Han and Y.-S. Kim, *Physical Review B* **81** (7), 075432 (2010).
189. J. S. Bunch, S. S. Verbridge, J. S. Alden, A. M. van der Zande, J. M. Parpia, H. G. Craighead and P. L. McEuen, *Nano Letters* **8** (8), 2458-2462 (2008).
190. O. Leenaerts, B. Partoens and F. M. Peeters, *Applied Physics Letters* **93** (19), 193107 (2008).
191. V. Meunier, J. Kephart, C. Roland and J. Bernholc, *Physical Review Letters* **88** (7), 075506 (2002).
192. Y. Li, G. Zhou, J. Li, J. Wu, B.-L. Gu and W. Duan, *The Journal of Physical Chemistry C* **115** (48), 23992-23997 (2011).
193. J. Choi, H. Lee and S. Kim, *The Journal of Physical Chemistry C* **114** (31), 13344-13348 (2010).
194. J. M. Carlsson and M. Scheffler, *Physical Review Letters* **96** (4), 046806 (2006).
195. J. Algdal, T. Balasubramanian, M. Breitholtz, T. Kihlgren and L. Walldén, *Surface Science* **601** (4), 1167-1175 (2007).
196. S. P. Kelty and C. M. Lieber, *Physical Review B* **40** (8), 5856-5859 (1989).
197. M. Caragiu and S. Finberg, *Journal of Physics: Condensed Matter* **17** (35), R995-R1024 (2005).

198. M. Breitholtz, T. Kihlgren, S. Å. Lindgren, H. Olin, E. Wahlström and L. Walldén, *Physical Review B* **64** (7), 073301 (2001).
199. G. M. Rutter, N. P. Guisinger, J. N. Crain, E. A. A. Jarvis, M. D. Stiles, T. Li, P. N. First and J. A. Stroscio, *Physical Review B* **76** (23), 235416 (2007).
200. Y. Qi, S. H. Rhim, G. F. Sun, M. Weinert and L. Li, *Physical Review Letters* **105** (8), 085502 (2010).